UNIVERSITÀ DEGLI STUDI DI UDINE
hic sunt futura

www.uniud.it

Corso di dottorato di ricerca in:

Informatica e Scienze Matematiche e Fisiche

Ciclo 34°

Development of the FAMU experimental apparatus for the proton radius measurement

Dottorando

Marco Baruzzo

Supervisore

Prof. Andrea Vacchi

Co-supervisore

Dott. Emiliano Mocchiutti

Anno 2022

Abstract

The proton, the nucleus of the hydrogen atom, is the building block of the universe and its fascinating internal structure is defined by Quantum Chromo-Dynamics. Our experiment will measure the hyperfine splitting of the muonic hydrogen atom (μp) to study the proton's internal magnetic structure by laser exciting from singlet μp to the triplet state with an original technique that we have proposed and tested in recent years.

Have had the chance to enter the FAMU (Fisica degli Atomi MUonici) experiment in its final realization phase and I could take part in the development of all aspects of the experiment from the preliminary data taking and the subsequent analysis to the definition of the layout and the development of the laser.

In particular, I took part in the preliminary data collection at ISIS accelerator facility at Rutherford Appleton Laboratory (RAL) in UK. I contributed to the analysis of the data collected by the detectors based on Ce:$LaBr_3$ scintillation crystals with an innovative readout based on SiPM (Silicon Photo-Multiplier), finding useful improvements to perfection the resolution of these detectors. I also analyzed the data collected in the 2016 FAMU data acquisition, improving the knowledge on the argon transfer rate dependence on the temperature and X-rays de-excitation energy spectra. I designed the trigger system and realized the laser data acquisition system.

The major work in which I was involved was on FAMU laser system, which will excite the hyperfine splitting transition, the most crucial part of the experiment. I participated, taking also the responsibility of the laser safety officer a RAL, to the development and characterization of the oscillator and amplifier for the 1.26 μm laser source, which we developed on purpose for our experiment. The test and qualification of all the non linear crystals were additional aspects of my work for our laser source, for which I developed the whole laser control program. This program allows to

control remotely and in real time every aspect of the laser: from the wavelength to the energy production and the control of the stabilization of the beams through a feedback system developed on purpose. Hit by the consequences of the COVID-19 pandemic, while continuously improving the laser and experiment layout, we were forced to postpone the data acquisition of the experiment at RAL in September 2022, after the one-year-long maintenance shutdown of the accelerator.

Contents

1 Introduction **7**
1.1 Proton radius 7

2 Fisica degli Atomi Muonici (FAMU) **13**
2.1 Methods 13
2.1.1 Zemach Radius from transfer rate measurement . . . 13
2.1.2 The extraction of the transfer rate value 17
2.1.3 Calculation of the Zemach radius from the transfer rate variation 19
2.2 Verification of the FAMU experimental method 21
2.2.1 Physical target development 21
2.2.2 2014-2018 FAMU measurements 24
2.2.3 Temperature and transfer rate to argon 29
2.2.4 Transfer rate to oxygen and the final choice 40

3 FAMU experimental setup **43**
3.1 The apparatus 43
3.2 Muon beam 44
3.3 Experimental target 46
3.4 Detector system 50
3.5 Mid-IR laser 55
3.5.1 FAMU laser setup 56
3.5.2 1.06 μm Laser Beam 57
3.5.3 1.26 μm Laser Beam 58
3.5.4 Combining the two beams 62
3.5.5 DFG scheme 65
3.5.6 Target injection 67
3.6 Data acquisition system 67

4 Developments **73**
4.1 Layout development 73
4.2 Test on advanced detector based on
Ce:$LaBr_3$ read by SiPM 74
4.3 Laser development 80
4.3.1 Oscillator improvement and characterization 80
4.3.2 Amplifier development and characterization 88
4.3.3 DFG setup development and characterization 95

5 Conclusions **115**

Chapter 1

Introduction

1.1 Proton radius

Starting from 50s and 60s different experiments measured the proton radius with the highest precision possible at that time using different techniques belonging to two main categories: electron and muon based experiments. The results obtained through out the years, as can be seen in figure 1.1, are not in agreement. The proton radius measurements differ within the same technique, but more interestingly the muonic hydrogen measurement is more than 5 σ away from the most recent and precise electron based measurements. This discrepancy generates new questions and requires new experiments to fill the gap [1]. Several possible explanations were proposed, from a wrong interpretation of the electronic hydrogen spectroscopic measurement, to the level of refinement of the QED corrections calculations to possible new interactions between the particles which leads to new physics beyond the standard model [1, 2].

As anticipated, the experiments carried out can be divided into two categories, the electronic measurement and the muonic one. In both cases, different techniques can be used, the main ones being: lepton-proton (electrons or muons) scattering and hydrogen laser spectroscopy.

The elastic electron-proton scattering was the first technique used to measure the charge proton radius, based on the measurement of the electric and magnetic proton form factor $G_E(Q^2)$ and $G_M(Q^2)$ [3]. The first measurements done in the 60s are obsolete, while modern measurements

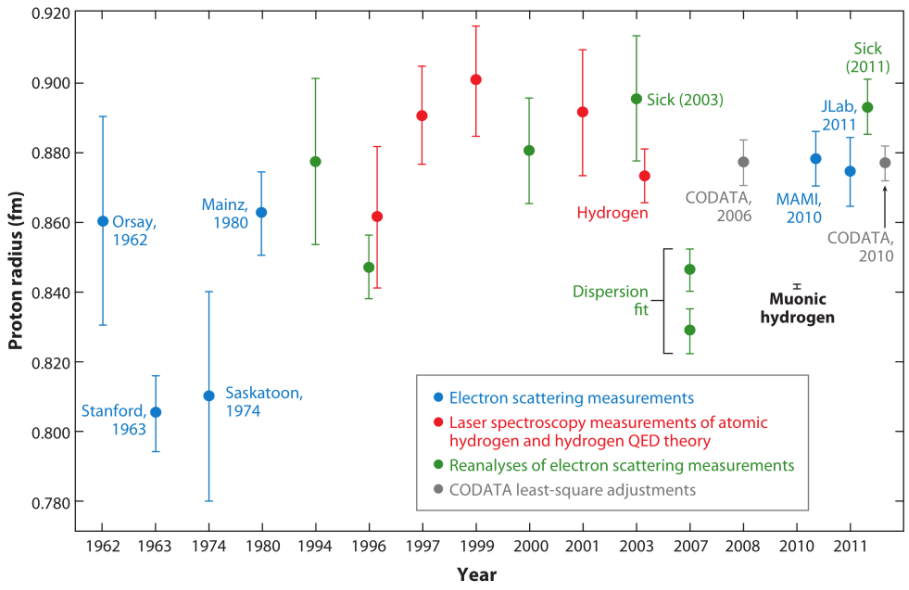

Figure 1.1: In this graph the proton radius values are plotted versus the year of measurement, to show the variation of the value and precision vs times. As can be seen, the values are not all compatible and in particular the muonic hydrogen measurement is more than 5 σ away from the last most precise CODATA value [1].

with the same technique over the past 10 years reached an accuracy of 1% [1].

The hydrogen laser spectroscopy can be both a way to measure the charge proton radius and to test the QED. The measurement of the energy levels of the hydrogen are very well predicted using QED. This can give direct access to a test of the Rydberg constant, but taking this value from a different experiment and considering QED one of the most accurate theory so far, the hydrogen laser spectroscopy can be used to measure the charge proton radius. In fact, the energy levels of the S-states of hydrogen follow this relation:

$$E(nS) \simeq -\frac{R_{\text{inf}}}{n^2} + \frac{L_{1S}}{n^3}, \tag{1.1}$$

in which R_{inf} is the Rydberg constant, n is the principal quantum number

and L_{1S} is the Lamb shift of the 1S state. From the QED:

$$L_{1S} \simeq (8.172 + 1.56\, r_p^2)$$

depends on the charge proton radius r_p. This last value can be obtained from the measurement of the energy level $E(nS)$ through laser spectroscopy and the R_{inf} from a different experiment.

Until 2010, before the introduction of high precision muon spectroscopy, the two techniques, electron-proton scattering and atomic laser spectroscopy, were the only ways in which the proton radius measurement was performed and their results, respectively R_E^{1H}=0.8775(50) fm and R_E^{1H}=0.8764(89) fm, were in agreement [4]. As we will see, the introduction of muonic hydrogen precision spectroscopy measurement opens a new issue.

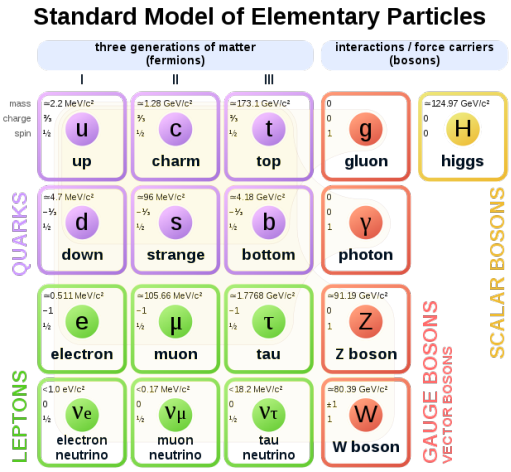

Figure 1.2: The standard model particles. In green the lepton family [5].

The muon is a particle of the lepton family, which shares some characteristics with the electron that make it an ideal substitute for the latter in high-precision measurements. Muons have charge 1 and spin 1/2 like electrons, but they are ∼207 times heavier. The direct effect of this can be observed in an atom which consists of a nucleus and a muon, instead of an electron. An atom formed in this way is called exotic atom and has

different and higher energy levels compared to the electronic ones. In particular, the muonic transitions are in the range of the keV, making the experiment and therefore also the measurement of the proton radius easier to be performed. Exploiting this increase of the binding energy gives a unique possibility to measure the charge proton radius. The characteristic of the muon that makes experiments in this category more challenging is the lifetime, which in vacuum is around 2.2 μs. Once bound to an atom, the mean lifetime shortens, but in the case of muonic hydrogen and low-Z atoms it does not vary substantially from the in vacuum values[6]. For this reason the measurement must be performed in less than $\sim$2 μs, before the muon decays or is captured by the atom.

Historically, muonic atoms are used for testing the QED prediction[7]. Recent measurements were performed with muonic hydrogen laser spectroscopy of the CREMA experiment at Paul Scherrer Institute (PSI) in Switzerland. Here a continuous muon beam was used to produce muonic hydrogen, stopping low energy muons in a low pressure hydrogen gas target. The arriving muons were tracked when entering the target and at the same time a laser was sent inside the optical cavity to illuminate the formed muonic hydrogen. At this point a set of large-area avalanche photodiodes (LAAPDs) were ready to collect the hydrogen K_α X-rays emission produced by the de-excitation. The experiment was focused on the measurement of the 2S-2P transition, giving as a result a discrepancy between the resonance found and the predicted values from the literature[8]. This discrepancy can be seen in figure 1.3.

So far, the muon-proton scattering experiment is a complete new measurement. An example of muon-proton scattering is given by the MUSE collaboration, which is planning the experiment during the 2021–2022. The setup is based on a liquid hydrogen target surrounded by a set of different detectors able to track the particles produced in the scattering and to measure their momentum. The peculiarity of the experiment is that the beam arriving to the target is not a pure muon beam, but it is also formed by electrons and pions. This characteristic permits to perform two measurements at the same time with the same apparatus, thus eliminating the possibility of system-related discrepancies[9].

To deepen the knowledge of the proton in its statics and dynamics, an-

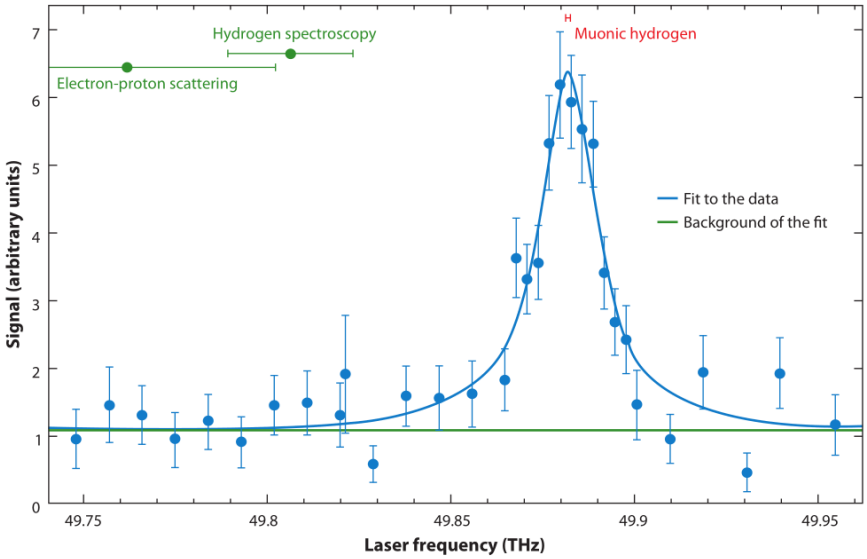

Figure 1.3: This plot shows the resonance found by the CREMA experiment vs the predicted values with a significant discrepancy of 5 σ [1].

other possibility is given by the Zemach proton radius (R_Z), which is a convolution of the proton charge ρ_E and magnetic dipole ρ_M momentum spacial distribution:

$$R_Z = \int d^3\vec{r}|\vec{r}| \int d^3\vec{r}' \rho_E(\vec{r}')\rho_M(\vec{r}-\vec{r}'). \tag{1.2}$$

Considering this scenario, composed of different and sometimes also incompatible values of the charge proton radius, it is clear that there is the need of new experiments and methods. In this context, the FAMU (Fisica degli Atomi MUonici) experiment represents an additional attempt to the measurement the Zemach proton radius using the muonic atom spectroscopy in a peculiar and original setup. In the following chapters a complete review of the FAMU experiment will be presented starting from the methods selected, the data analysis of the data collected, the design of the final setup of the experiment, the data acquisition system and the development of the laser system.

Chapter 2

Fisica degli Atomi Muonici (FAMU)

2.1 Methods

This chapter describes the FAMU experimental methods and the tests performed to prove it. Also, the procedure I used for the analysis of the data is described, using, as an example, the data collected with the argon-hydrogen mixture.

2.1.1 Zemach Radius from transfer rate measurement

The FAMU experimental method to measure the Zemach radius of the proton is based on the precise determination of the energy gap between the two hyperfine energy levels of the muonic hydrogen ground state. The energy difference between the singlet (1^1S_0) and triplet (1^3S_1) levels of the ground state 1S is theoretically predicted to be 0.1828 eV and it can be measured exploiting the dependence from the muonic hydrogen energy of the muon transfer rate to heavier atom. This method requires a few steps:

- formation of muonic hydrogen atoms: the hydrogen atoms capture the muons, produced by the accelerator, forming muonic hydrogens;
- thermalization: the muonic hydrogen thermalizes to the ground state through a collisional thermalization process;

- laser injection: the spin flip is induced by the exact wavelength of the laser beam;
- muon transfer to an high-Z contaminant: after the de-excitation the following spin flip, the remaining kinetic energy of the muonic hydrogen increases the transfer rate probability of the muon to oxygen;
- X-rays emission: the oxygen de-excites emitting X-rays which are detected by a set of dedicated detectors.

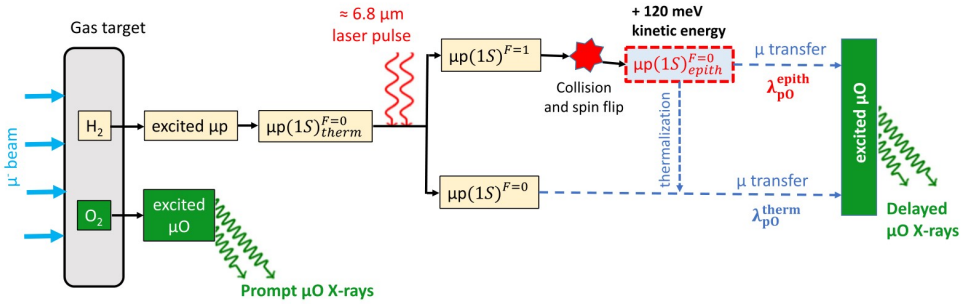

Figure 2.1: This scheme represents the FAMU experimental method. An event starts with the arrival of the muon spill, continues with the capture of the muons in the gas target and the laser shot and ends with the emission of the X-rays produced by the high-Z contaminant (in this drawing oxygen) after the transfer of the muon from the hydrogen.

The process is schematized in figure 2.1. First of all, a target pressurized container filled with a gas mixture of hydrogen and high-Z contaminant is placed on a low energy muon beam to form muonic hydrogen (μp). An important aspect that concerns the target is to maximize the μp formation rate by choosing an appropriate gas density and the muons energy. Muonic atoms are also formed with the high-Z contaminant, but these de-excites rapidly during the first phases of the experiment. Once the muon is captured by the hydrogen atom, the formed system de-excites reaching the ground state following two different paths. Around 25% of the μp thermalizes directly to the ground state singlet F=0. The remaining 75% reaches the final singlet state through a collisional thermalization process from the middle triplet state (F=1) in 300 ns [10].

Once the μp has reached thermalization, the spectroscopy experiment can be then performed on the μp. A narrow linewidth mid-infrared laser exactly tuned to the energy gap between the state F=0 and F=1 illuminates the μp inducing the quantum leap between the two energy levels. A certain percentage of the μp de-excites back colliding with the other H_2 in the target to the F=0 singlet state, and, during this process, around the 2/3 of the transition energy is converted to kinetic energy, which remains to the μp.

At this point, these muonic hydrogens have about 0.12 eV of kinetic energy and collide with other molecules inside the target. During these collisions a muon can be transferred to another atom and, with a certain probability, to the high-Z contaminant atom. The rate of this transfer directly depends on the kinetic energy which the μps have after the de-excitation, but this kinetic energy is present only if the laser light was able to induce the spin flip between the F=0 and F=1 states. Hence, collecting information on the transfer rate is equivalent to acquire information about the effectiveness of the laser. In particular, the experiment is focused on measuring the variation of this rate as a function of the laser wavelength. The transfer rate can be measured observing the rate of the de-excitation X-rays produced after the transfer to the high-Z contaminant. When an atom with high-Z captures a muon from one of the μps, the muon de-excites to the ground state emitting a characteristic X-rays that can pass through the target container and can be collected by an external X-rays detector. Since the focus of the experiment is the measurement of a rate, the speed and time accuracy of the detectors are of primary importance.

The process described above occurs over a time period of 4000–5000 ns. We can divide this time span in two parts. The first, called prompt phase, includes the X-rays emissions produced by the first interactions of the muons beam with the target materials and by the direct capture of the high-Z contaminant.

The prompt phase occurs simultaneously with the arrival of the beam and continues for about 150–300 ns after it. The duration of this phase, as well as of the other, directly depends on the gas conditions (temperature and pressure), the gas vessel materials, and the characteristics of the muon beam. The data collected during this phase are then also used for the energy calibration of the detectors as they contain very defined lines, mainly produced by aluminium and nickel.

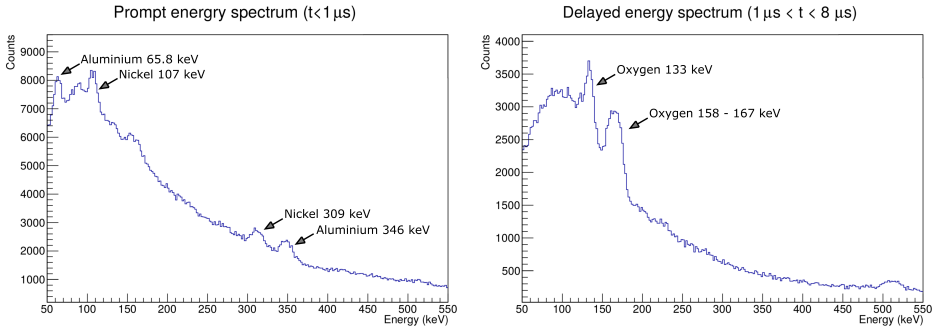

Figure 2.2: The two plots show the different energy spectra between the prompt and delayed signals collected during an oxygen measurement. On the left the prompt lines produced by nickel and aluminum. On the right the K-lines of oxygen.

The second phase, called the delayed one, is the most important for the experiment. In fact, it consists of the emission of the X-rays produced by the oxygen which participates to the process described before. The difference on the energy spectra of the two phases can be appreciated in figure 2.2, where different energy lines are visible in the first and second time window. The first plot on the left shows the energy spectrum produced by the aforementioned aluminium and nickel materials of the vessel. The plot on the right shows the delayed phase and the de-excitation X-rays line produced by the high-Z contaminant, in this case oxygen.

The precise measurement of the transfer rate value is important for the FAMU experiment and for this reason a preparatory measurements campaign was performed before the final experiment. The preparatory work was focused on the measurement of the transfer rate of the muon to a set of possible high-Z contaminants, in different pressure and temperature conditions and, on the test of the various parts of the FAMU apparatus, especially the detectors. The measurement of the transfer rate is paramount to choose the ideal physical conditions of the target. The next sections describe how to extract this important value from the data of the delayed phase.

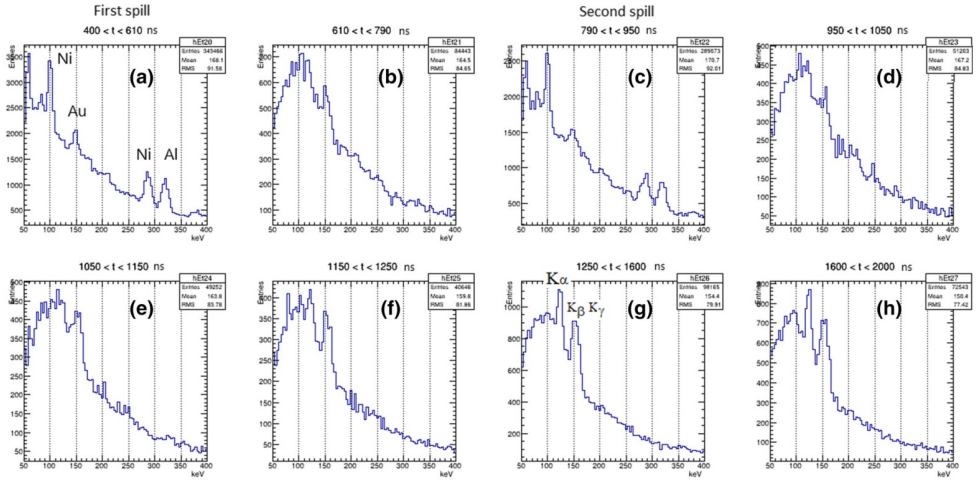

Figure 2.3: Examples of histograms of time frames covering from the prompt to the delayed phase. The first three histograms (a-c) show the arrival of the muon beam and the prompt phase. In the last histograms (d-h) the delayed energy spectrum produced by the high-Z contaminant (oxygen) is shown.

2.1.2 The extraction of the transfer rate value

The transfer rate is obtainable from the analysis of the data collected in the delayed phase of X-rays emitted from high-Z contaminant. In order to grant the end of the prompt phase, a time window is chosen starting 150 to 300 ns after the muon arrival.

These data are then further divided into time frames. The analysis of each single time frame allows the extrapolation of a time trend of the arrivals of the X-rays from the muon transfer to the high-Z component of the gas. In figure 2.3 eight histograms represent an example of this analysis, covering both the prompt and the delayed phases. Histograms (a) and (c) correspond to the first and second bunch of muons, that are separated by 300 ns and correspond to the prompt phase. Comparing the plot (c) and (h) a strong difference in the spectral lines can be seen: plot (c) shows the prompt X-rays produced principally by the aluminium and nickel of the target structure, while plot (h) shows X-rays lines produced by the high-Z contaminant, in this case oxygen, after the transfer.

The number of these time frames and their lengths depend on the to-

tal number of events and, the larger the statistics, the more granular the time frame will be. For each single time frame the background spectrum collected from a measurements with pure hydrogen is subtracted, thus obtaining the X-rays produced by the high-Z contaminant in the delayed spectrum only. An integration of the obtained spectral X-rays lines is performed. By doing this procedure for each time frame, we can reconstruct a time evolution curve of the signal X-rays during the delayed phase. The obtained graph can be fitted with an exponential curve which contains the information on the time evolution of the transfer phenomena at that temperature. The analysis delivers the rate of disappearance of muonic hydrogen atoms λ_{dis}, which varies with the density of the target ϕ, the concentration of the high-Z contaminant, the concentration of deuterium, naturally present in pure hydrogen, the concentration and the formation of ppμ molecular ions. In fact, the disappearance of the muons occurs with different rates depending on the process and on the "branching ratio" of each of these. The rate of disappearance λ_{dis} can be written as:

$$\lambda_{dis} = \lambda_0 + \phi(c_p\Lambda_{pp\mu} + c_d\Lambda_{pd} + c_Z\Lambda_{pZ}). \tag{2.1}$$

In this formula:

- λ_0 is the disappearance rate of muons due to decays and nuclear captures;
- $\Lambda_{pp\mu}$ is the rate of the formation and c_p is the concentration of the ppμ molecular ions;
- the Λ_{pd} is the transfer rate of the muons to deuterium and c_d is its concentration;
- Λ_{pZ} is the value that we are looking for, the transfer rate of the muons to the high-Z contaminant;
- c_Z is the concentration of the high-Z contaminant gas.

The concentration c_Z becomes a major parameter to adapt the rate of disappearance of the muonic atoms to the need of the experiment. The λ_{dis} can be found from the exponential graph obtained before evaluating the variation of the number of hydrogen atoms $N_{\mu p}$ versus time using the following formula:

$$dN_{\mu p}(t) = S(t)dt - N_{\mu p}(t)\lambda_{dis}dt, \tag{2.2}$$

in which the last unknown is $S(t)$, the initial number of muonic hydrogen generated after the formation of muonic hydrogen. Combining the two formulas 2.1 and 2.2, it is possible to calculate the Λ_{pZ} transition rate.

An example of the full process can be found in section 2.2, where the full data analysis that I performed on the argon is described.

2.1.3 Calculation of the Zemach radius from the transfer rate variation

The key point of the method to measure the proton's Zemach radius is to evaluate the variation in the transfer rate between an event with and without laser injection in the target. As it has been explained in 2.1.1, if the wavelength chosen to illuminate the target is not the right one able of induce the spin-flip, the transition rate will not vary. If, on the other hand, a variation of the transition rate will be observed, it means that the energy corresponding to the wavelength is the right one to produce the spin-flip. The experiment is focused on the search of the right wavelength by methodically scanning the wavelength range around the most probable values [11]. An example of this transition rate difference can be seen in figure 2.4, where the red and the blue curves show the difference of the X-rays counting rate from high-Z contaminant with and without the correct wavelength light injected in the target optical cavity. The effect of the laser is directly correlated to the probability of inducing a spin flip in the target. This probability (P) depends on the energy of the laser beam (E), or in other words on the number of photons injected in the target, on the cross section and on the reflectivity of the mirrors of the multipass optical cavity (S and R) and on the temperature of the gas in the vessel (T). To summarize this [12]:

$$P = 2\ 10^{-5} \quad \frac{E}{(1-R)\ S\ \sqrt{T}}. \tag{2.3}$$

The relation to calculate the hyperfine splitting starting from the Fermi energy ΔE^{hfs} is:

$$\Delta E^{hfs} = E_F(1 + \delta^{QED} + \delta^{rec} + \delta^{Z} + \delta^{pol} + \delta^{hvp}). \tag{2.4}$$

In this formula some of the values are known or measured with high precision, up to 10^{-6}, as the lowest order Fermi hyperfine energy E_F, the QED

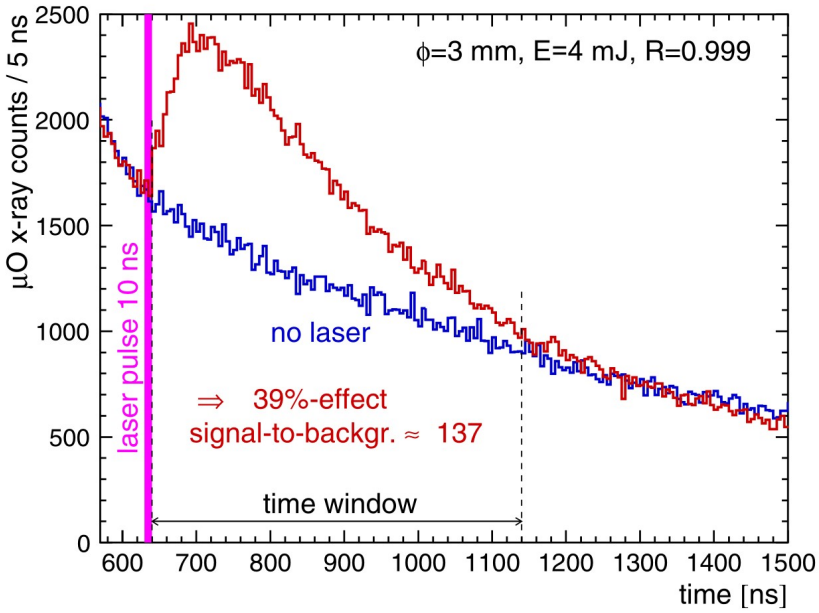

Figure 2.4: The plot shows a simulation of the difference between the μO X-rays time evolution curve with the laser, in red, and without the laser in blue, supposing a laser energy of 4 mJ and ϕ=3 mm represent the beam diameter and R=0.999 the reflectivity of the mirrors.

corrections δ^{QED} and recoil correction δ^{rec}. The hadron vacuum polarization δ^{hvp} is small compared to the other correction and can be neglected. The other two free values are the proton polarization δ^{pol}, which from the experimental data and theoretical calculation is $(4.6\pm 0.8)\times 10^{-4}$, and the Zemach radius term δ^{Z}. This term is calculated as:

$$\delta^{Z} = 2\,\alpha\,(1+k)\quad \frac{M_\mu\,M_p}{M_\mu+M_p}\,r_Z, \tag{2.5}$$

where α is the fine structure constant, k is a QED correction and M_p and M_μ are the masses of respectively the proton and the muon. The only free parameter remaining is the Zemach radius r_Z.

The aim of the experiment is to increase the data accuracy of the Zemach radius measurement experiments achieving a precision of 1% or better, only limited by the accuracy of the δ^{pol} parameter [11].

2.2 Verification of the FAMU experimental method

2.2.1 Physical target development

In the previous paragraphs, I presented the theoretical description of the experiment, without focusing on the mechanical and electronics specification of the FAMU apparatus. The central part of the experiment is the target in which both the muons and the laser are injected. Until now the focus was on the target as a compressed and cooled gas mixture. From this moment there will be a clear distinction between the *physical target*, intended as the gas mixture, and the *experimental target*, the apparatus which will contain the gas mixture. The *experimental target*, which I will call FAMU Target System, or TS, is formed by a cryostat hosting the pressure vessel which will contain the hydrogen-based gas mixture, the *physical target*. Once placed in front of the muon source, we have the formation of muonic hydrogen. At the appropriate time the laser beam is injected through the *experimental target* into the *physical target*, where it is reflected by an optical cavity, confining the light within the volume where muonic hydrogen is formed. In this phase the muon transfer to the high-Z contaminant can take place, with the subsequent emission of characteristic muonic line X-rays.

The first goal for the TS is to stop as many muons in the gas mixture as possible, allowing them to form the muonic hydrogen atom. This stopping rate is related to: the muon beam energy, the thickness of entrance window and the gas density. A high gas density increases the stopping rate of the muons in the gas and also increases the transfer rate of muons between muonic hydrogen and the high-Z contaminant. The experiment must be optimized between this two effects. The transfer rate value is the key variable of the entire experiment, as the FAMU method is focused in maximizing the variation of this value with and without the laser beam.

The transfer rate depends not only on the energy of the muonic hydrogen, which is the dependence that we are going to exploit, but also depends on the various other characteristics of the gas target, such as:

- the choice of high-Z gas contaminant (the chemical specie of the gas affects the transfer and also gives different signals of de-excitation);
- the quantity of the high-Z gas contaminant (if increased it gives a growth of the transfer rate);

- the density of the gas (which varies the distances between the gas molecules).

The FAMU collaboration, through two target prototypes, tested those parameters to determine the ideal target characteristics. This measurement campaign was divided in two parts. In the first part, different gas based on hydrogen mixtures with a variety of contaminant as oxygen, carbon dioxide and argon were tested. In the second part of the campaign, the high-Z contaminant concentration, the temperature and pressure values were scanned in order to verify the proposed experimental method and in particular the muon transfer rate from hydrogen to the contaminant as a function of the temperature.

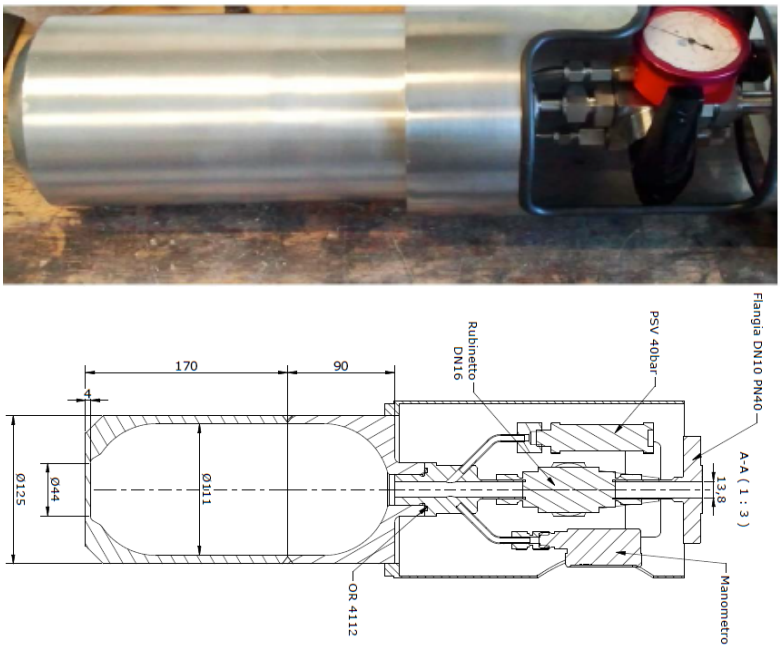

Figure 2.5: The picture and the related CAD drawing representing the first FAMU test target used during the data acquisition of 2014. As can be seen, it was a simple pressurized vessel with the necessary piping. This target allowed to test the proposed detection system with muonic oxygen X-rays.

First FAMU test target The first target was a simple pressurized gas container, shown in figure 2.5, made by an aluminium cylinder capable of

withstanding high pressure, up to 40 bar, with an aluminium thinned entrance window to minimize the stopping of the muons. The cylinder was around 30 cm long and it gave the possibility to maximize the stopping rate of the muons inside the target as a function of the energy of the muon beams. This target was used only in the 2014 data taking and it was primarily developed to study the behavior of the FAMU selected detectors.

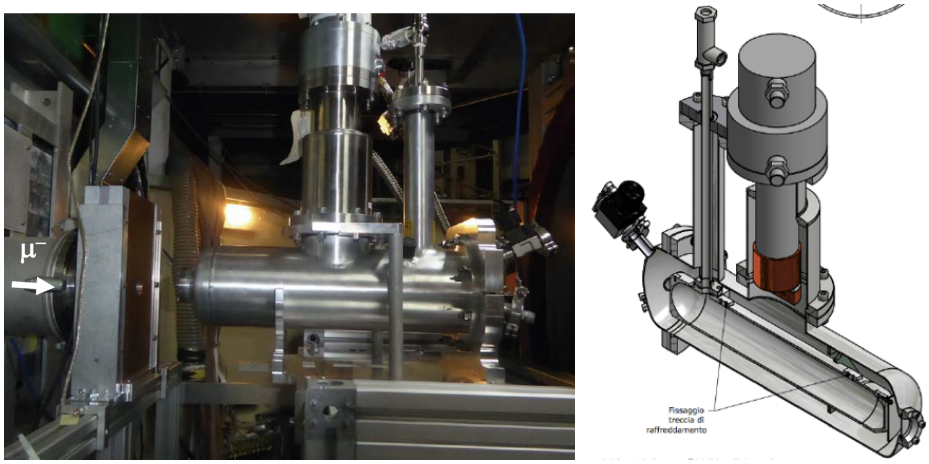

Figure 2.6: The image shows the 2016 FAMU target. The photo portraits the target placed in front of the muon beam. The CAD drawing shows the internal scheme of the target.

Second FAMU test target The second FAMU experimental target was more complex and capable to control the internal temperature. The system was based on an aluminium cryostat containing the gas pressurized vessel. The cryogenic gas target was built to minimize the heat exchange with the environment through a vacuum volume and a multi-layer thin aluminized mylar blanket able to further screen the irradiated heat, as can be seen in figure 2.6. In order to screen also the thin muons entrance window (0.8 mm of aluminium) from heat exchange and still further minimizing the muon absorption, a dedicated infrared radiation screen based on aluminium foils was placed in the vacuum. The internal gas vessel, made of the same aluminium of the external cryostat was connected to a cold finger capable of maintaining a constant preselected internal temperature in a range between 40 K and 300 K. Since the decay electrons produced by

the muons can increase the background noise due to their interactions with other materials and detectors, the internal surface of the vessel was coated with a thin layer of nickel and gold to absorb the muons before reaching the aluminium. In fact, the mean lifetime of the muon in the muonic aluminium is comparable to that of the muonic hydrogen and the muon will decay mainly during the delayed phase of the measurement. The internal temperature was controlled by four temperature sensors placed in pairs on the vessel and on the cold finger. Basing on the data from these sensors, a system based on the Lakeshore 336 Cryogenic Temperature Controller started and stopped the heater, which was placed on the gas vessel, to keep the temperature constant. If needed the 100 W heater could also be used to heat the gas vessel.

Simulations were performed before building the targets to understand where it was possible to reduce thicknesses to improve the muons entrance and to choose the best material to avoid unwanted X-rays lines on the energy spectra. Examples of these simulations performed with the GEANT 4 program are shown in figures 2.7 and 2.8. The first plot shows how the target length was specifically designed to stop most of the muons in the gas, while the second histogram shows the material source of the X-rays collected by the detectors. This histogram shows how the materials chosen for the target were and are very important to decrease the signal-to-noise ratio of the experiment.

2.2.2 2014-2018 FAMU measurements

The primary goal of these experiments was to test the FAMU proposed method to measure the transfer rate. These tests also gave the possibility to evaluate and select the best candidate as a high-Z contaminant for the hydrogen mixture. The possible gases to be selected for this role were oxygen, argon, carbon dioxide and methane.
In figure 2.9 we see the spectra collected with an hydrogen-argon gas mixture with the 2014 gas target. The upper panel shows the spectrum collected with a High Purity Germanium detector (HPGe), while the lower panel shows a spectrum collected with $LaBr_3$ detectors. The peaks corresponding to the muonic X-rays line of the various elements are evident. The lower panel demonstrates that the fast $LaBr_3$ detectors are apt to collect the energy spectra and its time evolution in the energy region useful

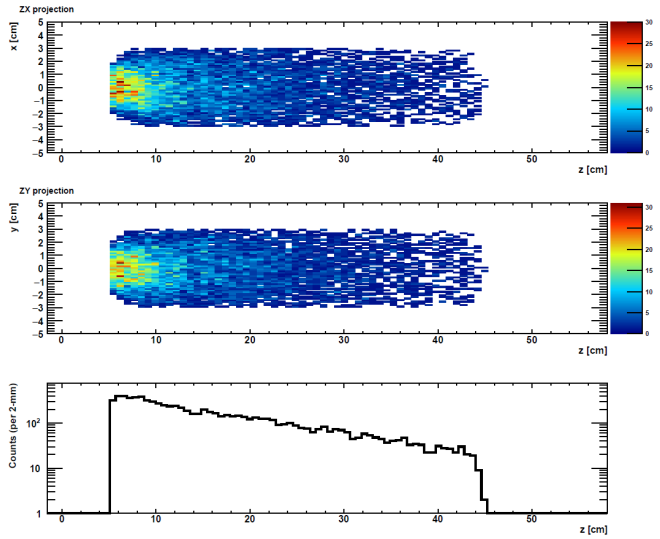

Figure 2.7: The simulation, as result of a calculation made with GEANT 4, shows the expected behavior inside the two FAMU test targets. The group of image shows the internal stopping point of the muons inside the first gas target.

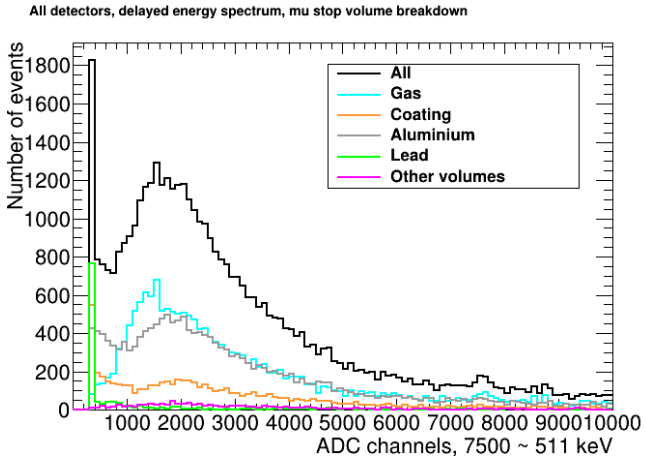

Figure 2.8: The result of a simulation made with GEANT 4, showing the source of the X-rays collected by the detectors. As can be observed, the aluminium stops most of the muons. The optimization lays on maximizing the stops in the gas.

for the experiment. The HPGe, while having a better resolution, is too slow to acquire the data of the experiment.

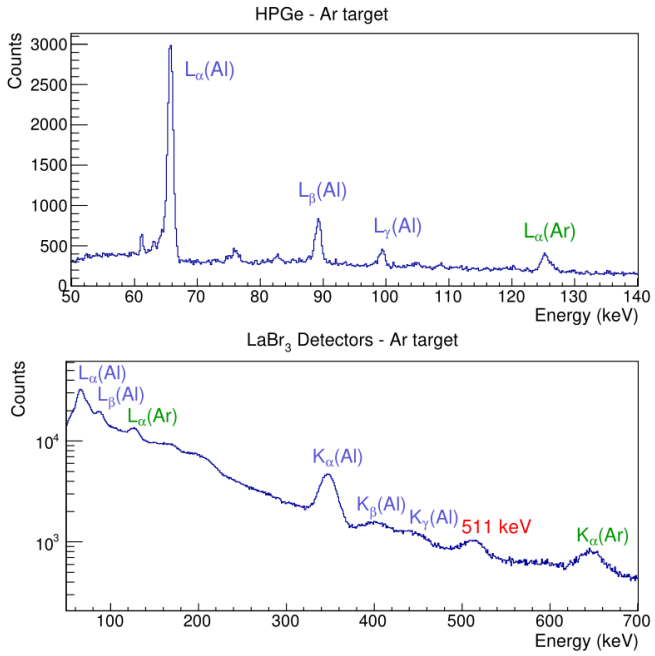

Figure 2.9: The two spectra in figure show the X-ray peaks produced by the de-excitation of the muonic argon used as a high-Z contaminant. They are collected using two different detectors: the upper panel with a High Purity Germanium detector, while the lower panel with a $LaBr_3$ detector.

In the 2016 data acquisition, the full set of gases was tested. An extensive measurement campaign was planned, which provided important data to better understand the ideal high-Z contaminant. Figure 2.10 gives in a glance a clear vision of the measurement progression performed during 2016 with the FAMU target able to set different temperatures. As can be seen, many gas mixtures were measured at different temperature. We can see the development of the various measurements as a function of time and temperature. The test on pure hydrogen was performed to have a reference or background for the other measurements, while nitrogen was used only to clean the target. As can be seen, also different concentrations and temperatures were tested, and argon and oxygen were extensively measured

down to 100 K.

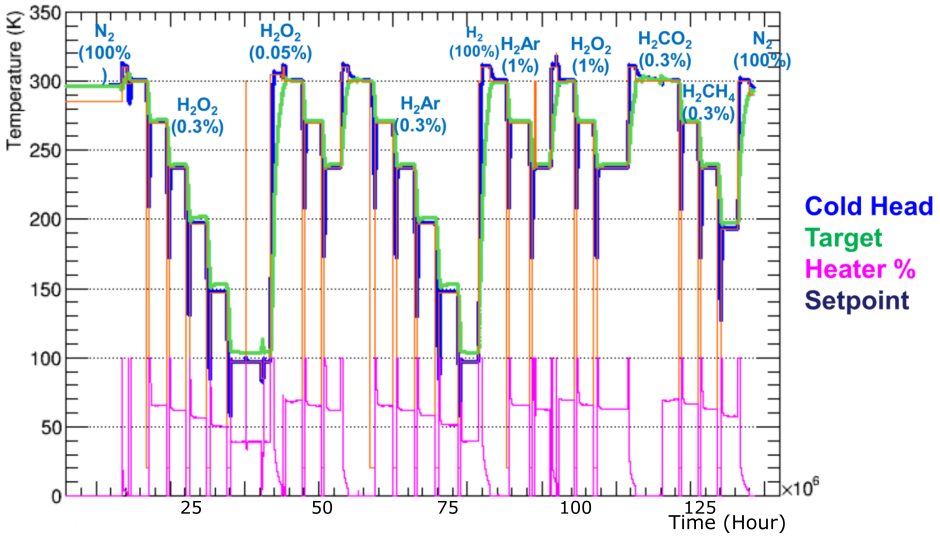

Figure 2.10: This plot shows the temperatures in the target as a function of time in the progress of a five days measurement campaign. Initially the gas target was flushed with nitrogen, then evacuated and filled with the gas mixture to be measured. The first mixture that can be observed from left to right is H_2 with 0.3% of O_2, which was measured in six steps from 300 K to 100 K. Then the gas target was brought back at 300 K and the mixture was replaced with one having a lower concentration of oxygen (0.05%). Few steps in temperature were enough to have an evaluation of this mixture. Subsequently an Ar 0.3% mixture was loaded in the target and measured with the same temperature progression used for the first mixture. Similarly, measurements were done with various concentration of Ar, O, CO_2 and CH_4.

The objective of this procedure was to extract the dependence of the transfer rate on the temperature. Keeping in mind that temperature and density of the target are bounded, the energy at which the transfer mechanism arises is bound to the target temperature. In this way we could verify the effect on the transfer rate rising the energy of the μps by means of the excitation of the hyperfine splitting transition. In fact, the effect of the laser prompting the hyperfine splitting transition corresponds to delivery

an energy of 0.183 eV which, after de-excitation of the μp, leaves a residual energy of 0.12 eV. This residual energy would correspond to the energy available to a μp in a target brought to a temperature of a 1000 K, while for a target temperature around 300 K we can reach a μp energy equivalent only to 0.05 eV [13]. While changing the target temperature, the FAMU detectors collect a variation of high-Z contaminant X-rays rate allowing to calculate the dependence of the transfer rate on the temperature, taking into account the variation of the gas density. The preliminary measurement performed during the 2016 data acquisition indicated oxygen as a good choice for the high-Z contaminant. Oxygen exhibited the most marked variation of the transfer rate as a function of the temperature, which demonstrated that oxygen makes the whole FAMU measurement possible. On the contrary, Ar and CH_4 were discarded due to the flat behavior of the transfer rate.

Having collected this crucial information about the dependence of the transfer rate on the temperature, the definition of the final working conditions will be based on the optimization of various parameters: the target temperature, pressure and high-Z contaminant concentration.
As described in 2.1, these parameters have to be reciprocally optimized to perfection the progression of the experiment from the moment of the μp formation, to the laser light injection and to the observation of the X-rays after the muon transfer. For example, the contaminant concentration c_z needs to be fine tuned, avoiding high values which would result in a too fast transfer rate, but also low values which, on the other hand, would strongly reduce the muon transfer. The gas mixture density should be ideally the highest possible, in order to increase the muons stopping rate. Nevertheless, high density values could work only if the contaminant concentration is tuned accordingly. The temperature should be the lowest possible, above the condensation temperature of the gas mixture, to maximize the transfer rate (as reported in formula 2.3) in fact, as mentioned, this value is dependent on the temperature.
Considering the above-mentioned parameters and respective requirements, and having fixed the temperature and the gas density (therefore even the pressure), the high-Z contaminant concentration is the parameter that can be changed to vary the transfer rate.
The following sections goes into details of the analysis of two data set, showing the different temperatures dependence of the transfer rate of the two gas mixture, argon and oxygen.

2.2.3 Temperature and transfer rate to argon

During my PhD I had the possibility to analyze, in depth and with high accuracy, the data collected in 2016 using a gas mixture made of hydrogen and argon. The aim of my work was to calculate the transfer rate of muons as a function of temperature from muonic hydrogen to argon. From the theoretical calculations this gas should behave similarly to oxygen, with a strong dependence of the transfer rate on temperature. It seemed to be an optimal candidate for this purpose, and it also had de-excitation X-rays energies of 127.6 keV, 171.8 keV and around 200 keV for the L-lines and 643.7 keV, 770 keV and around 850 keV for the K-lines. In fact those characteristics allow the position of the X-rays lines in the center of the linear range of the $LaBr_3$ detectors and, in addition, the relatively high energy avoids consistent absorption by the various material layers. The dataset to be analyzed consisted of a full day of data collection, with around 3.5 million triggered events and more that 20 million signals from the detectors. The program analyzed the amplitude of the pulses, which was then calibrated in energy, and the time of the pulse arrival. Aside from them, the online DAQ system collected also the temperature of the target and the time of the event. The data were taken at 300 K, 270 K, 240 K, 200 K, 151 K, and 105 K.

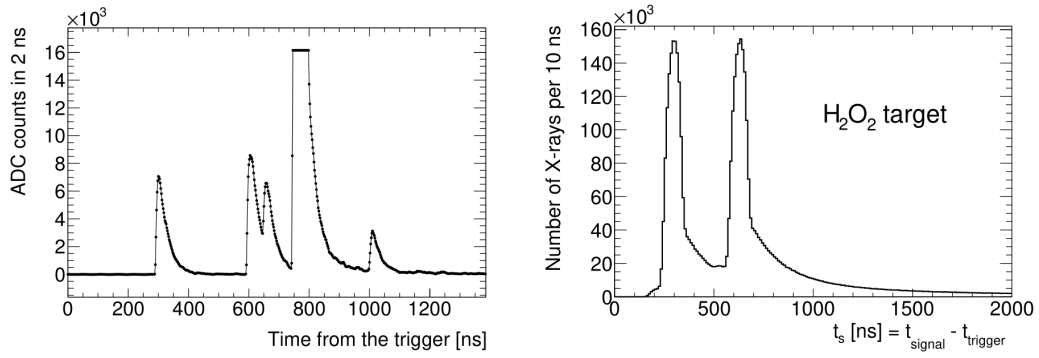

Figure 2.11: On the left, a standard waveform signal from a $LaBr_3$ detector as collected by the digitizer. On the right, the histogram of the arrival time of the X-rays, measured as the start of the peaks. The two peaks on that histogram are the effect of the arrival of the muon bunches in the target.

The analysis started from the raw data collected during the 2016 data acquisition and in particular I focused on the data collected on a gas mixture with a 0.3% argon concentration. The data were analyzed using the FAMUAnalysis software with routine able to measure the height and the timing of the peaks looking to the variation of the derivatives of the electronic signal. An example of these pulses is visible in figure 2.11: the plot on the left shows a digitized signal with different pulses for a single event triggered. For every pulse the program measures the arrival time of the X-ray, as the starting point of the pulse, and the energy of the X-ray, as the height of the pulse. The right plot shows the histogram of the arrival time of the X-rays. The two peaks on that histogram are the effect of the arrival of the muon bunches in the target.

Once the height/energy and the timing of the X-rays have been measured some cuts are applied to remove mis-reconstruction of the pulses and other fluctuations. The events which are removed may be the ones with a higher or lower than normal baseline and the not isolated events, in which the peak height reconstruction is imperfect, for example due to the presence of other peaks. After this process some preliminary plots can be already produced showing, as it is visible in figure 2.12, a reconstruction of the energy spectrum in most of the detectors, with the expected peaks distribution in the prompt and delayed phases.

Subsequently, a calibration based on recognized X-rays lines, the aluminium and nickel in the prompt phase and argon in the delayed phase, was performed. The result was crosschecked with the calibration made before the data acquisition with a set of X-rays sources as ^{137}Cs and ^{57}Co, to check the consistency of the calibration obtained. The calibration curves showed the expected quadratic behavior, as shown in figure 2.13.

This calibration curve points were measured by an automatic peak recognition and fitting algorithm used on the spectra of each single detector. This code is able to fit a complete portion of the spectra near to the recognizable peaks with known energy lines. The calibration curves extracted were plotted from these data and fitted with a quadratic function, showing a similar behavior on most of the detectors. Only one detector was discarded due to the low resolution of the spectra, derived from some defects on the electronics readout.

As a result of the calibration a good alignment of the peaks from the spectra of different detectors was obtained, demonstrating the quality of the calibration method and giving the possibility to merge the events col-

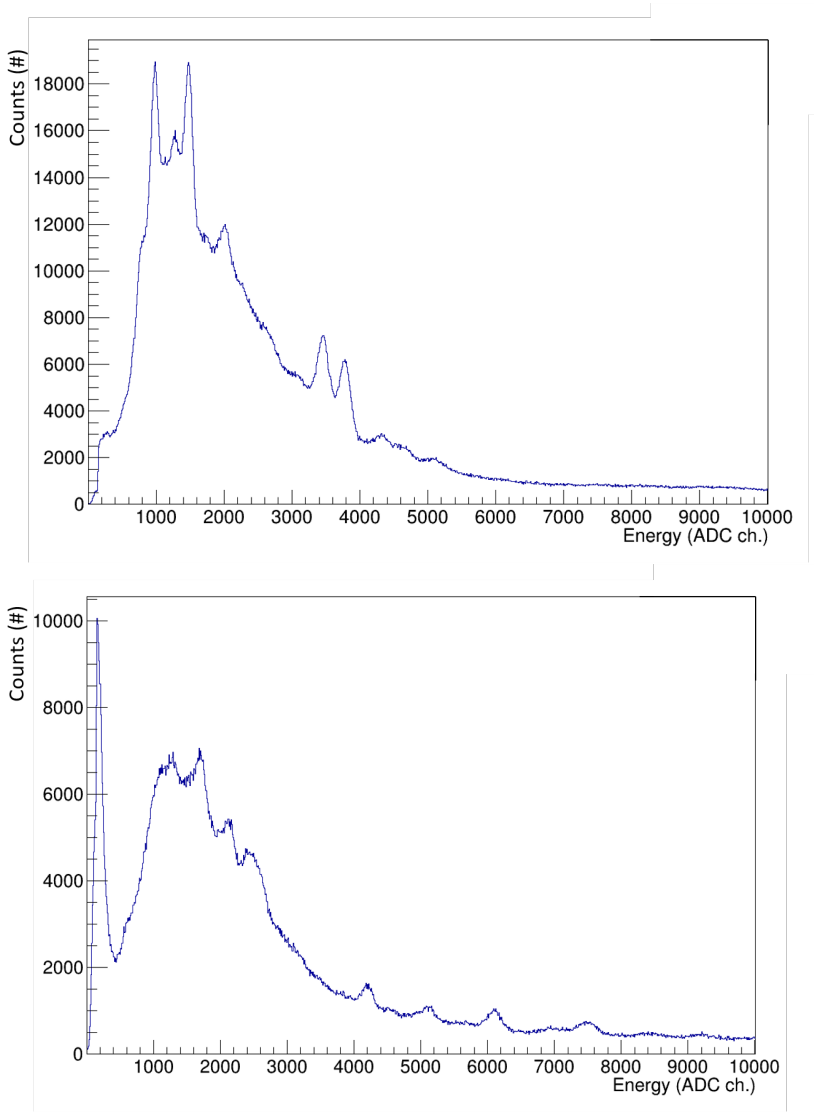

Figure 2.12: On the top, the prompt spectrum of the H_2-Ar gas mixture, showing principally the aluminium and nickel prompt X-rays lines around 800–4000 ADC ch. (30–350 keV), while on the delayed phase (bottom image) the argon de-excitation X-rays lines with at low energy, the K-lines at 1200–3000 ADC ch. (120–200 keV), and at higher energy, the L-lines at 5500–10000 ADC ch. (640–900 keV), are visible.

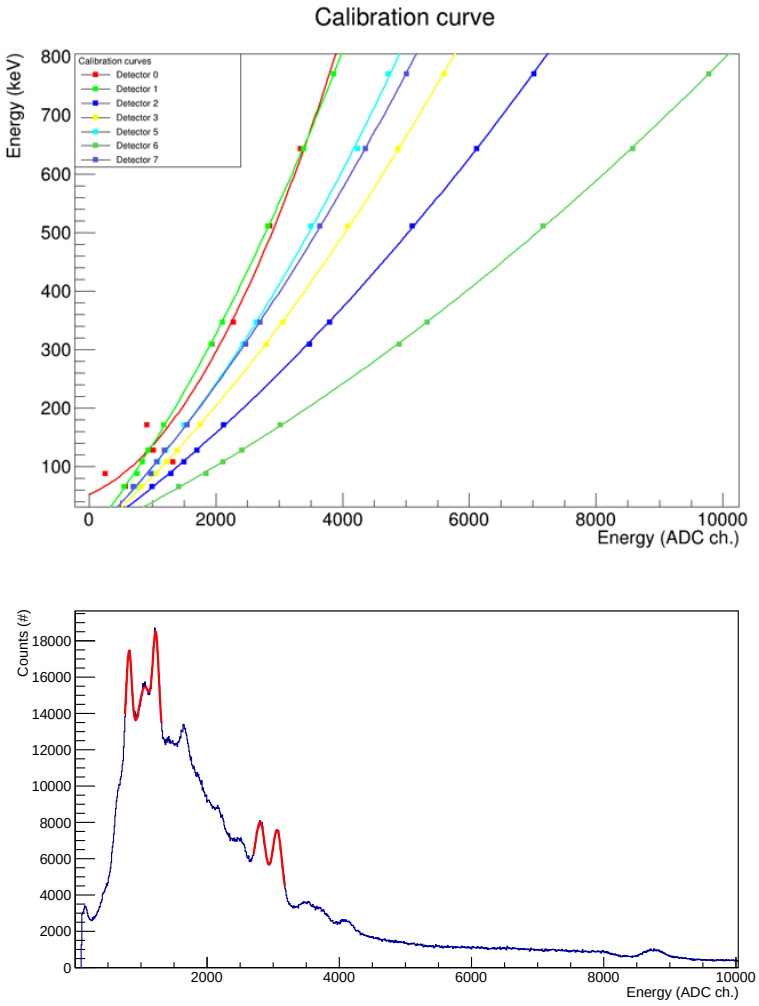

Figure 2.13: The first plot (top) shows the calibration curves for all the $LaBr_3$ detectors used during the 2016 data acquisition. The plot on the bottom shows an example of the quality of the peaks fitting algorithm on the prompt phase on the energy spectra. The peaks from the prompt and delayed phase are then reported with the theoretical energy value on the first plot and fitted with a quadratic curve.

lected by all the detectors in one single spectrum with the full statistics of the data acquisition. The result of the sum of the events can be seen in figure 2.14.

As previously mentioned, the FAMU method is focused on the transfer rate of the muons from the thermalized muonic hydrogen atoms to the high-Z contaminant atoms. For this reason the data analysis is performed on the delayed phase of the experiment, i.e. 300 ns after the second muon bunch, when the muonic hydrogen reaches the ground state. For the measurement of the transfer rate to argon we are interested on the X-rays produced by high-Z contaminant only. To count them, they have to be isolated from the background X-rays produced by the de-excitation of the other elements which are present in the target. These unwanted X-rays can be subtracted from the argon spectrum using as background sample the pure hydrogen spectrum, which is taken with the same procedure described before. These two spectra have to be normalized and there are three possibility to choose a reference normalization window on the two spectra. There are three possibilities:

- after the K-lines of the argon, i.e. after 900 keV.
- between the L-line of the argon and the 309 keV of the nickel;
- under 60 keV before the first visible peak of the carbon;

All these possible solutions have some weakness, as shown in figure 2.15. The first solution, the "high energy" normalization, seems to be the more promising one, but the low statistics acquired does not allows a good normalization and when we look at the low energy range, the argon L-lines peaks are all cut under the background. In this method only the argon K-lines can be used to measure the transfer rate, loosing more than a half of the already low statistics.

The issue with the second possible solution, or the "medium energy" normalization is that it is not known if the normalization is performed in a range of energy where there are not left, or low energy, tails of the argon K-lines. A left or low energy tail was observed in the data collected with the oxygen mixture, where part of the X-rays produced by the de-excitation of the oxygen are not fully reconstructed by the detectors due to energy loss in the crystals. The effect was then studied and reconstructed with GEANT 4 simulations. An argon K-lines left tail is expected because this effect should

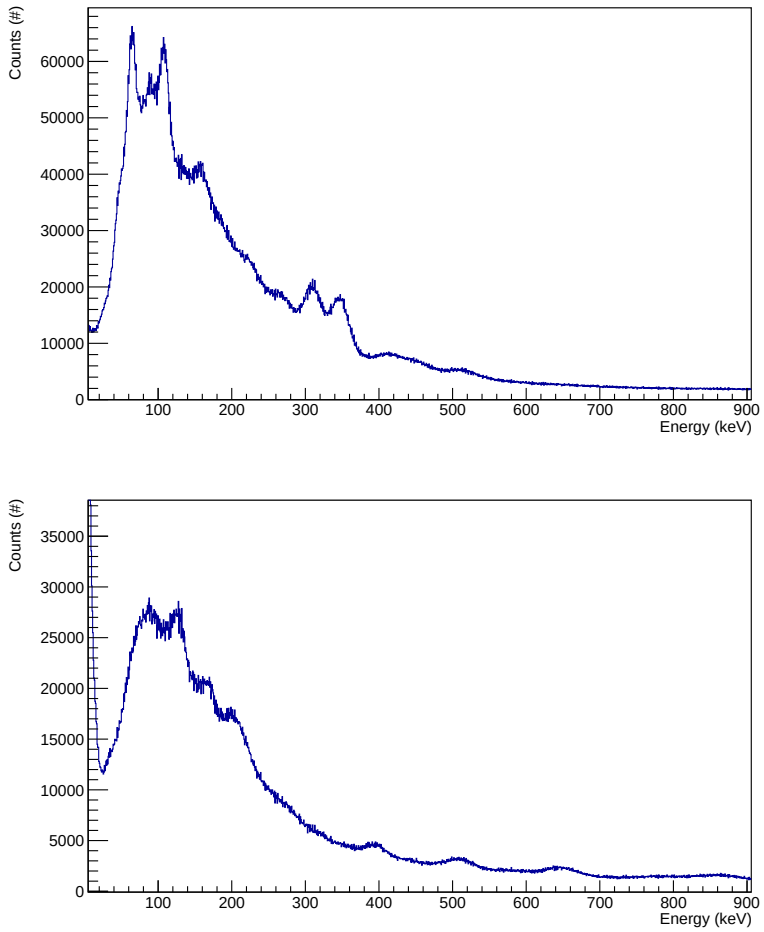

Figure 2.14: The two histograms are the energy spectra collected by all the detectors and calibrated in energy. The first plot (top) represents the prompt phase, the second one (bottom) the delayed phase.

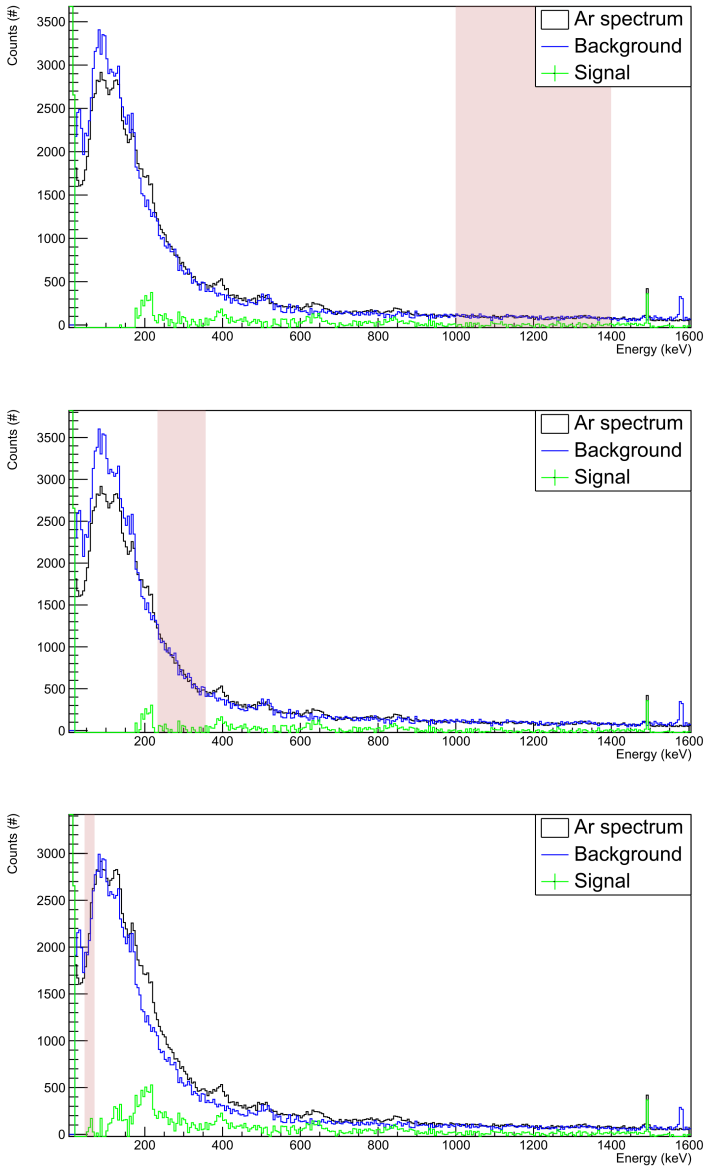

Figure 2.15: In this picture there are the three examples of normalization used during the data analysis with highlighted normalization ranges. From the top, there are the normalization in the "high", "medium" and "low" energy. Changing the normalization of the background, the height of the peaks change and in some cases the peaks are completely cut.

be more marked with higher energy X-rays. For this reason a simulation campaign has been started, trying to simulate the experimental result of the 2016 data acquisition, similarly to the simulation already done with the oxygen. The work on simulation is still ongoing. Like in the case of the "high" energy normalization, with the "medium" energy normalization the background cuts most of the argon L-lines, giving a similar result to the one before, probably underestimating the argon de-excitation event. The third case, or the "low energy" normalization, the issue is that the reconstruction is not well performed as the energy spectrum due to the absorption of part of the low energy X-rays in the target layers, giving some doubt on the quality of the normalization. The second issue is similar to the one of the "medium energy" normalization method. Fitting after the argon L-lines, there is not certainty that the background is not normalized on the low energy left tail of the L-lines.

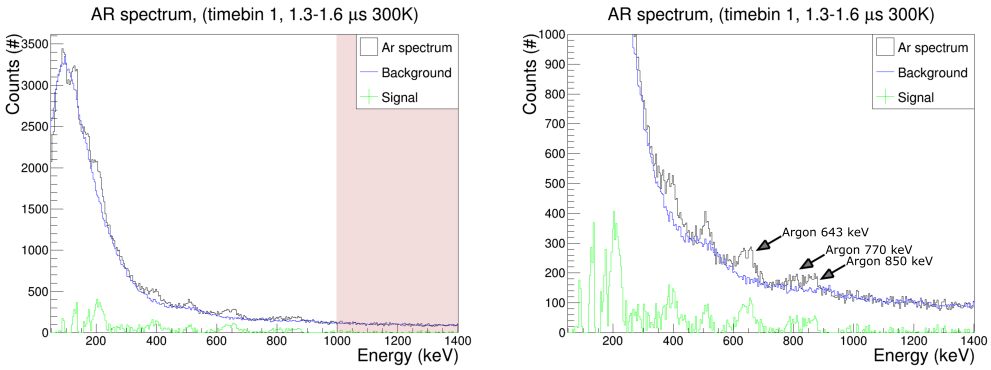

Figure 2.16: An example of the "high energy" normalization applied on the spectrum at 300 K. On the left the complete spectrum, while on the right a zoom of the peaks of the argon K-lines (highlighted).

In this paragraph the results obtained with the "high energy" normalization, which are not sensible to the left tail issue, are presented. The other two normalizations were used to estimate the systematic error of the measurement and are included in the table 2.1 and figure 2.19. In order to face the low statistic problem I also attempted the use of a smoothing algorithm with the technique of the Gaussian kernel [13]. With this method I was able to obtain the plots in figure 2.16. In the first (left) plot the full energy spectrum is shown with the background already normalized and the result of the subtraction (in green) in which the various peaks are visible. At this

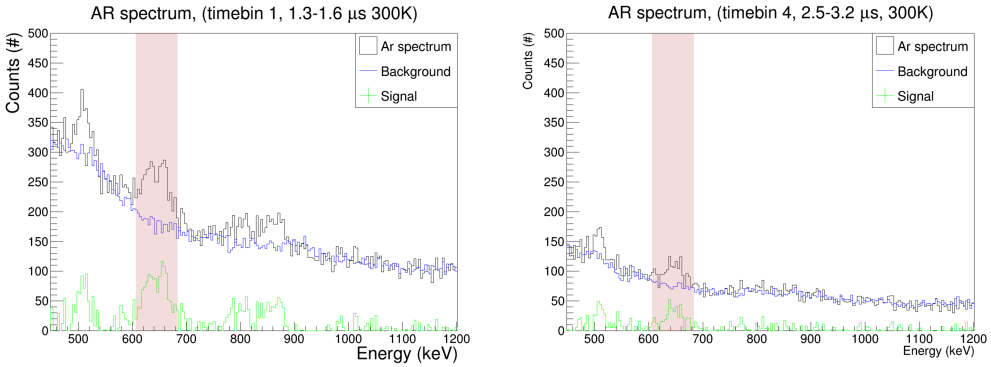

Figure 2.17: The two plots show the argon delayed energy spectra in two different time bins after the thermalization of the muonic hydrogen. Comparing the two plots it is evident the difference of the height of the argon K-α line peak (highlighted), which is more prominent in the first time bin. The variation of this peaks is used to create the time evolution of the argon X-rays produced by the transfer rate.

point only the argon K-α line is surely not cut by the choice of the normalization, for this reason a strong selection is applied considering only the K-α line at 642 keV to be used in the next steps. This choice can be seen in the second plot in figure 2.16.

As we are interested in the time evolution of the X-rays, the delayed phase is divided in a set of time bins, and for each time bin an energy spectrum is plotted. The time bins are strictly correlated to the total statistics of the data acquired. The integral of the count of argon X-rays for each time bin is then corrected by the time bin width. By comparing the energy spectra taken from different time bins, as shown in figure 2.17, a different height in the argon lines is revealed, giving a glimpse of the time evolution of the argon X-rays.

By integrating the histograms resulting from each time window around the 642 keV K-α line and plotting them in function of the center time of the time bin, can be obtained the time evolution curve of the argon de-excitation X-rays. An example of the time evolution curves can be seen in figure 2.18, where the argon time evolutions produced with the target at 300 K and 105 K are plotted. If the slopes of the curves are different, there will be the possibility of a temperature dependence of the transfer rate. In the case of argon we conclude that the slopes are very similar (written in

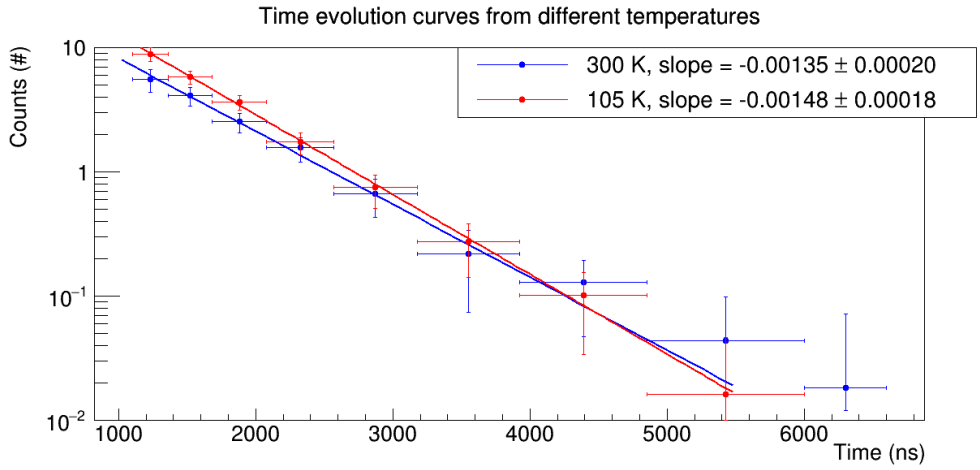

Figure 2.18: The X-rays time evolution depends on the transfer rate, which depends on the temperature of the target. In this case the two time evolutions are very similar, which is a hint of the argon transfer rate temperature independence.

the figure 2.18), within the error, hence there is no clear dependence.

At this point, with a selected density, fixed using the temperature and pressure, and concentration, the transfer rate $\Lambda_{pO}(T)$ can be calculated by fitting the curve of the argon time evolution using the functions 2.1. This process is repeated for each temperature value, obtaining a set of transfer rate values. As anticipated, the transfer rate is calculated by fitting the points of the time evolution curve from every time bin. The graph in figure 2.19 can be obtained by plotting the resulted transfer rate versus the temperature of the target together with the result of [14], even considering the large errors due to statistics and systematic on the background measurement, we can conclude that there is no strong temperature dependence of the transfer rate, demonstrating that argon cannot be considered a suitable high-Z contaminant for the FAMU experiment.

Temperature (K)	Transfer rate ($10^{10}s^{-1}$)	Transfer rate error ($10^{10}s^{-1}$)
300	20.84	4.13
270	19.01	4.60
240	19.82	4.17
200	21.10	4.29
150	22.72	3.80
105	25.76	3.30

Table 2.1: Argon transfer rate values and associated errors at different temperatures. In the errors the statistic and systematic on the background measurement are already included.

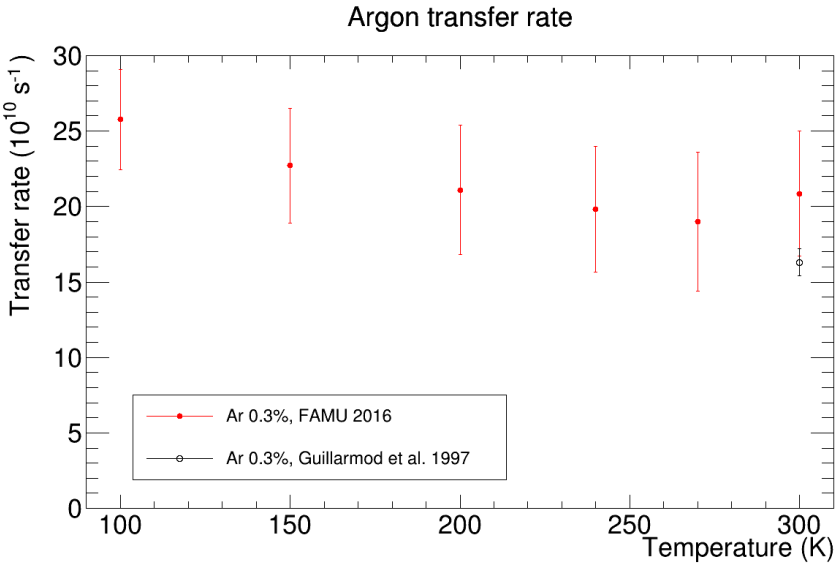

Figure 2.19: The plot shows the measured transfer rate vs temperature. The variation of the transfer rate due to the temperature is minimal. In the errors the statistic and systematic on the background measurement are already included. The plot also reports a transfer rate value from [14].

2.2.4 Transfer rate to oxygen and the final choice

As anticipated, the oxygen transfer rate shown a strong dependence from the temperature of the gas mixture, becoming a possible candidate as a high-Z contaminant for the FAMU experiment. The transfer rate of this gas was extensively measured and tested during the data acquisition of 2018, using different concentrations between 0.05% to around 5%, at different temperatures from 50 K to 330 K and with different pressures from 5 bar to 40 bar. The result of these data analysis were published in [13] and [15].

The data analysis followed the same process described in the previous section. As a consequence the description will not cover in depth the analysis, but will focus on some significant graphs only.

Immediately after the formation of the muonic hydrogen and the subsequent atomic cascade, the μp reaches the ground state with an initial energy. It thermalizes during following collisions and this phase is called epithermal phase. For this reason, to measure the transfer rate as a function of temperature we used a time window allowing to select only transfer events arising after the μp thermalization. Figure 2.20 shows a typical example of the epithermal phase, represented by different slopes in the initial part of the time evolution curve. During this analysis, this part was removed and we chose as a delayed phase the one starting just after the change in the slope. The time evolution curve for the transfer rate to oxygen taken at different temperature is visible in the plot evidencing different slopes.

As in the case of argon, the background normalization range of oxygen spectra was at "high energy", above the oxygen peaks energies. An example of the energy spectrum produced after the subtraction of the background is showed in figure 2.21, where the difference between one of the first time bins peaks heights and the one of the subsequent time bins can be appreciated. The variation of these peaks is used to create the time evolution of the oxygen X-rays produced by the transfer rate.

In addition, other data under 100 K were collected at 70 and 80 K. Other data under the oxygen freezing point of oxygen were discharged because of the clear drop of the transfer rate due to the condensation of the oxygen from the gas mixture and its deposition on the walls of the vessel. Also new data were collected at 323 and 336 K.

At these temperatures, the same analysis to measure the transfer rate

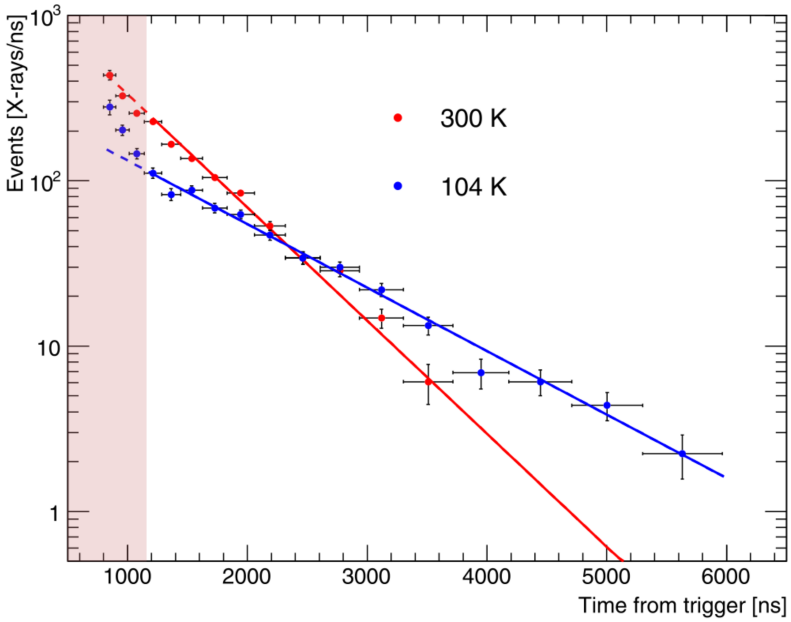

Figure 2.20: The X-rays time evolution depends on the transfer rate, which depends on the temperature of the target. A typical example of the difference between the X-rays time evolution curve can be appreciated in the image, where the slope of the 300 K target is more pronounced than the 104 K curve. The blue curve before 1300 ns shows also the effect of the epithermal phase.

was performed, but in this case the high-Z contaminant concentration with respect to hydrogen was altered by other factors. Thanks to the already known curve taken with the 2016 data, the transfer rate points were recalibrated on this data obtaining also the data on the concentration. For the cold side data the concentration was $1.61 \pm 0.11\%$, while for the warm side data was $0.51 \pm 0.06\%$. Those concentrations are not shown in the graph like figure 2.22 because is already normalized in the value. In this case, differently from the case of argon, the transfer rate dependence from the temperature is strong. This graph demonstrates the feasibility of the FAMU experimental methods and it is used to decide the final concentration, temperature and pressure of the gas target.

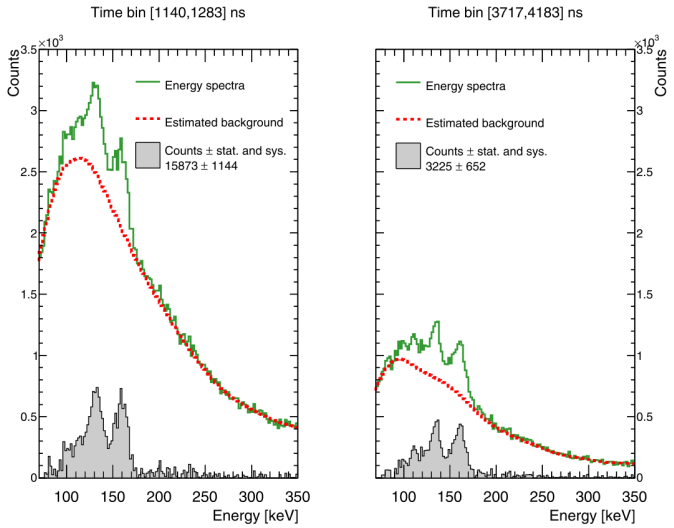

Figure 2.21: The two plots show the oxygen delayed energy spectra in two different time bins after the thermalization of the muonic hydrogen. Comparing the two plots it is evident the difference of the height of the oxygen peaks, which are more prominent in the first time bin.

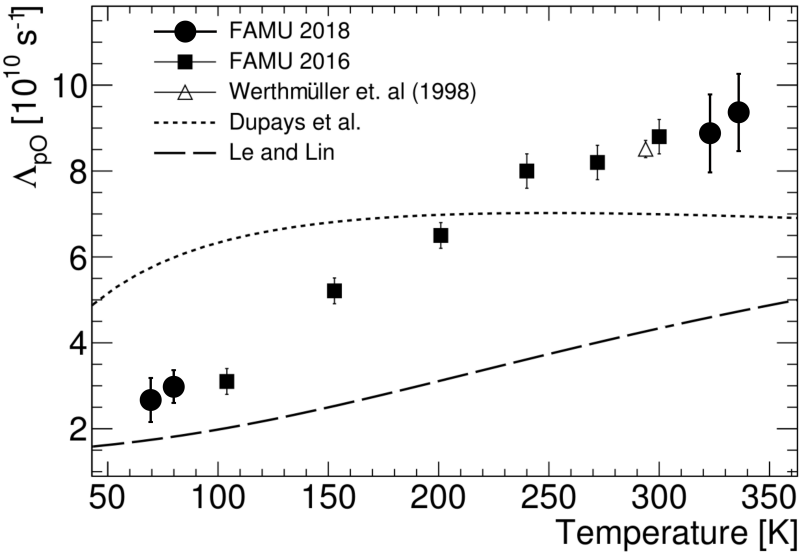

Figure 2.22: Transfer rate versus temperature, extended also at low and "high" temperature.

Chapter 3

FAMU experimental setup

A complex apparatus is required to perform the FAMU experiment with the method described in the previous chapter. This apparatus is made of devices which were developed by a team of scientists belonging from different areas of physics, such as nuclear physics, particle physics, laser physics and materials science. The final setup of the experiment is the result of a development path, started in 2014 with the first target prototype and the first test beam. In these years the devices were tested and modified to better fulfill the final experimental requirements. This chapter describes the FAMU experimental setup, focusing on the features that make each part optimal for this experiment.

3.1 The apparatus

Figure 3.1 shows a CAD drawing of the final apparatus. The beam pipe, shown in red, injects the muons into the gas target, which is surrounded by the detection system. The mid-IR laser source is placed on the optical table, under the safety covers. The laser light is transported to the target through a vertical tube. The DAQ system, which collects all the data necessary for the analysis, is also an important part of the experiment and it is not shown in the CAD drawing.

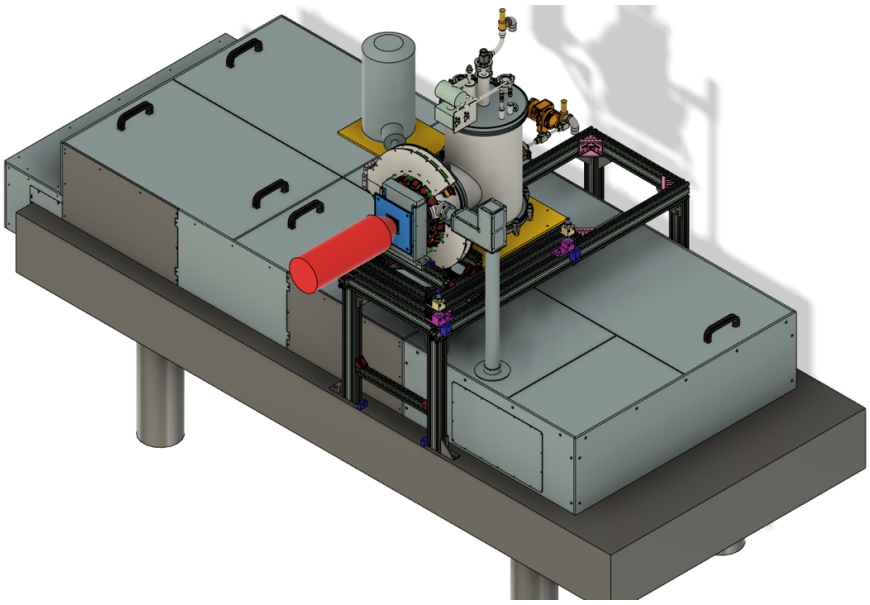

Figure 3.1: This CAD drawing presents the full FAMU setup composed by the cryogenic target, the detector arranged around the target and the laser setup covered by the safety panels.

3.2 Muon beam

The peculiar operating principle of the experiment requires a pulsed and reliable muon beam for the production of muonic hydrogen. The Rutherford Appleton Laboratory (RAL) [16] provide us the required muon source at the RIKEN-RAL facility at ISIS [17]. Located in the Oxfordshire countryside, RAL is home to the ISIS Neutron and Muon Source, a synchrotron that accelerates protons up to 800 MeV from which it produces neutrons and muons. The protons are sent along a vacuum pipe to a carbon target, where, due to the interactions, pions are emitted. The pions rapidly decay into muons, which are then focused in beams directed to the RIKEN-RAL experimental rooms. As shown in figure 3.2, the ISIS accelerator supplies protons to two target stations, TS1 and TS2. The four RIKEN-RAL experimental rooms, or "Ports", are located in TS1.

The ISIS accelerator provides a pulsed proton beam with a 50 Hz rate, but the protons bunches are split between the two target stations TS1 and TS2 respectively with a ratio of 4:1. The result of this split is that the final

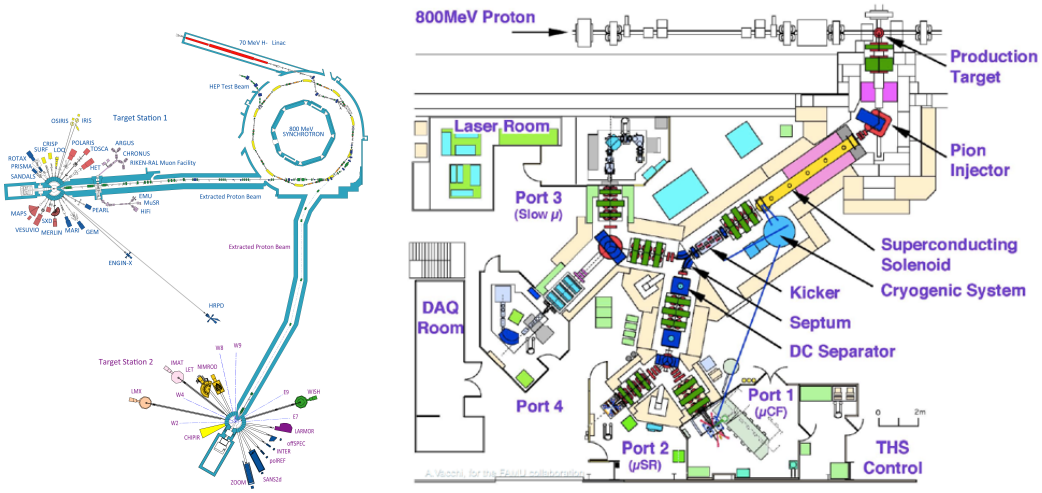

Figure 3.2: The scheme of the ISIS facility and the muon factory RIKEN-RAL facility at RAL, Chilton, UK. The FAMU experiment is placed in the Port 1.

beam arriving at Port 1, the experimental room where FAMU is located, is formed by four muon bunches spaced 20 ms apart and there is a 40 ms delay before the next pulse. All bunches made by two pulses with a length of 70 ns each. The distance between the two pulses is 320 ns.
The muons momentum can be varied between 30 and 80 MeV/c with a momentum spread of 4% FWHM. The energy of the beam depends on the target design. In our case, FAMU needs muons around 58 MeV/c. By increasing the energy of the beam, decreases the number of muons stopped in the entrance window, however the muons will hit the gas. The final value of the beam energy was selected through a series of simulations and during the previous measurement campaign. The aim was to maximize the number of muons stopped inside the target.

3.3 Experimental target

In sections 2.1 and 2.2, I have already introduced the target as a gas, consisting of mixture of hydrogen and a high-Z contaminant. This gas, the physical target of the experiment, will be contained in the TS. The TS serves several functions, such as:

- containing the gas in a very precisely controlled environment;
- maintaining the right condition to stop the muons in the target;
- confining the beam of light coming from the laser to illuminate the muon hydrogen;
- allowing the X-rays produced by the de-excitation of the oxygen exiting the TS to be collected by the X-ray detectors, which are placed around it.

The parameters that can be changed to fulfill all these purposes are:

- gas temperature and pressure: gas conditions change the number of muons stop in the gas mixture and at the same time have an impact on the transfer rate which must be tuned to observe the signal within $\sim$1 μs from the beam arrival;
- thickness of the muon window entrance: must be minimized to avoid the spread of the beam and the subsequent loss from side walls;
- high-Z contaminant concentration: the amount of the gas added to the hydrogen varies the timing of the observed X-rays lines;
- X-rays transmission efficiency: the use of the lightest material possible for the gas container and cryostat maximizes the number of observed X-rays;
- noise reduction: the use of heaviest material possible for the gas container and the cryostat allows to minimize the number of muons, due to nuclei muon capture, in the delayed phase. The smaller the number of muons, the smaller the noise induced by the electrons coming from muon decay.

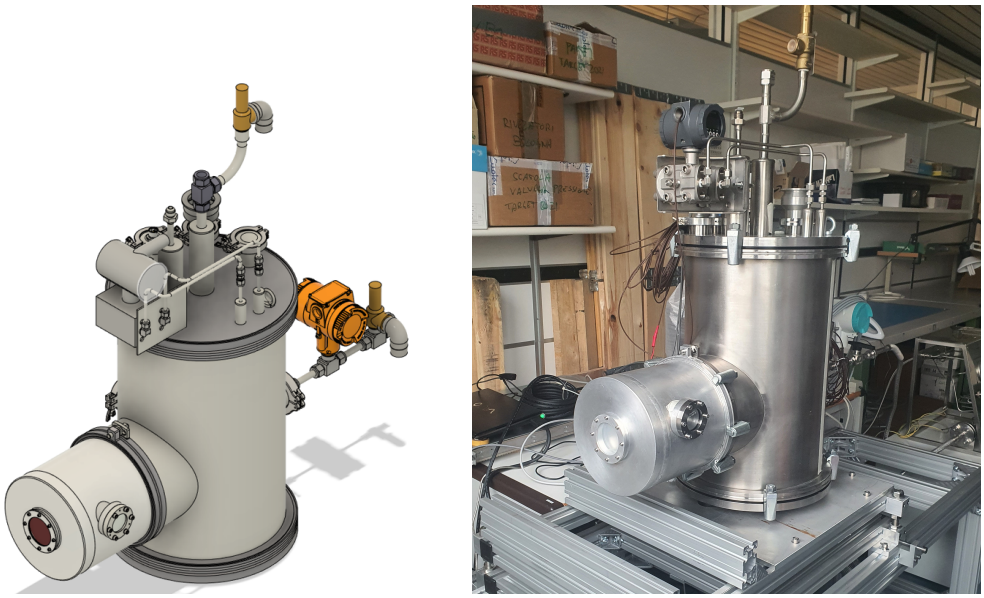

Figure 3.3: These two images show the FAMU target system (FAMU TS), as developed with a CAD drawing and in the final realization.

The final design of the target, a synthesis of all the simulations and experiments carried out in recent years, is the one shown in figure 3.3. The external visible surface is a single large vacuum insulation cryostat that contains the vessel with the gas target and the reserve of liquid nitrogen to keep the gas at the desired temperature of 77 K. The front cylindrical part, which contains the gas vessel and has to allow the passage of the X-rays, is 2 mm aluminium thick. The rest of the cryostat is made of stainless steel. Numerous tubes are visible on the outer surface of the cryostat. In the upper part there are the tubes necessary for filling and measuring the level of the liquid inside the nitrogen tank. On the rear side (the side opposite to the muon entrance window), there are the tubes for making the cryostat vacuum and the tube connected directly to the vessel, which will contain the physical gas target. This tube is used to fill the vessel with the hydrogen/oxygen mixture. The electrical connection on the side of the TS allows to connect the temperature probes and to power the resistor that heats the bottom of the liquid nitrogen tank.

The internal physical target is contained in a pressure-tight vessel that

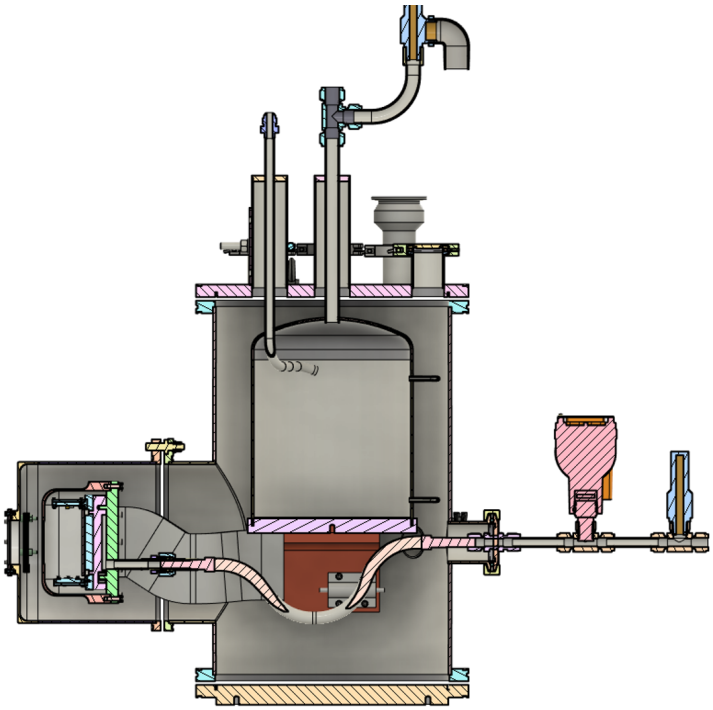

Figure 3.4: This CAD drawing shows a complete section of the FAMU TS. From the left: the muons entrance window, the gas pressurized target, the liquid nitrogen container and the pipe to fill the target with the gas mixture. All this parts are inside the vacuum cryostat.

encloses the optical cavity. Figure 3.4 shows a section of the CAD target where the internal structure of the TS is visible: the pressure-tight vessel, the liquid nitrogen reservoir and the copper braids. The braids cool the target to the same temperature as the reservoir. This vessel consists of a milled aluminium block with a 2 mm thick surface. The particular shape was developed so that the volumes of the vessel and of the optical cavity coincide as much as possible. In this way, the gas inside the target that will not be exposed to the muon beam and/or illuminated from the laser is minimized. The vessel thickness is also important for minimizing the oxygen de-excitation X-rays absorption and 2 mm is the minimum thickness needed for a pressurized vessel. This component is able to withstand up to 10 bar and is sealed by a specific indium gasket. The working pressure

during the experiment is 7 bar. The internal surface of the vessel is coated with two thin layers of nickel and gold to decrease the background noise produced by the aluminium capture of the muons. The lifetime of the muons in muonic aluminium is comparable to the lifetime of the muons in the muonic hydrogen. This similarity causes the decay electrons of the muons of the muonic aluminium to give signals during the delayed phase, increasing the background noise. To minimize this noise, a thin layer of gold reduces the number of muons interacting with the aluminium. Gold is an optimal choice for this task, in fact the muon is quickly captured by the nucleus in about 80 ns, removing the background from the delayed phase.

The optical cavity is fixed at the rear of the gas vessel, exactly at the height of the entrance of the laser beam. This choice was made to minimize misalignment of the laser beam with respect to the optical cavity, due to possible thermal behavior of the different components. To further decrease this potential issue, the optical cavity support is made of Invar alloy, known for its very low coefficient of thermal expansion. A lead panel is fixed on the support of the optical cavity, to absorb the muons that pass through the entire target without being stopped by the gas.

One of the important features of this target is the possibility to inject the laser beam directly into the pressurized gaseous target cooled by liquid nitrogen. Concerning the laser injection in the target, the three main challenges are the laser alignment, the minimization of vibrations and the need to reduce the heat exchange with the outside while using only one optical window to let the light beam in. The first point will be explained on the next section, where the laser target injection system will be described. With regard to the vibrations, these can cause misalignments in the internal cavity, resulting in decreased efficiency. To minimize the vibrations, the target is fixed directly to the laser table which has a passive damping system.
Regarding the heat exchange, the optimal solution to thermally insulate the target, is the use of two optical windows, one that closes the gas vessel and an external one that closes the cryostat. However, to minimize laser light absorption, it was decided to use only an optical window in CaF_2, which becomes the only separation between the external environment and the cold gas inside, as can be seen in figure 3.5. The interior of the gas vessel is also visible in the CAD drawing, showing the optical cavity and lead panel. The particular shape and position of the insulating tube is the key to

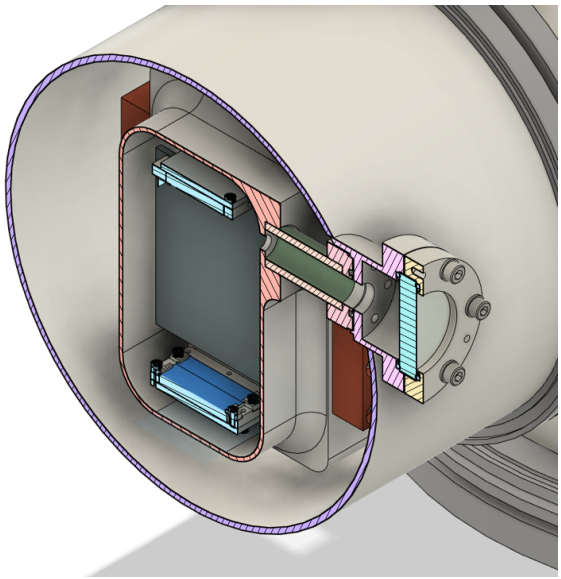

Figure 3.5: This CAD drawing shows the peculiar system which sustains the pressurized vessel. The entrance of the laser beam is on the right.

avoid potential thermal transmissions from the gas target to the windows by minimizing the convective motions of the gas.

3.4 Detector system

The challenge of collecting as much X-rays as possible from muonic oxygen capture is the goal of the FAMU detection system. In the chapter 2.1 the importance of a rapid collection of X-rays data has been underlined, in fact we are not interested in all the X-rays produced during the trigger event, but we focus on the delayed emissions that are produced 100 ns after the muons arrival. The X-rays produced by the oxygen are at 133 keV, 158 keV and 167 keV, but the detector covers the energy range between 100 and 700 keV thus providing not only the data, but also the lines produced by the emission of the other target material like nickel and aluminium which can also be used for calibration. These X-rays are emitted isotropically from the center of the target, increasing the importance of maximizing the solid angle covered by the detecting system. As for the target, also in this case the detector setup was developed in a long series of tests, as it will

be described in the section 4.2 . A set of fast X-rays detectors based on $LaBr_3$(Ce) scintillation crystals can fulfill this requirement while offering the required energy resolution and a good linearity in the energy range of the emission from the FAMU target. These detectors are divided into two groups according to the system used to collect the scintillation photons produced in the crystals: one part of the detectors uses photomultiplier tubes (PMTs) (developed by INFN Bologna) and the other is based on a silicon photomultiplier (SiPM) array (developed by INFN Milan-Bicocca). In addition to these, the system includes also a high-purity germanium (HPGe) detector for high-precision cross-checking of the energy spectra collected by the fast scintillation detectors and a hodoscope to monitor the size and shape of the muon beam at the entrance of the target. All these detectors are arranged around the TS, as can be seen in figure 3.6, with scintillation detectors placed in rings around the target, the hodoscope in front of it, and the HPGe on the side.

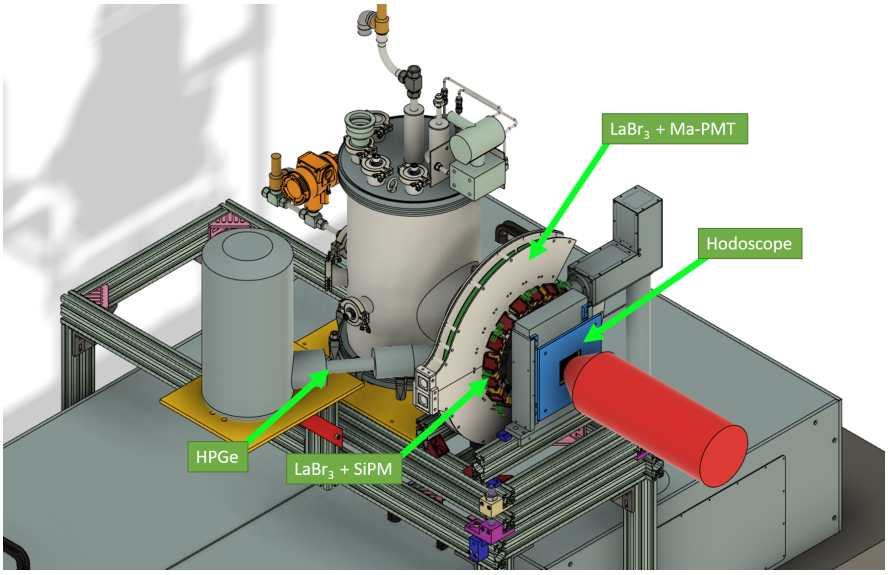

Figure 3.6: The drawing shows the locations of the various detectors placed near to the target. Of the three $LaBr_3$ detector rings only two are visible around the target, while the third one is hidden behind the central Bologna's detectors. The hodoscope is in front of the target and the HPGe on the side.

Detector based on $LaBr_3$(Ce) scintillation crystal

As anticipated, the $LaBr_3$(Ce) scintillating crystals can satisfy the requirement of the experiment, with an energy resolution of 7% at 140 keV and 4% at 511 keV, a decay time at 97% of 16 ns and a peak light emission at 380 nm. The first ring of detectors assembled and tested are based on

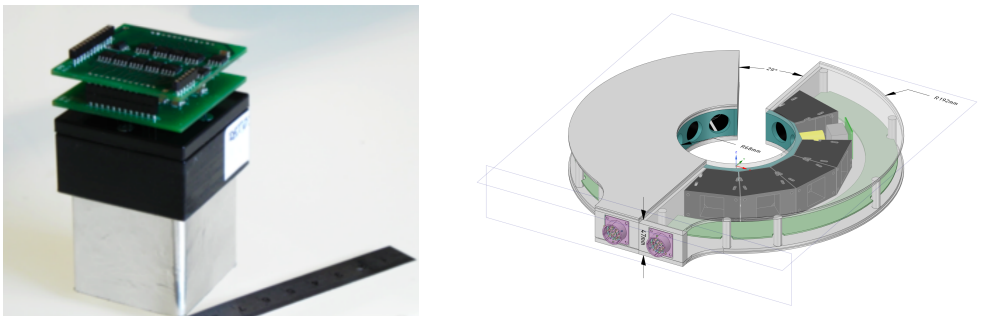

Figure 3.7: On left, a $LaBr_3$(Ce) detector read by PMT. On the right, the CAD showing the final ring assembly.

12 cylindrical 1" crystals read by a set of Hamamatsu R11265-200 PMT, developed by INFN Bologna. These detectors, shown in figure 3.7, are circularly arranged pointing towards the center of the target and fixed with an aluminum support around the cryostat. The scintillation crystals are shielded on the lateral surfaces with an aluminum profile to minimize the noise produced from the other directions and focusing on the X-rays coming from the muonic atoms formed inside the target. The signals from the PMT are shaped to produce optimal pulses covering the full dynamic range of the acquisition system, which consists of a set of 500 MHz CAEN V1730 digitizers connected to the FAMU Data Acquisition System. The rough calibrations and tuning of these detectors and DAQ are performed using the 662 keV line of ^{137}Cs, the 356 keV of ^{133}Ba and the 122 keV of ^{57}Co, while the data calibration is performed directly with the known lines of the spectra acquired during the data acquisition. By using data themselves for the calibration it is possible maximize the energy resolution taking into account the detector behavior in time. This choice for the calibration is a clever solution and can also minimize the error due to a possible gain variation. In an ongoing development, a new readout system for this detector ring is being tested. This new on-board digital pulse processor able to work at

1 Gs/s and to perform zero suppression is positioned directly in the ring, minimizing the distance route of the signals.

Maximizing the X-rays collected by increasing the solid angle covered by detectors is of primary importance for the experiment. For this reason other 28 detectors, organized in two rings, were developed. These structures are placed in the forward and backward side of the INFN Bologna's detectors.

Figure 3.8: A $LaBr_3$(Ce) detector read by SiPM. The 3D printed cases of these detectors are designed to be disassembled for a fast check.

Similarly to the previous detectors, the 28 Milano's detectors are also based on $LaBr_3$(Ce) scintillating crystals, but the readout is based on silicon photon multipliers: 18 crystals are equipped with a 4×4 array of 3×3 mm^2 Hamamatsu S14161 SiPM, while the remain part uses a 4×4 array of 3×3 mm^2 Hamamatsu S13161 SiPM. The crystal and the readout system are coupled and fixed using a 3D printed enclosure, like the one shown in figure 3.8. These SiPM have a rise time that is twice the PMTs one, but the use of smaller crystals reduces the probability of pile-up. Furthermore, the dimension and the weight of the SiPM detectors are smaller and they can be positioned more easily where it is needed to maximize the solid angle coverage. SiPMs are also known for the temperature dependence of the gain: an ad hoc power supply that corrects temperature related drift in real time was developed and tested during the last FAMU test at RIKEN-RAL [18]. The two rings are connected to an acquisition system based on a set

of CAEN V1730 digitizers cabled to the FAMU DAQ.

High Purity Germanium detector (HPGe)

The $LaBr_3$(Ce) detectors show a satisfactory fast response, fulfilling the requirement of the experiment, but at the expense of the energy resolution. A High Purity Germanium detector (HPGe) with custom fast electronic that can handle the high speed of the FAMU experiment was chosen to produce high quality energy spectrum of the X-rays exiting the target. These spectra are fundamental to double check the consistency of the data collected from the other detectors and to check the purity of the gas mixture inside the target. The readout of this detector is based on a CAEN V1724 digitizer, also in this case connected to the FAMU DAQ.

Hodoscope

To reduce the background noise produced by muons interacting with other target materials, the accelerated beam must be very well characterized and monitored. Elements such as aluminum and nickel produce X-rays with an energy comparable to that of oxygen, which produce a background that must be subtracted during data analysis. The muon beam, as already mentioned, is collimated with a square holed lead absorber, but to verify the uniformity and the position of the beam, a beam profile monitor has been specifically developed through a series of tests carried out during the year of FAMU R&D [19, 20]. This detector is positioned in front of the muons entrance, as shown in figure 3.9. The hodoscope has an active surface of 7.2×7.2 cm^2 which is covered by two layers of perpendicular scintillating fibers, 32 for each layer. The fibers do not cover the entire surface of the opening to minimize the material along the beam path. The light produced by the charged particle crossing the hodoscope is read by a series of 1×1 mm^2 Hamamatsu S12751-050P SiPM with their gain controlled and temperature corrected in real time with a CAEN DT5485 voltage supplies. The coincidences of the signals from the SiPM coupled to the two layers of fibers allow us to reconstruct the shape and the density of the beam.

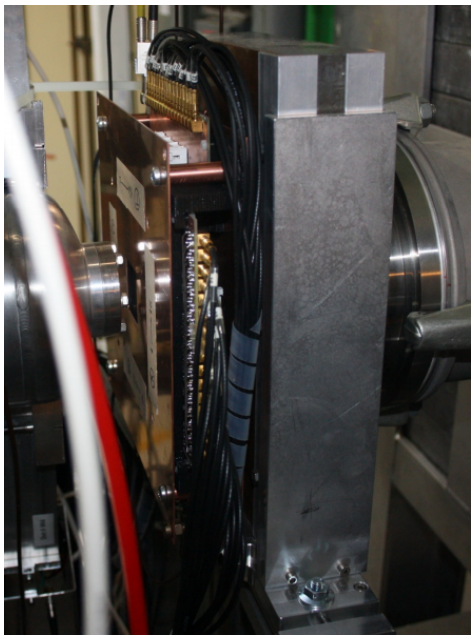

Figure 3.9: The hodoscope placed between the FAMU target and the lead collimator.

3.5 Mid-IR laser

Conventional laser sources emitting in the mid-IR region, such as color center lasers, CO and CO2 gas lasers, diode lasers and quantum cascade lasers cannot met the laser characteristic described in section 2.1.
Sources based on nonlinear frequency down-conversion pumped by solid-state lasers have demonstrated impressive results allowing to reach a wide range of mid-IR wavelengths combined with high energy pulses [21]. Two possibilities of this type of laser were explored: Optical Parametric Oscillation (OPO) and Difference Frequency Generation (DFG).
Systems based on OPO use as input only a high power pump. They can be widely tunable and have demonstrated capabilities of generating energies exceeding 1 mJ in the 6-10 micron range [22, 23]. However, OPOs typically have large bandwidths in the order of several nm, but the single frequency operation require a continuous tunability. This tunability is rather challenging due to the need to preserve resonant cavity conditions. Moreover, in nanosecond mid-IR OPOs optimized for high energy

extraction, the generation threshold is not far from the crystal's damage threshold, which poses reliability problems in cases of long duration measurements with continuous data acquisition. An alternative scheme, the DFG, relies on $\chi(2)$ non-linearity and involves three waves, namely pump, signal and idler. Compared to OPOs, the DFG process has two great advantages. First, it has the possibility to generate narrow bandwidth mid-IR emission by mixing narrow bandwidth pump and signal beams. Secondly, single frequency operation and continuous tuning of the DFG wavelength can be kept with relative ease at a fixed pump wavelength, by tuning the signal wavelength and by rotating a non-linear crystal to the corresponding phase-matching angle.
In the next sections I will describe the laser developed for the FAMU experiment, based on a DFG scheme. After a description of the general setup, I detail the different parts of the system and their automate control.

3.5.1 FAMU laser setup

The FAMU laser system is a pulsed, tunable, narrow linewidth and high energy light source, which aims to deliver the specific radiation parameters listed in table 3.1.

Parameters	Values
Wavelength	6785$\pm$3 nm (44.18 THz)
Energy output	$>$ 1 mJ
Line-width	$<$ 0.07 nm (450 MHz)
Tunability step	0.03 nm
Pulses duration	10 ns
Repetition rate	25 Hz

Table 3.1: FAMU laser requirements.

The FAMU laser source includes 4 different parts:

- the laser system generating the 1.06 μm pump beam;
- the laser system generating the 1.26 μm signal beam;

- the combining and the monitoring of the pump and signal beams;
- the generation, parameterization and monitoring of the 6.78 μm light (DFG).

The block scheme of these four steps is shown in figure 3.10. The laser system is complex, so a new FAMU Laser Control (FLC) software was developed. Written in Labview, constantly monitors the most of all laser parameters.

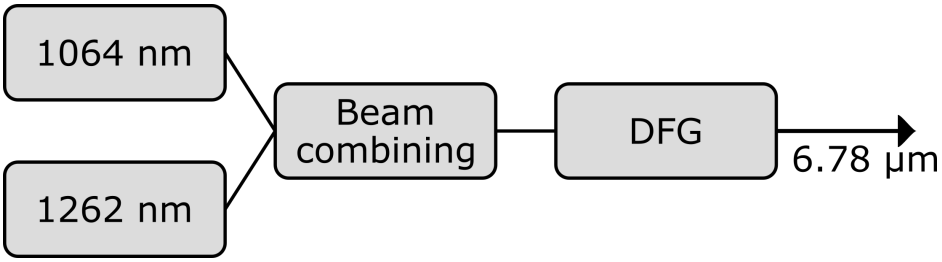

Figure 3.10: FAMU laser block scheme.

3.5.2 1.06 μm Laser Beam

The pump wavelength of the DFG system is a commercially available injection-seeded single-longitudinal mode (SLM) Nd:YAG laser system centered at 1064.135 nm, specially modified by the producer to meet the experiment specific requirements about the pulse duration. This is a master-oscillator power-amplifier (MOPA) Nd:YAG laser system (INNOLAS Spit-Light Hybrid II) seeded with a highly stable continuous-wave fiber laser at 1064.135 nm (Rock Fiber Laser Seeder, NP Photonics), with feedback controlled piezomotor system which enables to keep the single longitudinal mode. The main characteristics of this laser beam are: high energy combined with narrow linewidth, low jitter and single longitudinal mode, as listed in table 3.2.

Parameters	Values
Wavelength	1064.135 nm (or 281.72 THz)
Energy output	$>$ 300 mJ
Line-width	0.35 pm (or 93 MHz)
Tunability step	1 pm
Pulses duration	18-22 ns
Time jitter	$\pm$0.5 ns
Repetition rate	25 Hz
Beam quality	SLM (M^2 x=1.1, y=1.1)

Table 3.2: 1.06 μm laser beam characteristics. Notice that the tunability is not used in this setup, in which the wavelength is fixed at 1064.135 nm. M^2 is the beam quality factor, which describes how Gaussian the beam is.

3.5.3 1.26 μm Laser Beam

The signal wavelength for the DFG process is a laser beam centered at 1.26 μm produced by a dedicated Cr:forsterite MOPA laser system. The main characteristics of this 1.26 μm centered laser beam are: high energy, tunability, very narrow linewidth and single longitudinal mode, as listed in table 3.3.

Parameters	Values
Wavelength	1257–1267 nm
Energy output	$>$ 45 mJ
Line-width	$<$0.5 pm
Tunability step	1.2 pm
Pulses duration	9 ns
Time jitter	$\pm$2.5 ns
Repetition rate	25 Hz
Beam quality	SLM (M^2 x=1.9, y=1.7)

Table 3.3: 1.26 μm laser beam characteristics.

The master-oscillator of this laser system contains a tunable single-frequency Cr:forsterite cavity, pumped by a built-in Nd:YAG laser (LS-2138N,

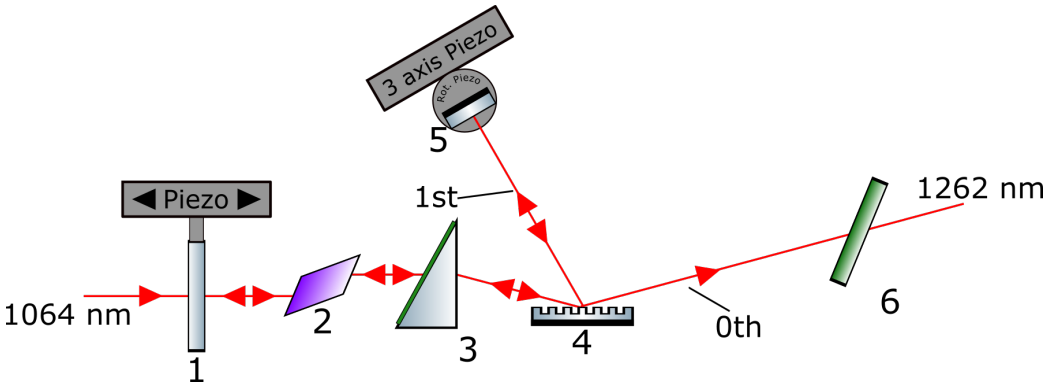

Figure 3.11: Cr:forsterite oscillator block scheme: dichroic mirror (1), Cr:forsterite crystal (2), right-angle prism expanding with entrance side AR coated @1.06 μm(3), diffraction grating (4) and back mirror (5), window with Anti-Reflection (AR) coating @1.06 μm (placed at 56° respect to the beam) (6).

LOTIS TII). The generated light is then injected in a 3-stage, 16-pass power-amplifier, pumped by another Nd:YAG laser (INNOLAS SpitLight 600, $\sim$700 mJ).
The oscillator, described in figure 3.11, uses a built-in 1.06 μm Nd:YAG laser coupled in a cavity formed by a dichroic mirror (anti-reflection (AR) @1.06 μm and HR@1.26 μm) (1), a 6.5$\times$9$\times$16 mm^3 Cr:forsterite crystal (2), a beam expanding right-angle prism (AR@1.06 μm to protect the diffraction grating)(3), a diffraction grating (1350 grooves/mm) (4) and a back mirror (HR 1257-1267 nm)(5). The dispersed beam coming out from the prism is selected with high precision in the 1^{st} order diffraction of the grating forming a grazing incidence cavity, with the 0^{th} order diffraction forming the output, sent to the amplifier. The back mirror (5) is placed on a rotation piezomotor, thus allowing the selection of the required wavelength by changing its angle with respect to the 1^{st} order diffraction. The whole assembly is fixed on a kinematic mirror mount with piezoelectric adjusters that allows remote vertical aligning of the Cr:forsterite cavity.

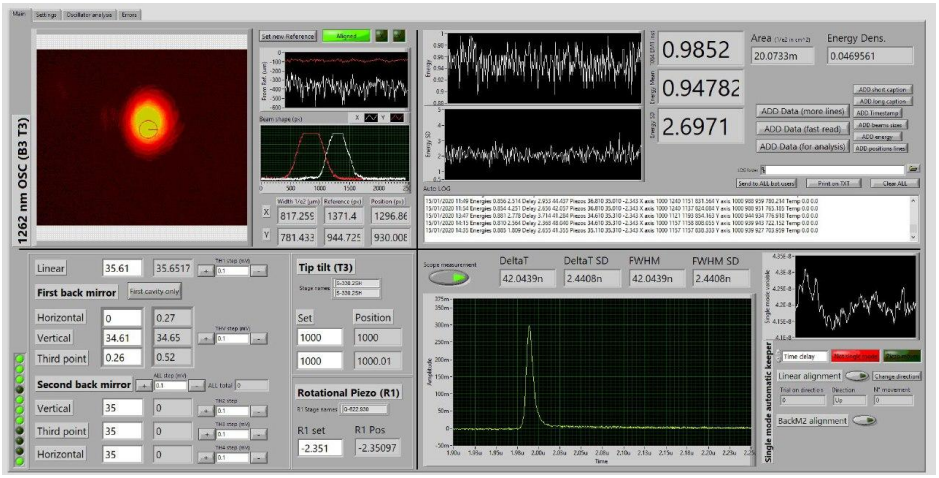

Figure 3.12: 1.26 μm oscillator control interface. The window is divided in 4 pads with different applications, clockwise from the top-left: monitoring the positioning and beam shape, energy and stability control, pulse shape and jitter measurement, and control of the piezomotors.

The first part of the FLC software (the graphic interface is shown in figure 3.12) constantly monitors the oscillator beam parameters through a series of sensors. This software is able to prevent the instability of the Cr:forsterite oscillator's cavity and the loss of the single mode operation of the laser emission due to thermal effects. The program acquires information about:

- energy (EnergyMax-USB J-50MB-LE,Coherent Inc.);
- wavelength and the linewidth (WS7-60 IR-I, High Finesse);
- timing and the beam pulse temporal shape, using a PIN-photodiode (InGaAs ET-3010, Electro-Optics Technology, Inc.), connected to an oscilloscope (MDO4104C, Tektronix);
- beam size and position through a self-made software, which use as reference the centroid of the beam. The detection is made by a CMOS camera (acA2440-20gc, Bassler AG) which images a secondary deviated beam.

All these measurements are gathered 5 times per second. The system is able to react in real time to keep the parameters in a predefined range centered on the requested values, in particular (numbers refer to figure 3.11):

- the single mode operation is maintained by acting on the piezomotors of the dichroic input mirror (1) and on the vertical adjuster of the back mirror (5);

- the position of the Cr:forsterite oscillator beam is controlled by moving a piezomotorized mirror at the output of the oscillator.

Both actions can be performed remotely by a user or automatically by the FLC program taking as reference predefined parameters. With a pump energy of 36 mJ, the oscillator generates approximately 1 mJ in the spectral range 1257-1267 nm. The beam energy slightly depends on the exact wavelength selected with the back mirror and this energy variation can be measured through the Cr:forsterite amplifier and the DFG setup as a whole. Before entering the amplifier, the oscillator's beam is frequency doubled by a second harmonic generation (SHG) crystal (BiBO), to generate the 631 nm beam that is observed with the CMOS beam positioning camera. The 1.26 μm beam is reflected with one of the HR@1.26 μm mirror to the amplifier, while the SHG beam passes through the mirror, which is transparent for the 631 nm visible light, up to the camera. This scheme was chosen to minimize the light losses of the beam, even taking into consideration the up-conversion losses, as the sensitivity of the camera in the visual range is much higher compared to the sensitivity in the IR range. Figure 3.13 shows the optical scheme of the beam path between the MOPA and the amplifier.

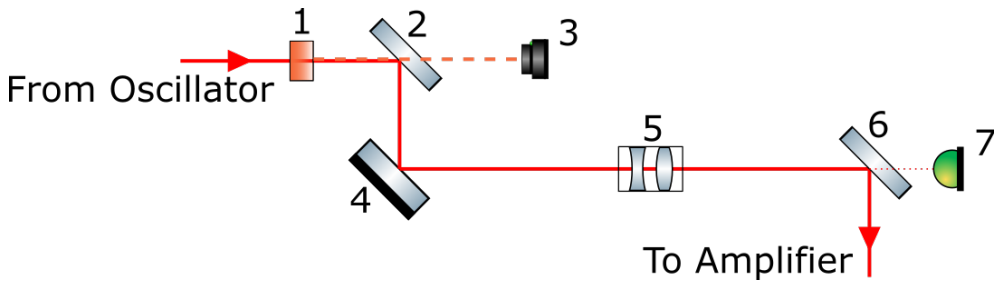

Figure 3.13: Scheme of the beam path between the oscillator and the amplifier: SGH BiBO crystal (1), HR@1.26 μm mirror (2), visible CMOS camera (3), HR@1.26 μm mirror (4) telescope (5), 1.26 μm mirror (6), PIN-photodiode (7).

The 1.26 μm light produced by the oscillator is injected in the amplifier unit pumped by another Nd:YAG laser (INNOLAS SpitLight 600), in order to increase the final energy by a factor of 50 and more. Figure 3.14 shows the amplification system.
The oscillator's beam is monitored for its position before entering the amplifier and it is resized using a telescope to best fit the amplifier crystals; its pulse shape and timing delay from the external trigger are registered and measured by a PIN-photodiode connected to the oscilloscope, (7) in figure 3.13.
The Cr:forsterite amplifier is composed of three stages, each one with a Cr:forsterite crystal, cut at Brewster angle, with a total of 16 passes through them. The three crystals have different dimensions and are pumped with different energies from a laser beam at 1.06 μm, delivering a total of 450 mJ of horizontally polarized light, which is split in three beams using a set of waveplates and polarizers. The energies injected in the crystals are 112 mJ in the first, 156 mJ in the second and 160 mJ in the third one. The values are chosen in order to fit best the sizes of the amplified beams and keep the energies of the three 1.06 μm pump beams close to the optimal excitation energy density of 1 J/cm^2. The total number of passes is 16 because the last crystal is depleted from the stored pump energy in only four passes by the 1.26 μm laser beam coming from the second stage [24].

A total output energy of 45 mJ is generated starting from a 0.85 mJ oscillator beam thus giving a multiplication factor of 53. A further increase of the Cr:forsterite unit can be obtained by increasing the pump energy at the third stage and adding two additional passes.

3.5.4 Combining the two beams

The two beams at 1064 nm and 1262 nm, exiting the lasers are resized through dedicated telescopes to fit the non-linear crystal's dimensions. As shown in the scheme given in figure 3.15, the beams are then guided through a system of mirrors and combined by a dichroic mirror DM1 (S1: Ts>97% @1.06 μm and Rp>99.3% @1.26 μm; S2: AR@1.06 μm, AOI=45°) to overlap collinearly after it. Mirrors M2 and M5 are mounted on piezo driven tip/tilts (S-330.2SH, High-Dynamics Piezo Tip/Tilt Platform – PI-Physik Instrumente) that allow remote and automatic re-aligning of the

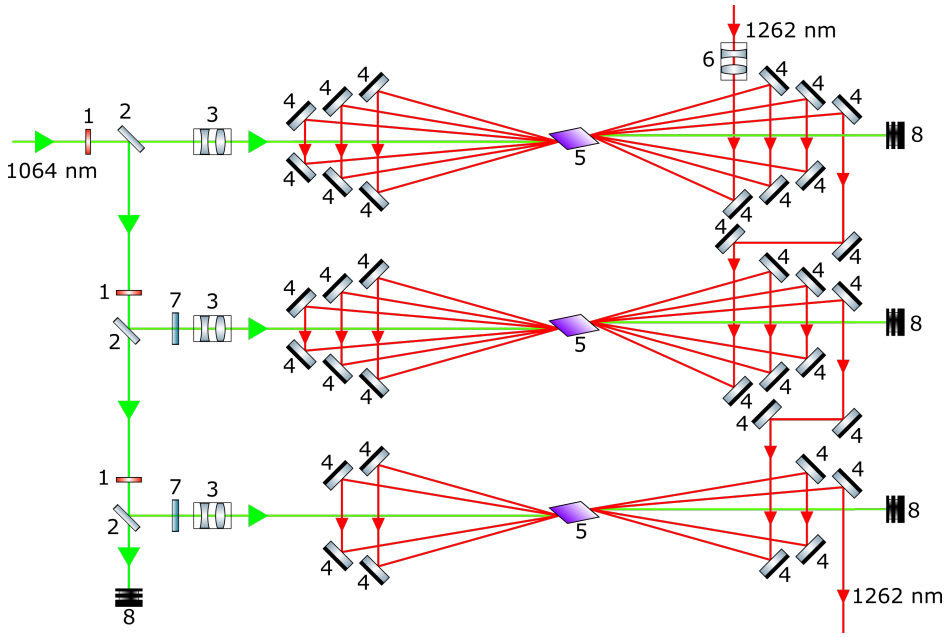

Figure 3.14: 1.26 μm amplifier block: $\lambda/2$ waveplate at 1.06 μm (1), polarizer at 1.06 μm (2), telescope AR coated at 1.06 μm (3), mirror HR 1.26 μm (4), Cr:forsterite crystal (5), telescope AR 1.26 μm(6), polarization rotator 90° at 1.06 μm (7) and beam dump (8).

beams in order to keep the overlapping constant. Beam samplers (not shown in figure 3.15) direct part of each beam to a system of sensors (energy sensor, NIR camera, PIN-photodiode and wavelength meter) used by the FLC program to perform a complete check of both lasers' parameters. The observed characteristics of the two beams are:

- pulse lengths, shapes and timings, to have the perfect synchronization for the phase matching;
- the energies, to avoid too high energy that can damage the non-linear crystal, especially for the 1.06 μm radiation;
- the positions, with automatic re-alignment;
- the transverse dimensions and the shape of each beam, to ensure they fully overlap on the non-linear crystal (an example can be seen in figure 3.17);

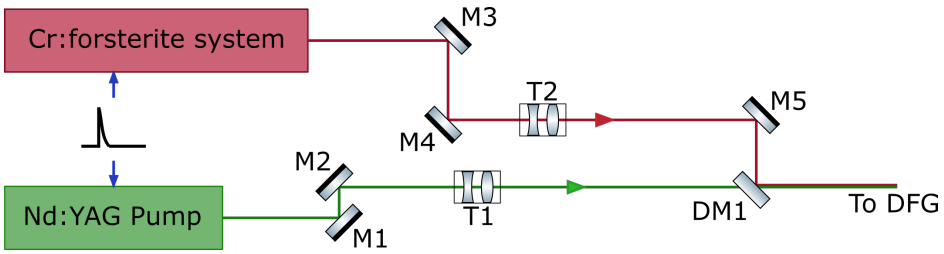

Figure 3.15: Diagram of the beam combing block: 1.06 μm mirrors (M1-M2), 1.26 μm mirrors (M3-M4-M5), 1.06 μm telescope (T1), 1.26 μm telescope (T2), dichroic mirror (DM1).

- the wavelengths and linewidths of the pump lasers, to ensure that the right wavelengths are mixed for the DFG process.

Figure 3.16 shows one of the control panels of the FLC program and in particular the one which displays the data of the two beams before entering the DFG setup.

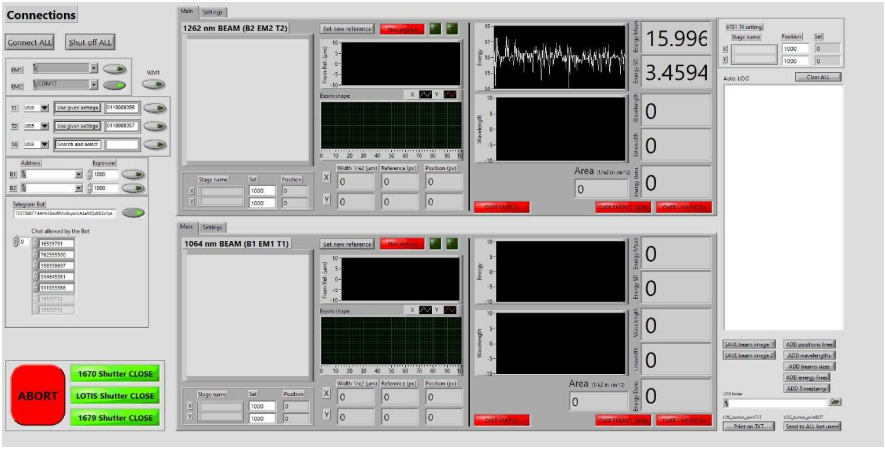

Figure 3.16: Beams' control interface. The left and right panel are for the setting. The center is divided in two rows and two columns. Each row shows the parameters of one of the two beams, on the left column the beams position and shape and on the right columns the energy and the wavelength.

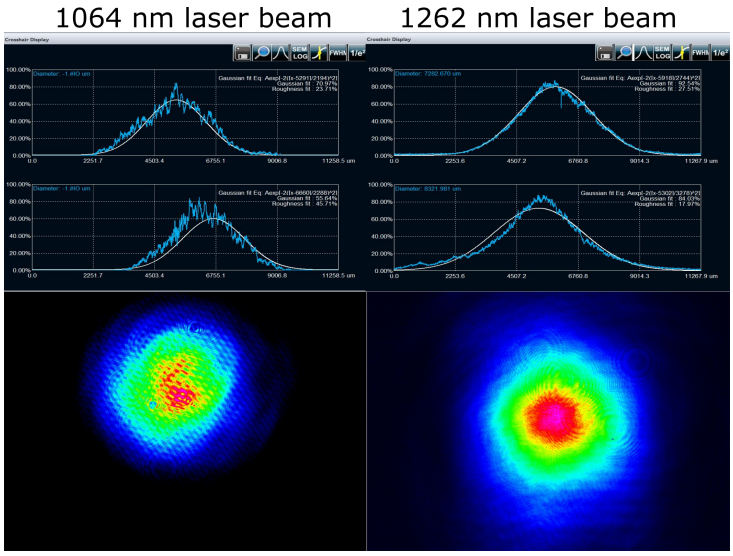

Figure 3.17: Images and cross-sections of both beams along X and Y axis showing a Gaussian shape profile. The beam profile of the 1.06 μm radiation presents interfering patterns because of the use of a set of neutral filters to decrease its intensity.

3.5.5 DFG scheme

The Nd:YAG wavelength is fixed at 1064.135 nm while the Cr:forsterite is tuned at 1262.075 nm, thus generating 6785 nm[25]:

$$281.72 \text{ THz} - 237.54 \text{ THz} = 44.18 \text{ THz}(6785 \text{ nm}).$$

A non-linear (NL) crystal is fixed on a 6 axis kinematic mount for easy aligning and setting at the correct phase-matching angle. The two laser beam at 1.06 μm and 1.26 μm, correctly polarized and time synchronized, are injected inside the NL crystal using a double pass configuration, as shown in figure 3.18. In this setup the pump and signal beams are reflected in the crystal with a trichroic mirror, which reflects the two beams but transmits the 6.8 μm beam produced in the DFG process. All the three beams exiting the crystal are then reflected back with a silver broadband mirror to the trichroic, where only the 6.8 μm beam passes through the mirror in the direction of the target.

The 6.8 μm laser beam is monitored to control the parameters of the light to be injected into the cryogenic target for the hyperfine splitting ex-

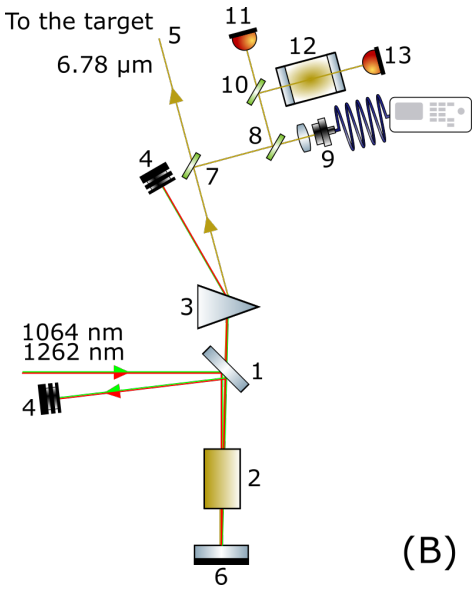

Figure 3.18: Diagram of DFG setup double pass configurations with absolute calibration setup. The component are the following: trichroic mirror (1), non-linear crystal (2), prism (3), beam dump (4), 6.8 μm light (5), silver mirror (6), beam splitter (7,8,10), optic fiber coupled with the wavelength meter (9), energy meter (11,13), calibration cell filled with ethylene gas (12).

periment. The monitoring system collects continuously information on the energy, the wavelength and the linewidth, three fundamental parameters for the FAMU experiment. These data about the energy are collected using a EnergyMax-USB J-10MB-LE Energy Sensor, which is optimized for low energy measurement as uses the diverted 5% of the initial beam, and the wavelength and linewidth data are collected using a HighFinesse Wavelength Meter WS6-200 IR III, from a beam diverted with the reflection on a ZnSe window. The data collected are saved on the PC and then saved together with the data collected from all detectors of the experiment.
One of the key point in the FAMU experiment is the precision of the laser wavelength. To ensure an accurate measurement of that value, an absolute calibration procedure was developed. This technique is based on the absorption lines of gaseous ethylene (C_2H_4). A cell filled with C_2H_4 is placed on the path of the 6.78 μm beam. The absorption is then mea-

sured comparing the energies before and after the cell. Varying the laser wavelength, an absorption spectrum is obtained and it is compared to the HITRAN database [26] for an absolute calibration.

The entire laser system is closed in a safety cover, made by plastic removable panels, that acts as safety device against stray beams. The safety cover increases also the thermal stability of the laser and therefore the precision of the generated light, isolating the temperature sensible laser system from the external temperature variation. Part of this cover is also designed to be air tight. In fact, to avoid the absorption of the IR light in air caused by atmospheric water vapor, the DFG setup cover is filled with dry nitrogen.

3.5.6 Target injection

The generated mid-IR beam at 6.78 μm, after being characterized, is sent to the FAMU target which contains the muonic hydrogen at 7 bar, 80 K. A multi-pass cavity is placed inside the gas target to "trap" the laser beam and maximize the number of excited atoms before it is absorbed by the gas and the mirrors. To maximize the reflections inside the cavity a high precision alignment of the beam is required at the first mirror of the cavity. For this reason, the FLC program executes also a real time alignment of the beam passing through the target windows. This is done through a series of IR sensors developed for the FAMU experiment and positioned in the last part of the laser path, before the target entrance. These monitoring detectors consist in 4 IR pyroelectric active surfaces placed at 0-90-180-270 degrees in a plane perpendicular to the beam. They are able to report in real time to the system if the beam is misaligned and in which direction [27]. With these information the system automatically moves the last guiding mirror before the target entrance, placed on a tip/tilt piezomotor, thus keeping the IR beam in the correct position.

3.6 Data acquisition system

All the parts described above are required by the experiment, but a reliable acquisition system is essential to store the data collected by the detectors and sensors that are placed around the setup. The first step to be able to

acquire data is the synchronization of all these devices, which becomes particularly challenging when the devices cannot work at the same rate. The muon bunches arriving from the accelerator, as described before, have a rate of 50 Hz but arrive in train of 4 bunches followed by a missing one. Instead, the laser is designed to work at 25 Hz forcing us to synchronize the two events also remembering that the fifth is missing. To overcome this, we need to be able to synchronize the laser shot with the second and the forth bunches of the train, leaving the first and the third without laser and to be used as reference of an event without laser. For this reason the experiment needs two different triggers: the detector trigger, which makes use of the accelerator triggers, and a more complicated laser trigger. The two

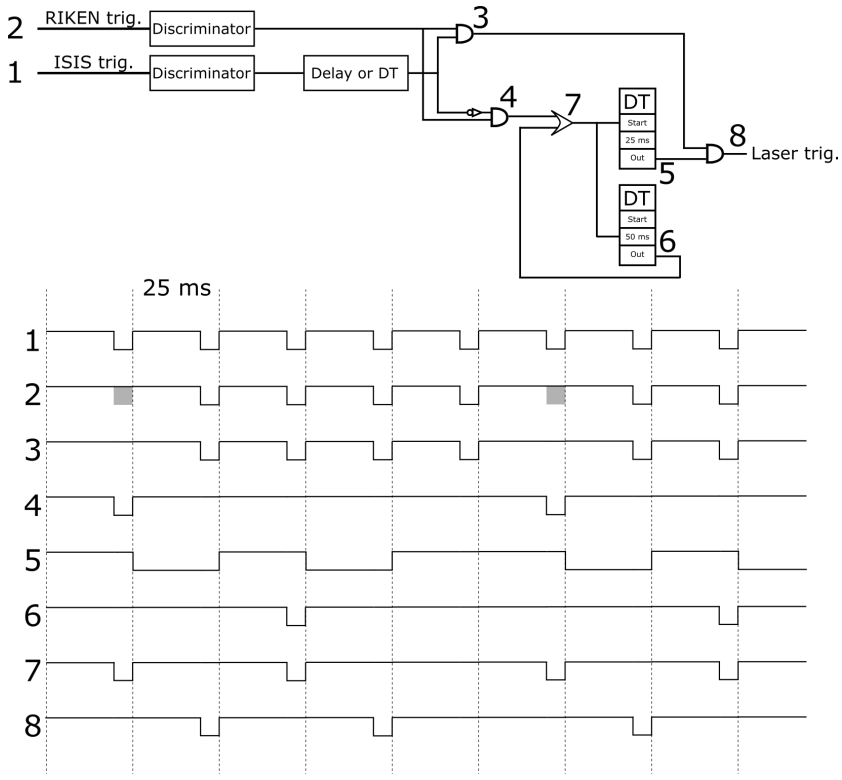

Figure 3.19: On the upper part the scheme with the electronic NIM module to produce the needed laser trigger. On the bottom side the scheme of how the signal are synchronized.

triggers given by ISIS will be exploited in a setup as shown in figure 3.19.

One of the trigger arrives directly from the accelerator, giving a perfect 50 Hz signal (1) meanwhile the other comes from a detector on the beamline before Port 1, giving a signal only when the muons are arriving to the target (2). The signal produced using the anti-coincidence (4), so the events (1) and not (2), after been delayed (5), are used to trigger the event after, in which surely there will be muons. The trigger produced with the electronic scheme on the picture (8) is used to trigger the laser and a clone of this signal is also sent to a custom trigger board FPGA based, which is able to handle both trigger signals, the detector trigger and laser trigger. This board uses the detector trigger signal to synchronize the acquisition of the digitizer electronics, meanwhile the laser trigger is used to give a signal to the "Laser collector PC" which is described after in this section. The trigger board also creates the trigger event number which is fundamental to the data acquisition.

The FAMU acquisition system is a complex set of devices, formed by 3 branches:

- a system to digitize the data from the X-ray detectors;
- an apparatus with a series of instruments to gather the laser characteristics shot-to-shot;
- a setup to acquire the housekeeping information from the target.

All these branches are connected to a set of PCs able to collect, merge and store these data, and to do a fast real time analysis to check the status of the experiment. To better clarify the setup I will name "X-ray collector PC", "Laser collector PC" and "housekeeping collector PC", the computers which are directly connected to the devices that acquire the data. In addition to these three, other two computers, one which collects all the data from the other branches and merge them, storing the final results in two copies (one in a local disk and one on the INFN network) and a second one which perform the online fast real time analysis to check the status of the running experiment are used. All this acquisition system is described by the following drawing in figure 3.20.

The setup for acquiring housekeeping data is easier to describe and, although not essential for calculating the transfer rate, this system allows us to track and monitor the complete situation of the experiment, also allowing us to evaluate *a posteriori* the state of the target during the acquisition

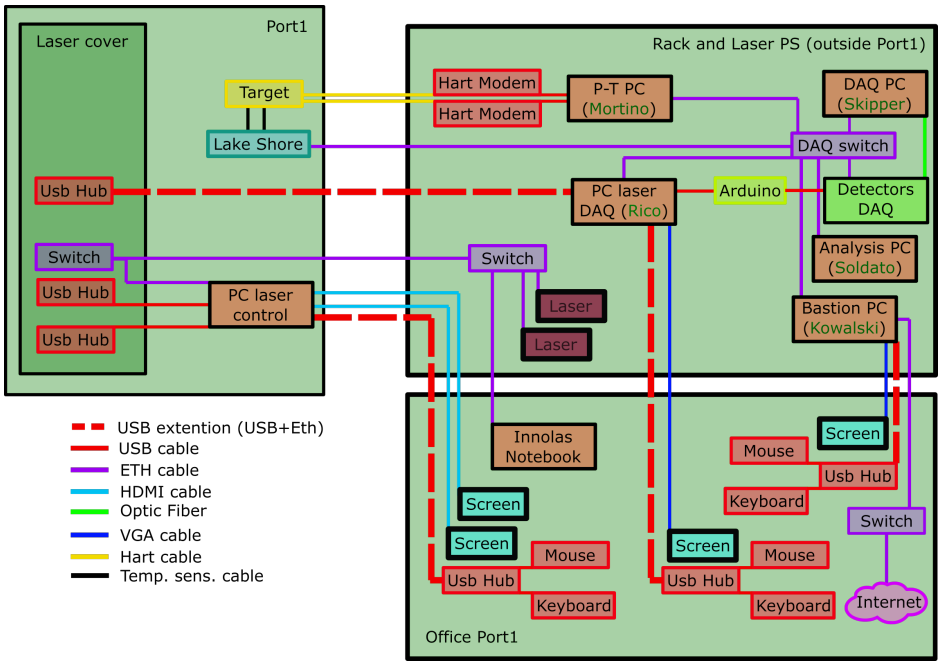

Figure 3.20: This scheme shows the system used to collect data from the FAMU experiment.

of a particular signal. The setup consists of a series of sensors fixed on the target to monitor the pressure and temperature of the internal vessel, the vacuum level of the cryostat and the level of liquid nitrogen present inside the reservoir. All these sensors are connected to the housekeeping collector PC, in which a specific developed program gathers all the values and send them to another PC that will collect all the data coming from all the DAQ setup branches.

The main system is the one which collects the physical data related to the time and amplitude of the X-rays produced inside the target and collected by the set of detectors described before. The X-rays collector PC, running the Linux-based FAMU DAQ software, is equipped with a CAEN V3818 PCIe-Optical Link bridge, allowing the computer to be connected directly using an optic fiber to the CAEN V2718 VME bridge. This board gives access at the PC to the VME bus on the back of the crate where all the digitizers are connected. The experiment uses three types of digitizers to convert the amplified or pre-amplified analog signals coming from

the different detectors. All the $LaBr_3$ detectors signals, both the one read with PMT and SiPM, are digitized by a set of CAEN V1730 8-channels 14 bit 500 MS/s Digitizer, used to sample with a 2 ns step the pulses coming in the 12 μs after the trigger. In this time frame the arrival of the muons double spills and the complete delayed phase after them can be observed. As mentioned before in the detector section, a new acquisition system is under development for the $LaBr_3$ detectors read by PMT, which will be independent from the V1730 and it will perform the digitization directly in the detector front-end. The hodoscope is connected to a set of CAEN V1742 32+32 Channel 12bit 5 GS/s Switched Capacitor Digitizer, capable to handle the great amount of channels coming out from this detector. Finally, the HPGe, after a required pulse shaping done with an Ortec 579 Fast Filter Amplifier, is connected to a CAEN V1724 8 Channel 14 bit 100 MS/s Digitizer. As said before, this VME crate is connected to the X-rays collector PC where the first part of the FAMU DAQ software is running. This computer only collects the data of the detectors and store them in a reliable standard HBOOK files. The software is based on a C program with a graphical interface written in TCL.
The system described so far does not take into consideration the laser data acquisition. As previously mentioned in the laser section, the laser setup is controlled by two FLC programs, which are installed in the same computer and control almost all the parameters of the laser, from the pointing to the energy and wavelength of the beams which are combined to produce the 6.8 μm light. These software are huge and controlling all these important parameters in real time, shot to shot, would slow down the PC and make less reliable and stable the full system. For these reasons FLC run at around 10 Hz for every sensors, except for the camera's images of the beam which are in full resolution and in long exposure, forcing the program to work at lower rates. In order to increase the reliability of the DAQ system, I decided that the program which acquires information from the laser final beam before entering in the target must run on a different computer with respect to FLC. This program collects information about the energy, the wavelength and if the laser fired or not during the last experiment trigger, shot to shot. These data are fundamental for the experiment and they are necessary for the data analysis. Usually this kind of task is performed by a central DAQ program, in this case the X-ray collector PC. The main issue at this point is the operating system of the laser DAQ. The X-ray collector PC is based on a Linux environment, but the drivers needed to connect the Laser col-

lector PC to wavelength meter are provided by the manufacturer only for Microsoft Windows. This forces the choice of the Windows operating system and obliges us to use a different computer to acquire the important data from the laser and then transmit to the merger PC, rising a further issue. It's important to be able to match the data of single laser shot to the respective muon bunch and to do this a trigger number must be share between the two DAQ programs. The custom trigger board solves this issue by sharing the trigger number on both X-ray collector PC and laser collector PC. As mentioned above, when an accelerator trigger arrives to the board, its FPGA creates the event number and sends it via the VME bus to the CAEN V2718 and finally to the X-ray collector PC.

The trigger board is equipped with a freely programmable 16 pin digital I/O. In this case the trigger board is programmed to share the coded number via the I/O port directly to the Arduino Due coded to convert the binary number in decimal and immediately send it to the laser collector PC via serial protocol. The number is sent only when it changes, giving the possibility to use the serial message as a trigger for the laser collector PC, which will then collect the data from the wavelength meter and the energy meter. These two devices are activated by the laser trigger and store the last reading until requested by the PC. This computer saves the trigger timestamp, the event number, the wavelength and the energy of the laser pulse and the other housekeeping data to check the stability of the system. All these values are stored locally and they are directly collected by the merger PC, which has access to the disk of the Windows PC.

Once all these data are "synchronized" using the timestamp and the number of trigger, they are merged in the same ROOT files, ready to be analyzed by the analysis program in real time and to be sent for final storage in the INFN network.

Chapter 4

Developments

The setup of FAMU experiment has required a long developmental process, which I joined during my PhD, contributing actively to the final design of the overall apparatus. In particular, this setup consists of a main body, formed by the TS and the detectors assembly, and the laser setup which lies on an optical table.

4.1 Layout development

When designing the layout, the first fundamental parameter to be taken in consideration is the height at which the muon beam is delivered in our experimental room, that is centered at 1.9 meter from the floor, determining the height of the TS. For the muon transfer rate preliminary measurement, a big aluminium structure was developed to sustain the TS, but this did not consider the laser which was not necessary during those tests. Introducing the laser into the setup meant to find a location to place the complete huge laser apparatus with the best solution to inject the light into the FAMU target. The initial idea was to divide the laser setup in two parts: a first one including all the devices needed to produce the two laser beams that must be injected into the non-linear crystal, and a second one with the DFG setup directly connected to the TS. This solution resulted to be not convenient due to the possible vibrations between the two setups and the complicated safety system which was needed between the two parts. In fact, the laser beams must be confined inside an aluminium or steel tube to avoid possible stray beams that can cause injuries to the operators.

In addition, any misalignment between the two setups can lead to fluctuations in the final laser energy, introducing other variables in the final data acquisition. For this two reasons, it was decided to simplify the setup by distributing the whole experiment on one optical table, thus improving the stability and the safety of the system. An optical table 4 m long and 1.5 m wide was purchased, then positioned parallel to the wall of the muon beam pipe. The table, 0.9 m high, hosted the entire laser setup on the surface and was covered by plastic panels for safety reasons. The cover was designed to leave a 5 cm free frame around the edge of the table, where an aluminium structure was fixed to hold the TS in place. This solution, shown in figure 4.1, allowed to avoid the vibrations not only between the laser stages, but also between the laser and the target, in which, as I said, there is the optical cavity, highly sensible to misalignments.

The position of the table was carefully chosen to house the lasers power supplies and the detector electronics outside Port 1. As mentioned in chapter 3.5, the laser is very sensitive to temperature variations and thus a powerful air conditioning system was mounted. To further minimize temperature issue, most of the electronics was placed outside the experimental room, even through this gave origin to another issue: the length of pipes and cables. In fact, the pipes that connect the lasers to their power supplies cannot be disconnected and replaced and this was solved by rearranging the position of the laser heads on the table and re-positioning the table nearer to the wall. A similar constrain was also found with the detectors electronics, which work better with shorter cables in order to avoid possible electronics noises and reduction of the signal strength.

4.2 Test on advanced detector based on Ce:$LaBr_3$ read by SiPM

During my PhD, I had the opportunity to analyze fresh data collected during a data acquisition period at RAL in December 2018, to which I participated. These data were needed to evaluate the quality of the measurements performed using the $LaBr_3$ detectors read with the SiPM, as the one described in section 3.4. These devices were the latest added to the detectors of FAMU, and were equipped with an automatic system able to keep the detector gain constant. SiPM are known to be very sensible to temperature

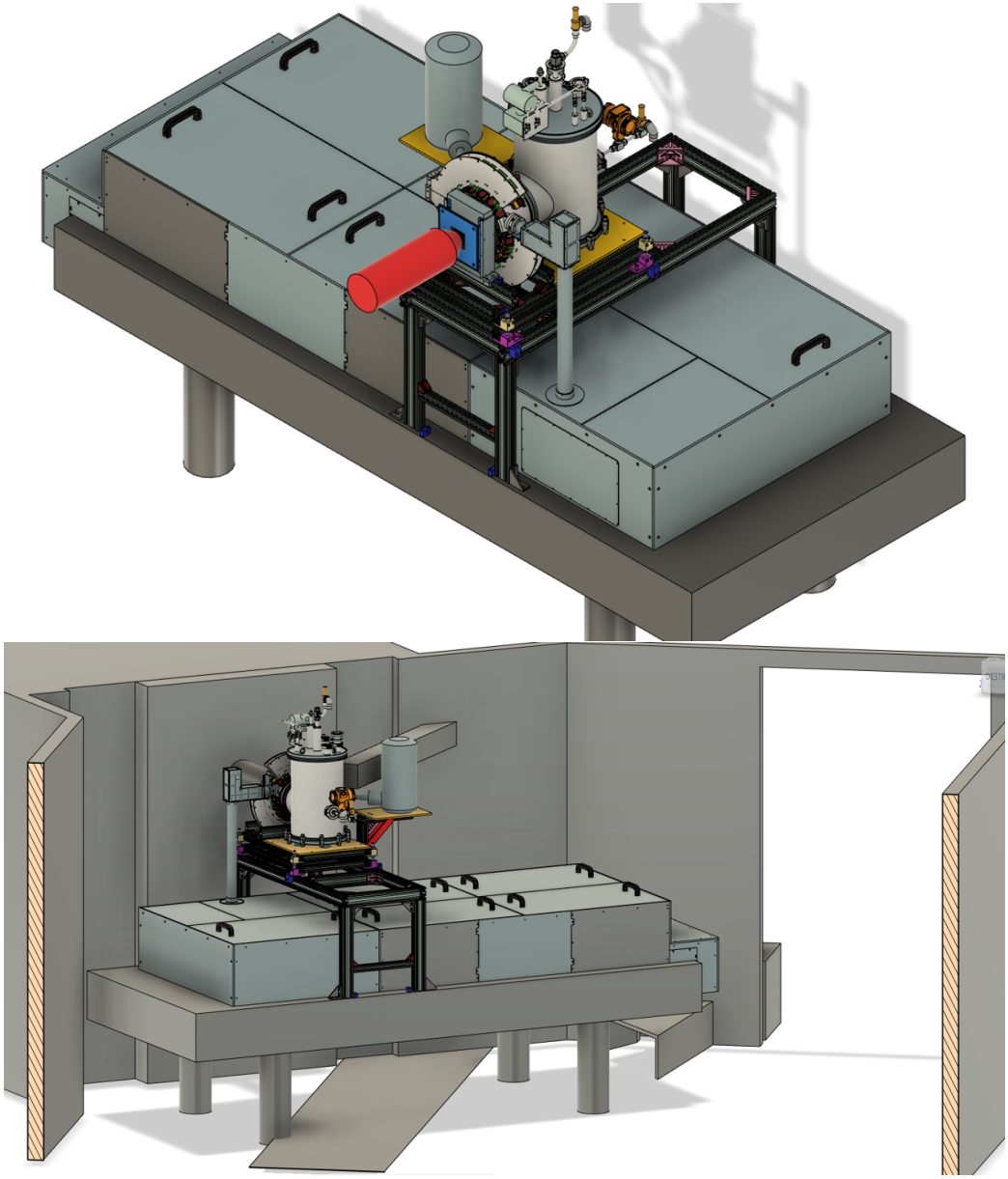

Figure 4.1: The two CAD drawings present the final setup chosen for the FAMU experiment (top) and the position of the table inside the Port 1 (bottom). The optical table hosts both the laser, inside the safety covers, and the target system.

variations and for this reason a specifically developed electronic gear able to change the voltages applied to the detectors according to the temperature was added. Before the data acquisition in December 2018 these electronic devices were not fully tested in long data taking, therefore the FAMU data acquisition to measure the transfer rate with different temperatures, pressures and gas concentrations was a perfect test opportunity.

The data I analyzed were collected using the second FAMU target as described in section 2.2, which gave the possibility to select the pressure and a precise temperature for the gas. The data analyzed and reported in the following section were taken from three different day times. All measurements were based on a hydrogen-oxygen mixture, but collected in different hours of the day, I used two sets that had 0.3% concentration of oxygen at 40 bar and one which had a 2% concentration at 7 bar. All three sets were taken at 80 K. In total, I analyzed 3.5 million trigger events, with an avarage of 80 minutes or 1.2 million events per set. The analysis was mainly focused on studying the gain of the detector over time. Since it was the first time that data of these detectors were analyzed, I started from an in depth analysis of the pulses produced by the SiPM, to better decide the algorithm to measure the height of the signals. All 8 detectors of this analysis are based on the same Ce:$LaBr_3$ scintillation crystals, provided by Kinheng, with an active volume of 14x14x14 cm^3, but used SiPM based on the same Hamamatsu S13361 TSV with different detector windows. Different types of silicon and resin windows were tested. A detector formed by Ce:$LaBr_3$ crystals with Hamamatsu S13361-3050-AS SiPM arrays showed to have a resolution at 622 keV of 3.1% and at 122 keV of 6.6%, which are the target of the FAMU experiment [18]. The SiPM showed a 54 mV/°C gain drift due to temperature variation, typical of this type of detector. For this reason, a system was developed to keep the gain stable by varying the voltages applied to the SiPM according to the temperature variation, using a CAEN A7885D regulated power supply chips.

The analyzed signal pulses showed a peculiar behavior. An example of this can be seen in the following figure 4.2. The second and the third figures show a zoomed portion of the first one, which represents an example of a signal pulse from the detector. The pulse shows a good rise time of the order of 45 ns, but after the peak the signal is not always able to recover to the same baseline level as before the peak. Most often the peak had a long wavy right tail with, in some cases, a strong overshoot after the peak. Estimating the baseline after the first peak was unfeasible and unfortunately

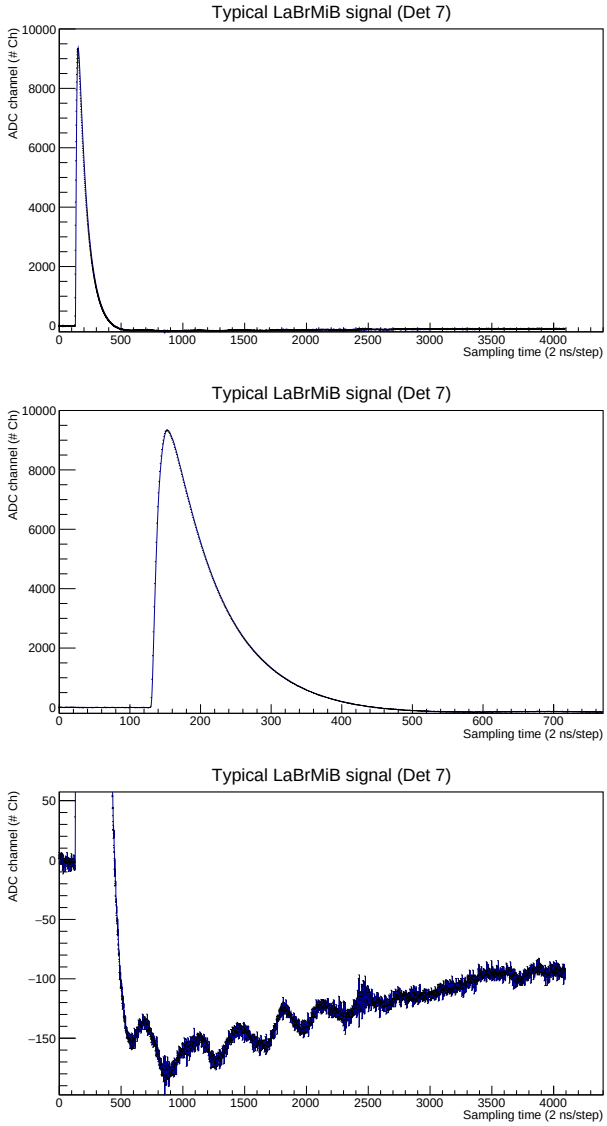

Figure 4.2: These plots represent an example of a signal pulse coming from the $LaBr_3$ detector equipped with the SiPM array readout. The second and the third are a zoomed part of the first plot and they are showing the good rise time of the signal and the wavy undershoot after the peak.

the pulse had a complex shape difficult to be fitted. For this reason the analysis was based only on the first pulse for each trigger, cutting one third of the total statistics.

Starting from what was discovered from these pulses, I decided to measure the height of the peaks measuring the amplitude variation between the mean of the baseline before the peak and the maximum of the peak. To determine the maximum and the initial peak variation I used two different methods, based on the pattern recognition on the derivative curve of the signal. For the maximum I simply look for the derivative sign inversion taking into account the possibility of some fluctuation around the peak. In case of an unclear situation I selected the higher amplitude point. To find the point where the signal starts to rise I set three threshold for three consecutive point that must be fulfilled at the same time. These thresholds were selected and carefully tuned to better match the signal of the single detector.

Using this procedure I was able to plot the energy spectra like those recorded with other detectors and a standard PMT readout. The spectra show the same expected peaks in a transition rate measurement with the FAMU test setup with prompt and delayed phase, as can be seen in figure 4.3, and a resolution slightly higher than the one measured in the laboratory test before the data taking. This small variation in the resolution, of the order of 3% in the 122 keV region, was not constant throughout all the analyzed set. A more in depth analysis was performed, showing that all detectors suffered the same effect, but in a different way depending on the time of the measurement. It was discovered that this unknown behavior was an effect of the temperature variation inside the experimental room Port 1. In fact, as it can be seen on the following picture 4.4, the gain and therefore the peak position in the spectra drifted in time in opposite directions during the day and night. This helped to identify a firmware issue in the electronic circuit, which should have kept the gain constant as the temperature changed and, instead, it was not working. The bug has been fixed and the $LaBr_3$ detector equipped with the SiPM array readout proved to be an optimal addition to the detector system of the FAMU experiment.

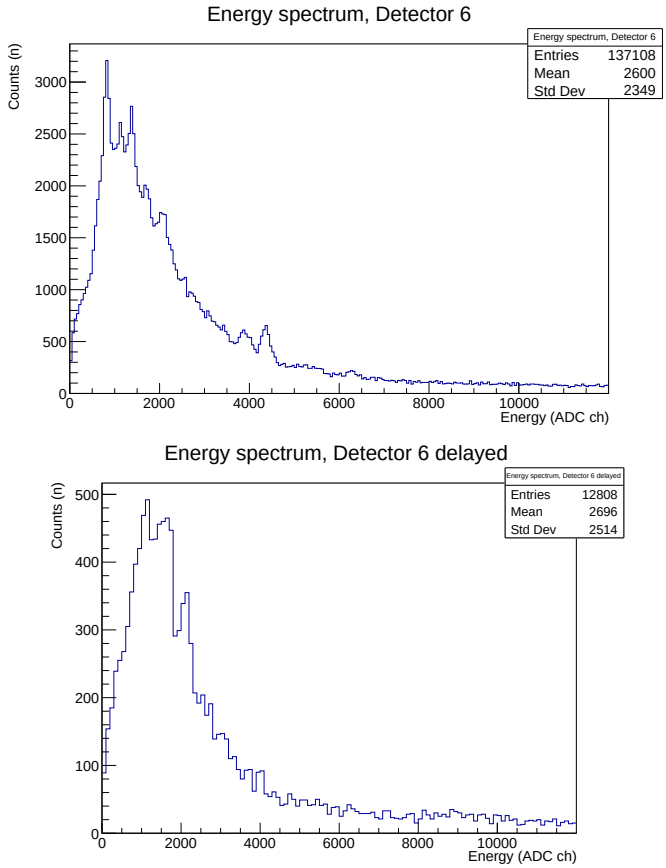

Figure 4.3: The two graphs show the energy spectra collected using the $LaBr_3$ detector equipped with the SiPM array readout. The first one shows the prompt phase of the experiment, where the Aluminium, Nickel and Carbon lines are visible. In the second one the oxygen lines produced during the delayed phase are visible.

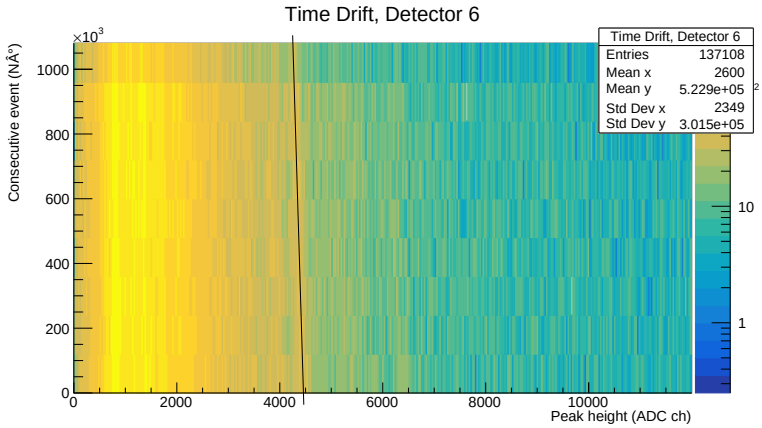

Figure 4.4: The 2D energy spectrum shows the gain variation of one of the $LaBr_3$ detectors equipped with the SiPM array readout. This variation can be seen looking to the Nickel peak which is underlined by a black line. In a perfect situation with a constant gain, it should be perfectly vertical line, while in this plot it has a clear slope.

4.3 Laser development

The development of the FAMU laser has been one of the main topics of my three years of PhD, even if its development is an ongoing process since 10 years. The following sections will describe the part of the development in which I have been directly involved.

4.3.1 Oscillator improvement and characterization

One of the main peculiar features of the FAMU laser system is given by the Cr:forsterite MOPA, which delivers one of the two initial beams that are then injected in the non-linear crystal of the DFG setup. The Cr:forsterite MOPA, hereinafter referred to the Oscillator, as described in the section 3.5.3, is formed by a Nd:YAG laser (LS-2138N, LOTIS TII) which pumps a Cr:forsterite cavity that can be modified to obtain a tunable, single-frequency and narrow linewidth laser beam. The cavity, as built by the manufacturing company, had a linear piezomotor to help the alignment of the cavity, but some of the work must be done by opening the laser and directly adjusting the knobs of the mirrors kinematic holders. In addition, the

optical mount for the wavelength tuning was totally manual, not allowing a frequent external modification of the final wavelength of the beam. Also a complete realignment of the optical cavity was necessary in the event of larger wavelength variation. To overcome all these issues, a set of remotely controlled piezomotors were positioned in correspondence with the most important mirrors of the cavity. Figure 4.5 shows that the linear piezomo-

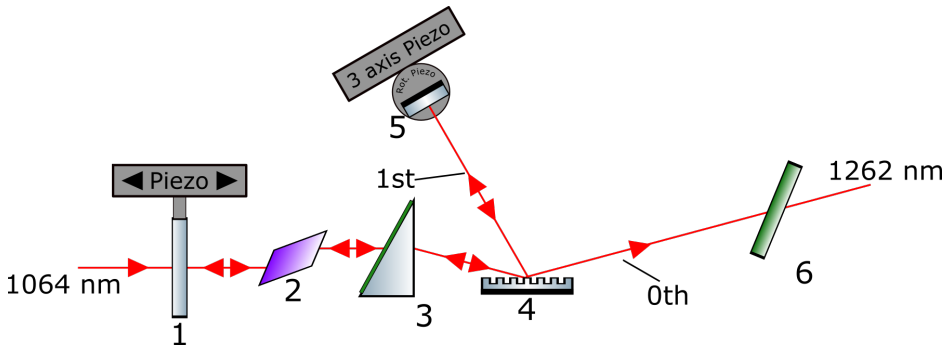

Figure 4.5: Cr:forsterite oscillator block scheme: dichroic mirror (1), Cr:forsterite crystal (2), right-angle prism expanding with entrance side AR coated @1.06 μm(3), diffraction grating (4) and back mirror (5), window with AR coating @1.06 μm (placed at 56° respect to the beam) (6).

tor is placed in correspondence of the dichoric mirror (1), which acts as the first cavity mirror, and the other two piezomotors are placed on the mirror (5) on the 1^{st} order reflection from the grating (4). The first linear piezomotor moves the mirror (1) back and forth changing in this way the length of the final Cr:forsterite cavity. One of the other two piezomotors (5) rotates the full assembly vertically, around an horizontal axis, enabling a precise alignment of the cavity, meanwhile the second one is a rotational piezo able to rotate the mirror around a vertical axis allowing the selection of the required frequency with a precision of 1.2 pm. When the mirror (5) and is rotated by the rotational piezo, the cavity slightly mis-aligns, requiring some fine-tuning using the vertical and linear piezos. This piezomotor system is connected directly to the already described FLC program and can act autonomously to keep the laser beam in a stable single-mode condition (SM condition). A further two-axis piezomotor (not showed in figure 4.5) is also placed after the filter (6) on a 1.26 μm mirror to correct the small movement of the beam caused by the realignment of the cavity. This

movement, which in principle is of the order of some μm, can negatively affect the energy amplification in the amplifying stages by mis-aligning some of the stages. This piezo, is automatically controlled by the FLC, checks the position of the beam collected using a camera placed on the path of a secondary diverged beam, which is previously frequency-doubled using a second harmonic generation (SHG) crystal.

The single-mode condition

A long series of tests were performed to try to increase the energy and the stability of the oscillator itself, without an active control by the operator or by a program. The oscillator proved to be the main source of instability of the complete FAMU laser system and the reflections of stray beams on the inner aluminium surface of the cover could cause a complete loss of the SM condition. Variations in the lamp condition and thermal fluctuations could also cause changes in the energy amplitude, increase pulse time jitter and cause loss of the the SM condition. To avoid, at least in part, these issues, the aluminium surfaces that could affect the beam quality were masked with light absorber and the complete laser system was inserted into a large laser cover able to maintain more constant temperature and humidity conditions. The lamp was replaced and a series of spare lamps were prepared in case of need. The SM condition could be checked either with a wavelength meter able to measure the linewidth, that in case of a SM beam is the smallest possible achievable by that device, or with a technique involving the use of a Fabry-Perot etalon. Unfortunately, during the first part of the measurements we were not equipped with a wavelength meter for this wavelength (1.26 μm) and for this reason we performed all these tests using the Fabry-Perot etalon technique. The beam coming from the oscillator, expanded with a concave/divergent lens (f_1 = -10 cm), was injected in the Fabry-Perot etalon (synthetic fused silica, 48 mm clear aperture, length of 30 mm, with design finesse 36 and free spectral range 3.45 GHz) and was then focused on the CMOS sensor of a camera with a convex/convergent lens (f_2 = 25 cm). We used different cameras during the various measurements, but these changes did not interfere with the final result. The cameras used during these tests were the Basler, model acA2040-25gmNIR, and the Gentec Beamage-4M.

An example of an image collected by the camera is shown in figure 4.6.

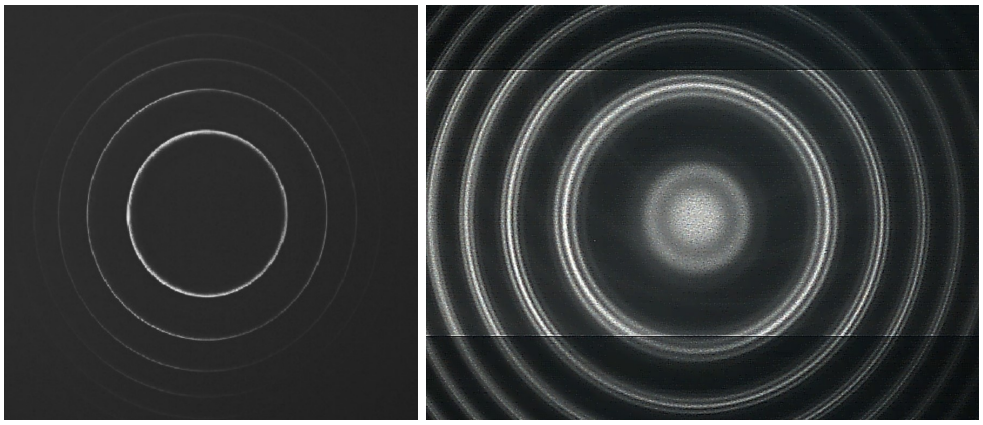

Figure 4.6: On the left, the interference fringes produces by the Fabry–Perot etalon when the system is working in SM. On the right, an example of interference fringes of a multi-mode laser beam.

In the image a set of concentric rings with different thickness Δr and radius r can be seen: knowing the pixel dimensions of the camera, the focal length of the focusing lens f_2 and the wavelength λ of the laser beam, we could calculate the linewidth $\Delta\lambda$ following this rule [28]:

$$\Delta\lambda = \lambda \frac{r\Delta r}{f_2^2}.$$

The wavelength used in this formula was measured through a spectrograph working in the visible spectrum coupled to a SHG crystal to halve the wavelength from around 1.26 μm to 631 nm. As before, the linewidth can tell us if the SM condition is satisfied or not, but also the rings image gives interesting information. In fact, if the rings are arranged in pairs, it means that the beam is dual-mode, while if the rings are broad and very large the beam will be multi-mode, as shown in figure 4.6.

The system was automatized, allowing the real time measurement of the linewidth during the movement of the piezomotors. I developed a program, showed in figure 4.7, able to collect the ring image directly from the camera, which can be seen almost in the center of the graphical interface, and according to the parameters set (left side), it can perform a scan on the image looking for the center of the rings. The algorithm used by the program to find this center is the maximization of the distance of the

peaks in the graph produced taking a horizontal section of the image. An example of the search for the maximum of this distance can be seen on the bottom-left graph (figure 4.7), showing the two peaks of the internal rings. At this point the two peaks are fitted to measure the thickness, one of the parameters required by the formula to calculate the linewidth. Once the radius of the ring is found as half of the distance between the two peaks and the thickness is derived as a mean of the two thicknesses calculated from the standard deviation of the fits, the linewidth calculation is performed automatically.

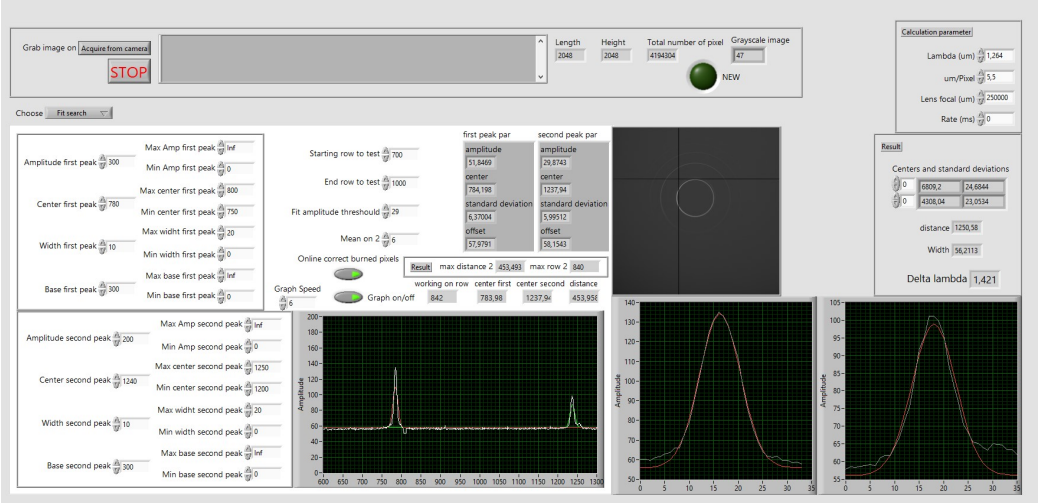

Figure 4.7: In this image it is shown the graphical interface of the specific program developed to calculate in real time the linewidth of the 1.26 μm laser beam using the image collected from the camera after the Fabry-Perot etalon. In the center, the rings image is visible which is analyzed using all the parameter shown on the left. On the right, inside the result box, there is the measured linewidth.

The system provided a direct measurement of the SM condition, but since its loss could also affect other laser features, such as energy and time jitter, all those parameters were investigated during those tests to identify the most reliable (and feasible) one that could highlight the laser SM condition.

A decrease in the energy of the laser beam could be an effect of the loss of the SM condition. Similarly a decrease of the energy stability, or

an increase of the energy jitter, could also be an indicator of an out of SM situation, even though increased energy in multi-mode was observed in some cases. For this reason, and also to spare all the possible energies produced by the oscillator, this parameter was not elected to monitor the SM condition, but was very useful to select the most stable SM piezo position.

The time shape of the laser pulse was greatly affected by the loss of the SM condition. As can be seen in figure 4.8, the smooth curve given by a SM beam can be recognized very clearly in the C) plot, this is why it was our measurement of choice during the alignment of the oscillator cavity. The issue with this measurement was the difficulty of coding a program that could recognize the laser SM behavior.

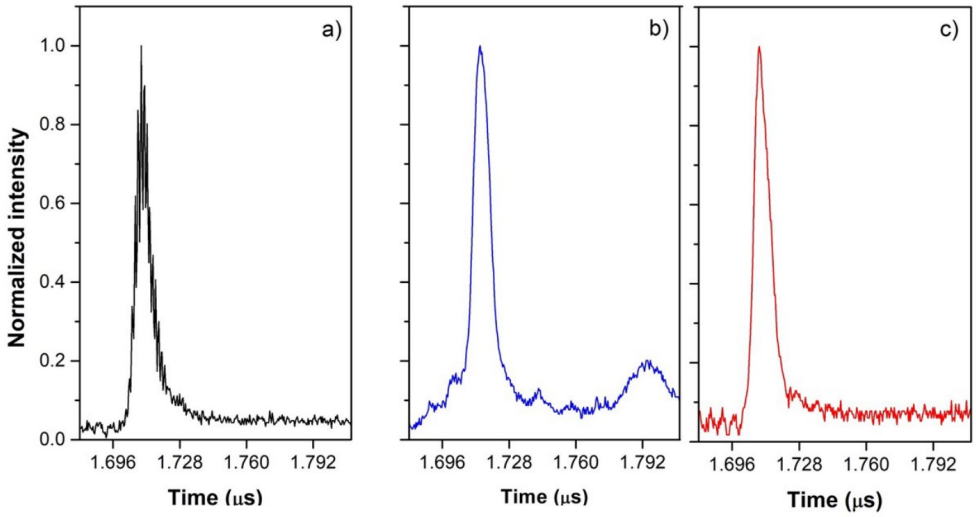

Figure 4.8: In this image there are 3 different pulses collected with the InGaAs pin-photodiode detector and recorded by the oscilloscope. In a), a multi-mode pulse that can be recognized from the multiple close peaks. b) a dual mode pulse visible as the smooth first peak and the small bump on the right. The last one c), a single mode pulse with its smooth pulse shape.

The time of formation of the laser in the cavity and the time jitter of the pulses were monitored. Both pulses of the figure 4.8, are measurements made with a InGaAs pin-photodiode detector, directly connected and recorded by the oscilloscope. A reflection of the laser beam is collected by the photodiode instantly forming an electric signal which can be observed in the scope. The above mentioned parameters are then calculated by mea-

suring the delay between the laser trigger and pulse collected by the photodiode. Large fluctuation of this delay, i.e. jitter, were produced by non SM-condition, but this parameter was not reliable as the delay itself.

The last parameter tested to monitor the single-mode condition was the time that took to the cavity to produce a pure 1.26 μm laser beam, which decreases to a minimum when the SM-condition is reached. From a simplified point of view, to create a SM laser beam in the cavity less reflections are needed to have stimulated emission in the active medium. This behavior was tested and proved to be reliable and stable enough for monitoring the SM condition. Therefore this parameter was selected as the reference value for the automatic system to maintain the SM condition. In the two graph-

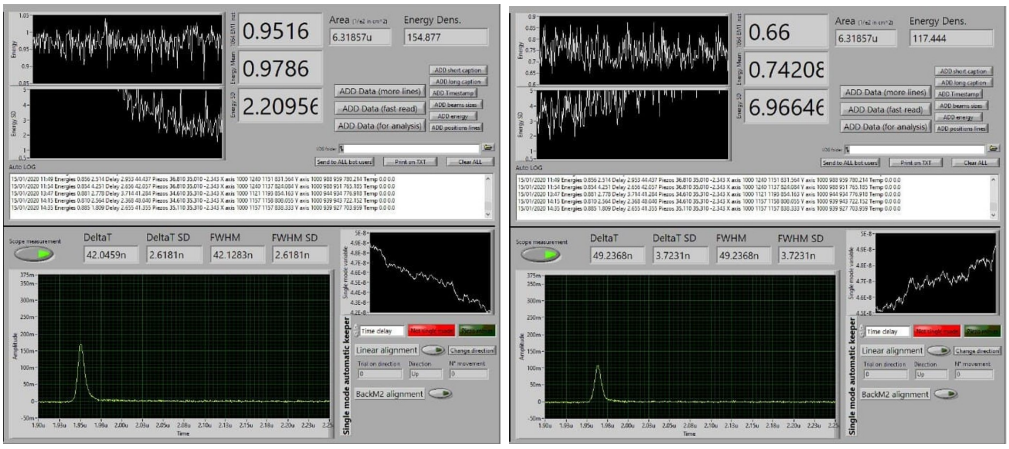

Figure 4.9: These images are taken from the FLC program which controls the oscillator. They show two different SM conditions: on the left image the system is entering in SM, on the right, it is starting to loose the SM condition. This can be observed from the lower energy and bigger energy jitter (the two plots in the upper side) of the non SM beam versus an SM beam. More clearly, in the plots on the right side of each screenshot, the trend in time of the delay of the laser pulse from the laser trigger is shown. When the beam is reaching the SM condition the delay decreases, while it increases when exiting the SM condition. In these images the system which keeps automatically the SM condition was disabled.

ical interfaces, showed in figure 4.9, the SM condition can be observed directly from the FLC program which controls the oscillator. In the upper part of the screens, two plots show the trends of the energy and the energy

jitter. As can be seen, when entering SM situation, the energy is greater than in the other case and also the energy jitter is decreasing. More interestingly, the bottom parts of the interfaces show the pulse shape as collected by the scope with the two measurements of the delay and the time jitter of the pulses. On the right side one can observe the time trend of the delay showing a clear correlation between the decreasing of this value and the beam entering in the SM condition. In fact, in the right image corresponding to the exiting from the SM situation, the delay value starts to increase. By tuning the delay, the system is able to keep the parameter under control acting on the linear piezo of the cavity, therefore keeping the SM condition.

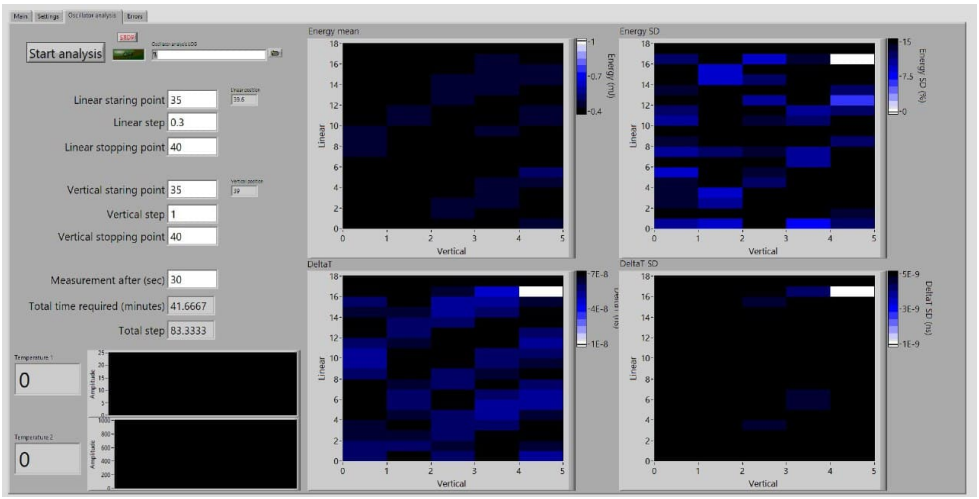

Figure 4.10: The image shows the four plots resulted from the campaign of measurement made changing the position of the linear and vertical piezomotors. All these plots showed the same behavior with the diagonal lines.

Further tests were performed to better understand the best pair of values for the linear and vertical piezomotors. The test was performed automatically using a program that I specifically developed for this purpose and which is now part of the FLC program that controls the oscillator. The program is able to scan the entire ranges of the two piezomotors and for each point it measures the energy, the energy jitter, the delay and the time jitter of the pulses. The result of this measurement (figure 4.10) showed

diagonal trends on all the 2D plots, in which X and Y are respectively the linear and vertical position of the piezomotors and the Z axis (given in color) represents the parameters listed before. The plot that shows the most clear effect is the bottom-left one, the measurement of the delay of the time beam. Similar trends can also be observed in the other plots and this means that all these parameters can be used as reference for the SM condition and are strongly correlated. It can also be observed that not all the SM positions found had the same energy and stability, showing that only some configurations are optimal for the final experiment. By repeating the experiment, different positions in the lines were found depending strongly on the temperature and on the stability of the laser pump itself.

4.3.2 Amplifier development and characterization

The multi-pass cavity tests

The energy of the 1.26 μm beam required in the DFG process to produce more than 1.5 mJ at 6.8 μm, necessary to have a good signal to noise ratio for the experiment, is more than 20 mJ. The oscillator, as described before, does not reach this value and a common approach in these cases is to build a system based on a Master Oscillator Power Amplifier (MOPA) configuration, to increase the energy of the pulses adding more amplifying stages. This approach was extensively tested by the FAMU laser team on a test bench formed by a single amplifying stage[29]. The setup was developed primarily to test a single crystal multi-pass configuration. To amplify the 1.26 μm beam another Cr:forsterite crystal similar to the one present in the oscillator was needed. The crystal was pumped with a Nd:YAG laser and a series of mirrors were positioned and aligned to reflect the beam coming from the oscillator into the crystal, giving up to six passes through the crystal, resulting in a configuration like the one shown in figure 4.11.

The experiment was performed with the oscillator able to deliver between 0.8-1.0 mJ in a stable SM condition, 7.5 ns pulses with a time jitter of $\pm$2.5 ns and a Innolas Spitlight 600 Nd:YAG laser producing up to 150 mJ in 18 ns pulses and time jitter below 0.5 ns. Both lasers were operating at 25 Hz and synchronized with a Quantum Composer 9520 pulse generator, selecting the correct delay which maximized the energy produced by the crystal. The beam dimensions were also increased to better match the entire surface of the crystal and increase the efficiency even more. In

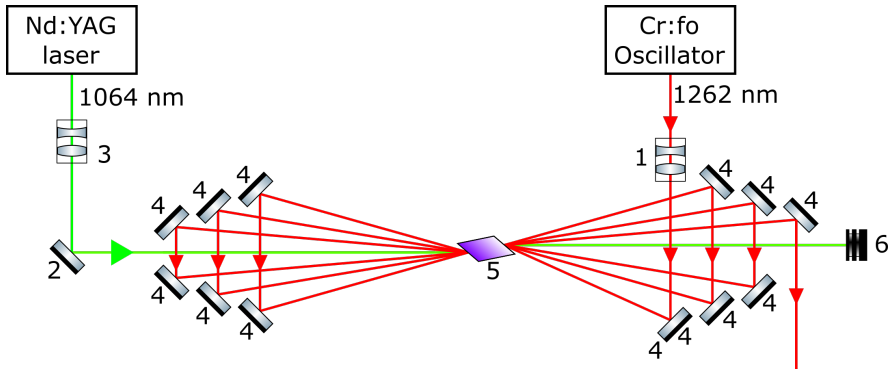

Figure 4.11: Scheme of the Cr:forsterite six-passes amplifier test-bench. decreasing telescope 1.26 μm (1), turning mirror 1.06 μm (2), decreasing telescope 1.06 μm (3), turning mirrors 1.26 μm (4), Cr:forsterite crystal (5), beam stop (6).

this condition we measured the energy using the Coherent EnergyMax-USB J-25MB-HE and J-50MB-YAG, the timing pulse shape using two InGaAs pin-photodiode detector (ET-3010, Electro-Optics Technology, Inc), recording the signals from them with a 2 GHz oscilloscope (Lecroy WaveRunner G 6200A). With a SPIRICON IEEE-1394 digital camera (model LBA-FW-SCOR20) we collected the beam dimension, shape and, through a Fabry–Perot (FP) etalon, the SM condition of the beam. The alignment of the mirrors to achieve six passes through the crystal, brought the energy of the multi-pass amplifier from the initial 0.8 mJ to 10.8 mJ, with a total gain of 13.5. The energy was measured after every pass obtaining the graph in figure 4.12. In this graph it can be seen that we did not deplete the crystal energy with six passes, as the trend is linearly increasing, but for lack of space we have not been able to place additional mirrors. The first mirrors are positioned with an angle of around 5-6°, while the last ones have almost 2-3° and this difference can be observed also in the graph 4.12: in fact, the first mirrors are less efficient because their angle is above the Brewster angle respect the crystal surface.

This type of behavior can be described with the model developed by Frantz and Nodvik[30], which is able to predict very precisely the gain of a single-pass amplifier. The equation is based on a quasi-two-level model, with the gain medium described with two populations n_1 and n_2, respectively for the lower and upper lasing level. The gain given by an amplifica-

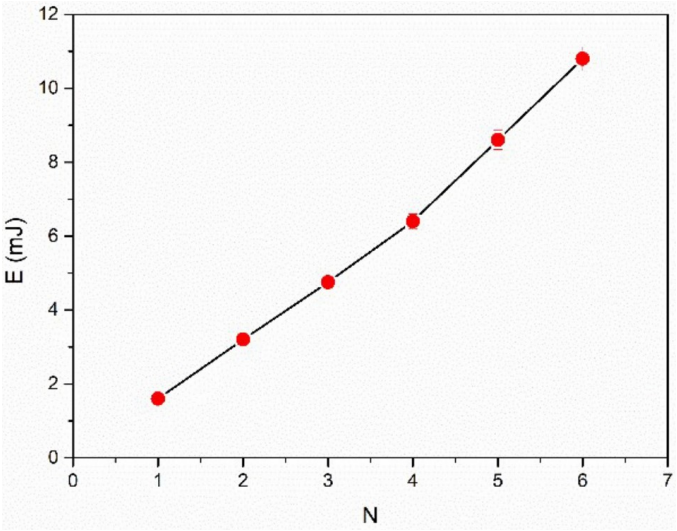

Figure 4.12: This graph shows the energy increase with the number of passes through the Cr:forsterite crystal. The curve is straight, meaning that we did not deplete the crystal with 6 passes, but unfortunately adding more passes was not possible due to lack of space.

tion process of this type can be calculated as:

$$G = \frac{E_s}{E_{in}} ln \left\{ 1 + \left[exp\left(\frac{E_{in}}{E_s} \right) - 1 \right] G_0 \right\},$$

with $G_0 = exp(g_0 L)$ the small signal-only single pass gain, calculated from the length of the crystal L and $g_0 = n\sigma$. The other variables in the equation are the saturation fluenceE_s, the input fluence at the entrance of the amplifier E_{in}, the inversion population density $n = n_2 - n_1$ and the stimulated emission cross section σ. Differently from single-pass amplifier, this calculation is not able to predict perfectly the final result for a multi-pass amplifier, which in various cases results in an overestimation of the final experimental result. In fact, a lot of other factors are not taken into account, like the absorption in the medium, heating, and thermal lensing [31]. For the simulation of our system we used a saturation fluence E_s = 0.82 J cm^{-2} and a cross section σ = 1.44 10^{-19} cm^2 .

Further tests where performed at low temperature using the same setup, searching for the possibility to exploit a possible significant gain increase in the amplifying stages. The crystal was placed in a support able to cool

the active medium down to -15°C in a humidity controlled atmosphere to avoid the formation of moisture on the surfaces of the crystal. The crystal support was fixed on a double layer Thermo-Electric Cooler (TEC), or Peltier cell, which was connected to a liquid heat sink, closed on the two sides facing the laser path with a couple of CaF_2 windows to minimize NIR light absorption. The cell was then fluxed with dry air to avoid moisture on the surfaces. The final apparatus can be seen in the infrared picture in figure 4.13, showing the temperature reached on the outside surface of the cell. The setup was at this point realigned to compensate the deviation of

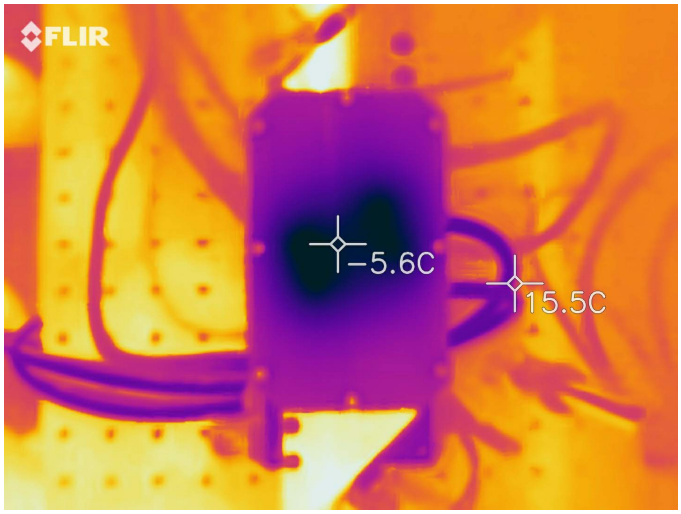

Figure 4.13: An infrared picture of the test bench with the cooled crystal to -5°C.

the beam caused by insertion of the windows on the beam path. The cooled system showed a little increase in the amplification gain, but due to the use of windows to close the cell, we also observed that part of this gain was lost due to the absorption of the windows. In fact, the laser beam passes 12 times on the windows (two for each pass through the crystal). The increase of the gain can be appreciated in the plot in figure 4.14, showing a mean gain between 10°C and -15°C of around 10%. This result at low temperature was promising, but we decided to concentrate on the multi-crystal multi-pass amplifier, able to ensure higher energies.

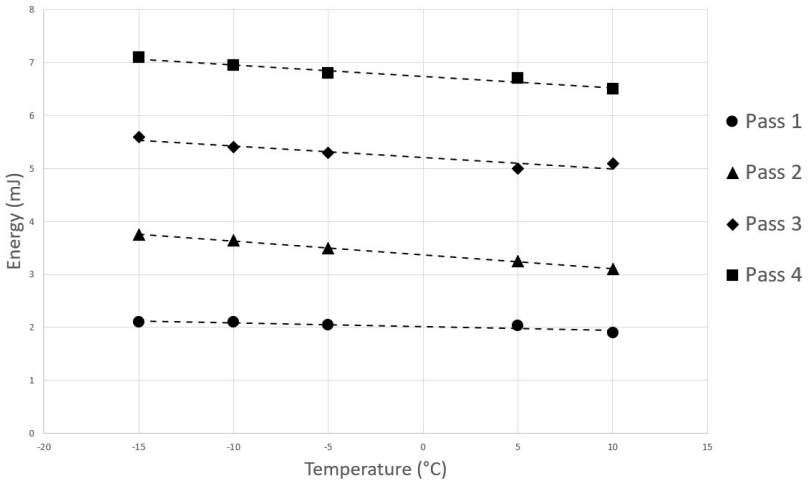

Figure 4.14: The plot shows the efficacy of the Cr:forsterite crystal cooling for increasing the amplification. The tests on different temperatures were done for every single passage in the crystal. The initial energy of the oscillator was 0.9±0.1 mJ.

The three stage multi-pass amplifier

The development of a multi-stage multi-pass amplifier started from a MOPA, purchased from Lotis, which was formed by three Cr:forsterite crystal, pumped by a powerful Innolas Nd:YAG, in which the laser beam coming from the oscillator was injected. As can be seen in figure 4.15, the 1.26 μm laser beam passed through each crystal two times, with a total of six passes[24].

Starting from the knowledge acquired during the tests on the multi-pass cavity, we decided to improve the Lotis MOPA adding additional passes for each stage. After some initial tests, the team decided to pursue a design based on 6 passes for the first two crystal and four passes for the last one. A new complete set of optomechanics, optics and adapters was needed to complete the building of the MOPA. An image of the final setup with all the mirrors needed for all the passes can be seen in figure 4.16.

The challenging part at this point was the alignment of all the passes, keeping in mind that the beam is in the infrared region and the use of a visible laser beam was impossible due to the high crystal absorption at visual wavelength. An example of the difficulties can be seen in the two pictures

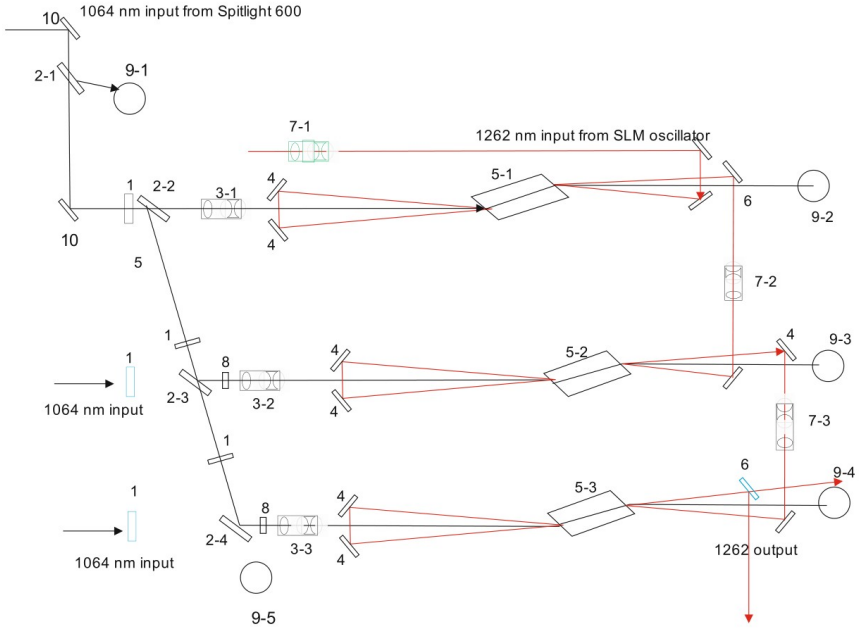

Figure 4.15: The laser amplifier module as provided by Lotis. In the scheme: retarding half-wave plate ($\lambda/2$, 1.06 μm) (1), polarizer (1.06 μm) (2), pump telescope (1.06 μm) (3), turning 1.26 μm mirrors (4)(6), Cr:forsterite active element (5), 1.26 μm increasing telescope (7), rotator 90° (1.06 μm) (8), beam stop (9).

in figure 4.17, where on the left there is the amplifier in the visible light, but the beams entering the crystal can be seen on the right side using an infrared visualizer only. For this reason the use of infrared visualizer card was necessary to perform the alignment. The final result of the development is the amplifier described in the previous chapter in 3.5.

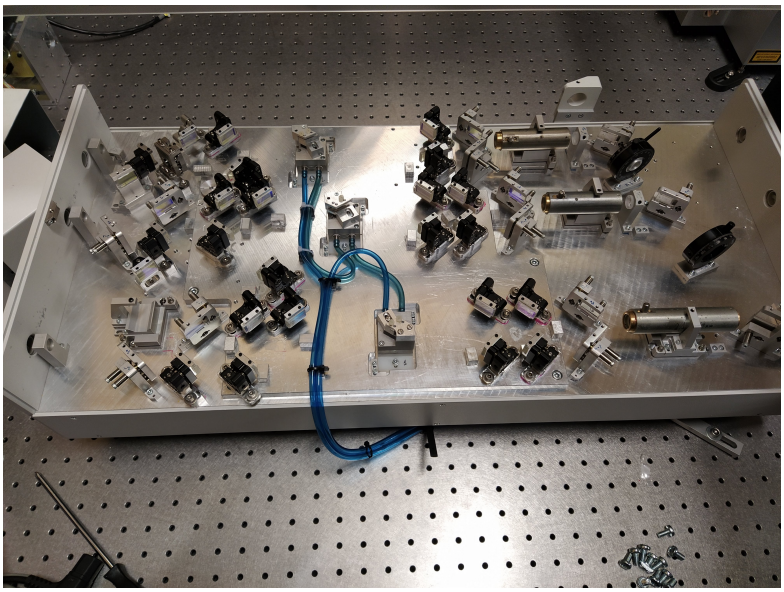

Figure 4.16: The picture shows the amplifier for the 1.26 μm laser beam. The black and some of the grey mounts supports for the mirrors needed for all the passes. In the center of the image, the three Cr:forsterite crystals inside their heat sink holders. The beams from the 1.06 μm pump arrives from the right.

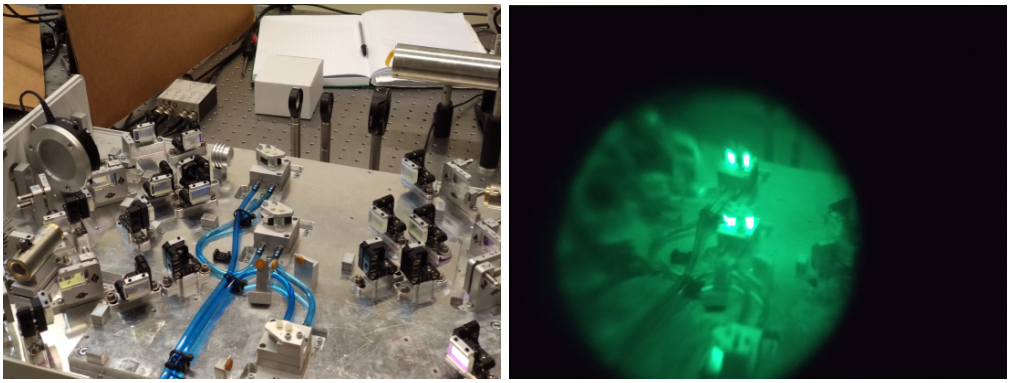

Figure 4.17: One of the main difficulty of this work was the alignment of all the mirrors with infrared light. On left the amplifier setup in visible light. On right a picture the same part of the setup through a infrared viewer. The brighter spots are the Cr:forsterite crystal pumped by the Nd:YAG laser.

4.3.3 DFG setup development and characterization

The purpose of such a precise laser in the 1.26 μm wavelength is to act as a signal in the DFG setup. As anticipated, the Difference Frequency Generation, or DFG, is an optical non-linear process which involves waves from two different frequencies ω_1 and ω_2, in our case 281.72 THz (1064 nm) and 237.54 THz (1262 nm), to produce a third wave with a frequency $\omega_3 = \omega_1 - \omega_2$ which is the subtraction of the initial two, 44.18 THz (6785 nm). The higher frequency beam brings the active medium to the higher possible energy level and the second one stimulate the downward transition to an intermediate level, from which the DFG photon is emitted[32]. A graphical scheme of this process can be seen in figure 4.18. This process is performed inside non-linear crystals, which need to be aligned under very precise time, spatial, polarization and angular conditions.

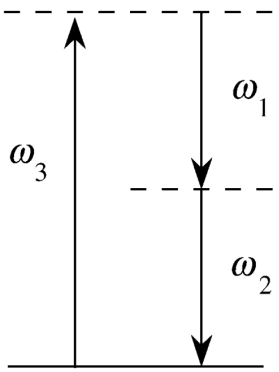

Figure 4.18: A scheme of the DFG process inside the crystal.

The first condition is the time synchronization between the pump and signal beams. The two laser beams must match perfectly in time during the passage inside the crystal in order to produce the required 6.8 μm light. The pump beam should have a slightly longer pulse in order to contain completely the signal pulse. In this way, the system will be also more reliable to potential time jitter fluctuation. This synchronization can be performed through the pulse generator used to trigger the two laser heads or changing the laser path to a length needed to synchronize in time the two beams when they arrive to the crystal. In our setup the synchronization is made using the first method, triggering both the lamps and the Q-switches

to match very precisely the two beams up to 100 ps. The importance of having a low jitter lasers is now explained. In fact, in some cases a less energetic but more stable laser beams is able to produce more 6.8 μm light respect to a more energetic but less stable beam. The precision needed on the synchronization can be deduced from the plot in figure 4.19, where a complete scan in delay between the two laser beams was performed, showing that also a delay difference of 10 ns can halve the energy produced in the DFG process. Choosing the right delay can be done by maximizing the energy along that curve or, in a more practical way, aligning the two laser pulses collected from a pin-photodiode and shown on the oscilloscope screen. This synchronization tuning must be performed every time the energy of the laser head pumps are changed, in fact the formation time of the laser beam inside cavities strongly depends on the energy delivered by the flashlamps or by the diodes. All the measurements performed and showed in this thesis have delays optimized to obtain the maximum possible energy, looking to the pulses collected from the pin-photodiode.

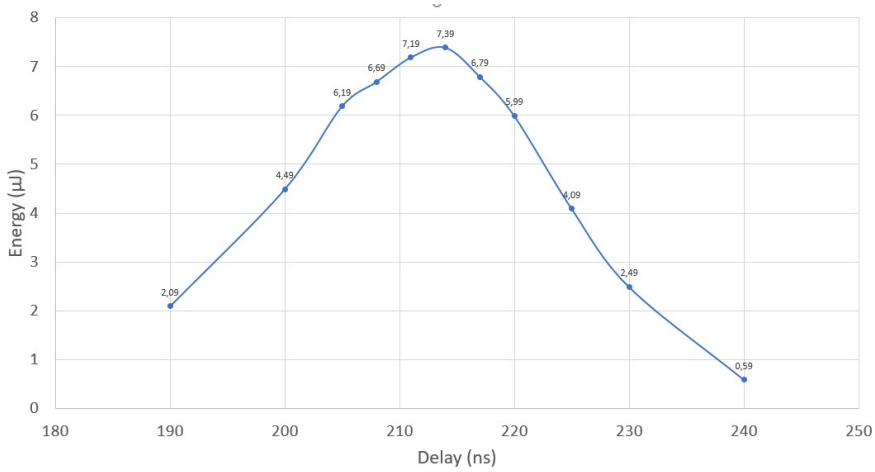

Figure 4.19: This plot shows how much the synchronization of the two laser beams entering the NL crystal heavily affects the energy produced in the DFG process. A variation of 10 ns halves the energy at 7 μm. This measurement was performed with a $BaGa_4Se_7$ crystal of 7x7x6 mm^3 with beams 7 mJ @1.26 μm and 12 mJ @1.06 μm.

A perfect timing of course is not enough to start the DFG process. The two beams must also match spatially, entering perfectly co-linearly inside

the NL crystal. To obtain this result a di-chroic mirror, able to transmit the 1.06 μm and reflect the 1.26 μm beam, was placed in front of the crystal and used to combine the two beams in a unique one and routed directly inside the NL active medium. This step ensures the delivery of the photons of the two beams in the same volume inside the crystal, increasing the DFG efficiency.

Another condition is the relative direction of the polarizations of the two incoming beams. This condition depends on the characteristics of the crystal lattice, giving as result a system of different types of polarization alignment, from type I to type VII, depending on the crystal structures and materials. The configuration suggested in literature for the crystals that we used in our test is the type I, in which the pump is aligned as extraordinary *e* beam and the signal ordinary *o* beam. The first, or the *e* beam, has the polarization aligned with the plane passing through the axis of the beam and the projection of the axis on the surface of the crystal. The signal, or the *o* beam, has the polarization perpendicular to the *e* beam along the same beam axis. For our test this means that the two beams must have relative orthogonal polarization. This is know as Phase Matching condition. It is clear that the polarization affects directly the design of the DFG setup. To facilitate the work of the crystal alignment and to keep the beam parallel to the optical table, needs the polarization of the pump laser, in our case the 1.06 μm beam, to be horizontally polarized. This restriction is imposed by the definition of e polarization which needs to enter in the crystal with a very precise and sensitive angle, that needs to be tuned every time the crystal is removed from the optical mount.

In the last paragraph we already cited the presence of important angles that must be matched to produce light from the DFG process. One of the critical points in the following description is that there is not only one system of coordinates, but there are three different systems. The first and most important ones are is the coordinates relatives to the crystal lattice, which are defined by the directions of the crystal in which the efficiency of the DFG process is maximized. The second ones are the coordinates created by the crystal producers when they cut the crystal matching at minimum one axis of the crystal lattice, the Z axis along which the light need to enter the crystal. The third and last coordinates are the ones referred to the laser beams entering the crystal, with the Z-axis on the direction of propagation of the crystal. The combination of the three coordinates systems will give a final idea of the θ and ϕ angles which are needed to describe the direction

of entrance of the lasers inside the crystal. θ is the angle between the Z-axis of the entering laser beams and the X-Y plane of the crystal lattice, which in our case is the surface of the crystal because the cutting of the producer matches the X-Y plane of the crystal. ϕ is the angle between the projection of the beam on the X-Y plane and the horizontal plane. The two angles can be visualized on the optical kinematic mount of the crystal in figure 4.20, where the ϕ angle is represented as the movement of the crystal around the grey aluminium mount axis, while the θ angle is the rotation around the vertical axis.

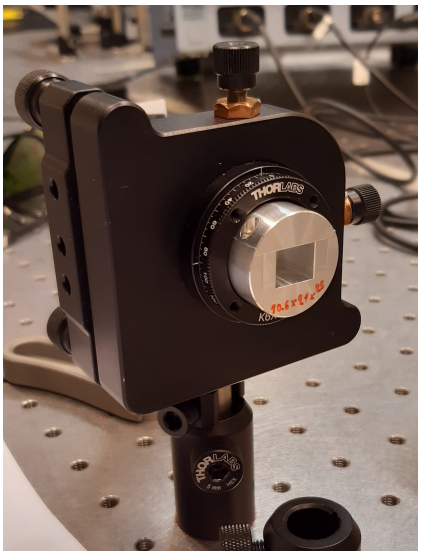

Figure 4.20: The picture shows a crystal holder in a 6-axis optical kinematic mount. The rotation along the crystal axis using the round gear in front of mount represent the ϕ angle. The movement around the vertical axis represents the θ angle.

After this introduction it is clear that the main goal of testing the DFG setup is to fully characterize the crystals that we have, in order to select the optimal crystal to be used in the laser during the final acquisition of the FAMU experiment. Five different crystal materials were tested to select the most convenient crystal for the experiment purpose: $LiInS_2$, $BaGa_4Se_7$, $GaSe$ and $LiInSe_2$. The tests focused on the first three types of crystals, in particular measuring the phase matching angles and the efficiency of the DFG process in the crystal.

Crystal test with Elettra setup

The tests were focused on the 6.8 μm energy dependence on the pump and signal beams energies. Part of the tests on the crystals have been performed using a different setup with respect to the one described up to now. All the crystal measurements of this paragraph were taken using as sources of 1.06 and 1.26 μm beams, respectively a Lotis LS2139DP Nd:YAG diode pumped laser and a Lotis LT2112 Cr:forsterite oscillator pumped with a Lotis LS2138 Nd:YAG laser. This setup is able to inject into the non linear crystal up to 10 mJ at 1.06 μm and 7 mJ at 1.26 μm. Both beams were not single mode, as the setup was used only to study the crystals angles and energies. The wavelength of the 1.26 μm beam can be changed moving the back mirror of the Cr:forsterite cavity similarly to what was done on the oscillator of the final setup. The back mirror is rotated using a manual microscrew.
The two beams were resized using irises to select the best dimensions for the experiments. The final measurements of the beam diameters and shape were performed using a SPIRICON IEEE-1394 digital camera. The diameters selected to perform the measurements described in this subsection is 3.5 mm for both beams. This value was chosen to have comparable area-independent measurements from all the crystals which had different section sizes. The measurement performed varying the beams dimensions was done exploiting the small divergence of the laser beam and moving the crystal position back and forth along the laser beam. The two beams, after been resized, were then combined using a dichroic mirror, which reflects the 1.06 μm and transmits the 1.26 μm.

The energy at 6.8 μm was measured with a Coherent EnergyMax USB-J-10MB-LE Energy Meter. Using the two combined beams, multiple crystals of multiple materials were tested to understand if they were suitable for the experiment requirements.

$LiInS_2$ The first material tested extensively was the $LiInS_2$. Three different crystals of different dimensions were tested. All the crystal dimensions will be given as surface sections times the length passed by the light. The $LiInS_2$ crystals there are parallelepiped crystals: 10×10×5 mm^3, 5×5×15 mm^3 and 8×8×18 mm^3. All these crystals were coated with an AR coating for 1.06, 1.26 and 6.8 μm lights.

These crystals are at present the most extensively tested. Having different crystals with different lengths was very useful to measure, for example, the increase of the 6.8 μm light energy when varying the length of the crystal. An example of this measurement can be seen in figure 4.21. The plot shows that the increase of the 6.8 μm energy is more than quadratic respect to the length, due to parametric oscillation effect, as described in literature [32]. For this reason longer crystals are advised to increase efficiently the energy of the produced beam.

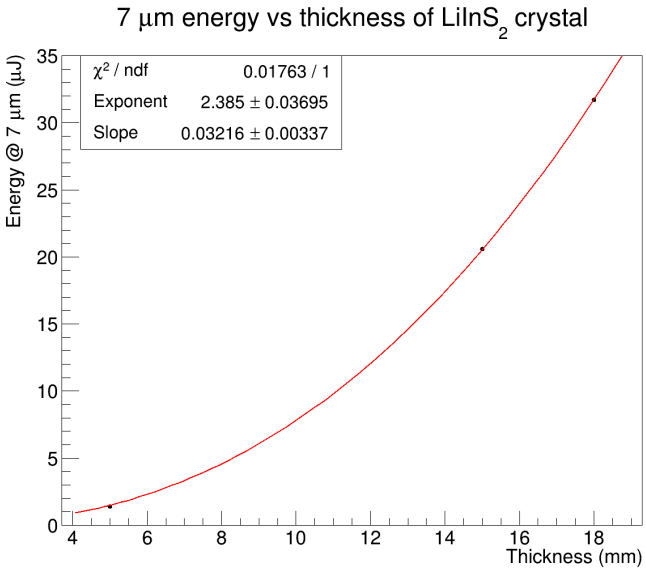

Figure 4.21: This plot shows the crystal length dependence of the energy produced in the DFG process at 6.8 μm.

The first of the $LiInS_2$ crystal had another interesting characteristic: it had a large surface that was optimal to test the efficiency variation of the DFG process varying the energy density of the entering beams. This test was performed keeping the energy of the beams fixed and at the same time moving the crystal along the beams to change the dimension of the illuminated spot. The effect of the dimensions variation can be seen in figure 4.22, where a larger beam with a smaller energy density produced less energy than a smaller beam with a higher energy density, considering the same total amount of energy in all three measurements. Other tests of this effect are ongoing.

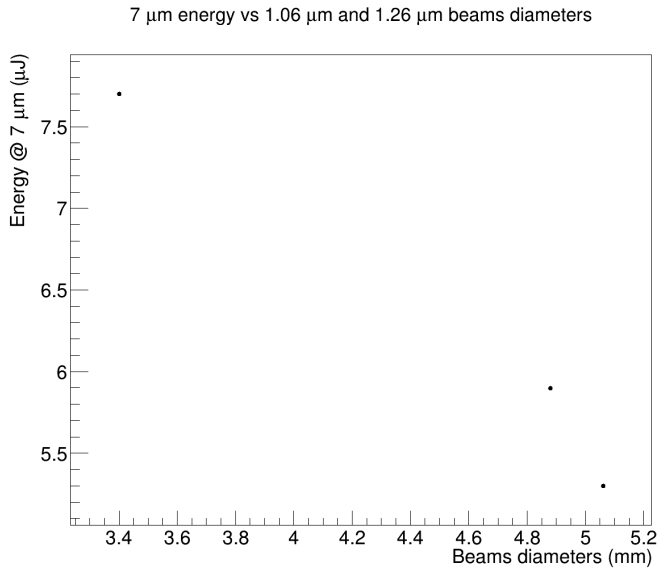

Figure 4.22: This plot shows the dependence of the energy produced in the DFG process on the beam diameter. Varying the beam diameter and keeping the energy constant means varying the energy density of the pump and signal beams.

More measurements were performed to see the energy produced by the crystals. In the plots in figure 4.23 the energy production at 6.8 μm is plotted varying the energy of the 1.06 μm beam keeping the 1.26 μm energy constant (left column) and vice versa, varying the 1.26 μm and keeping constant the 1.06 μm (right column). In this case, the effect of the energy density is not taken into account. The effect is more remarkable in the first column. The dependencies are linear with the energy of the two beams in both cases as expected from the literature.

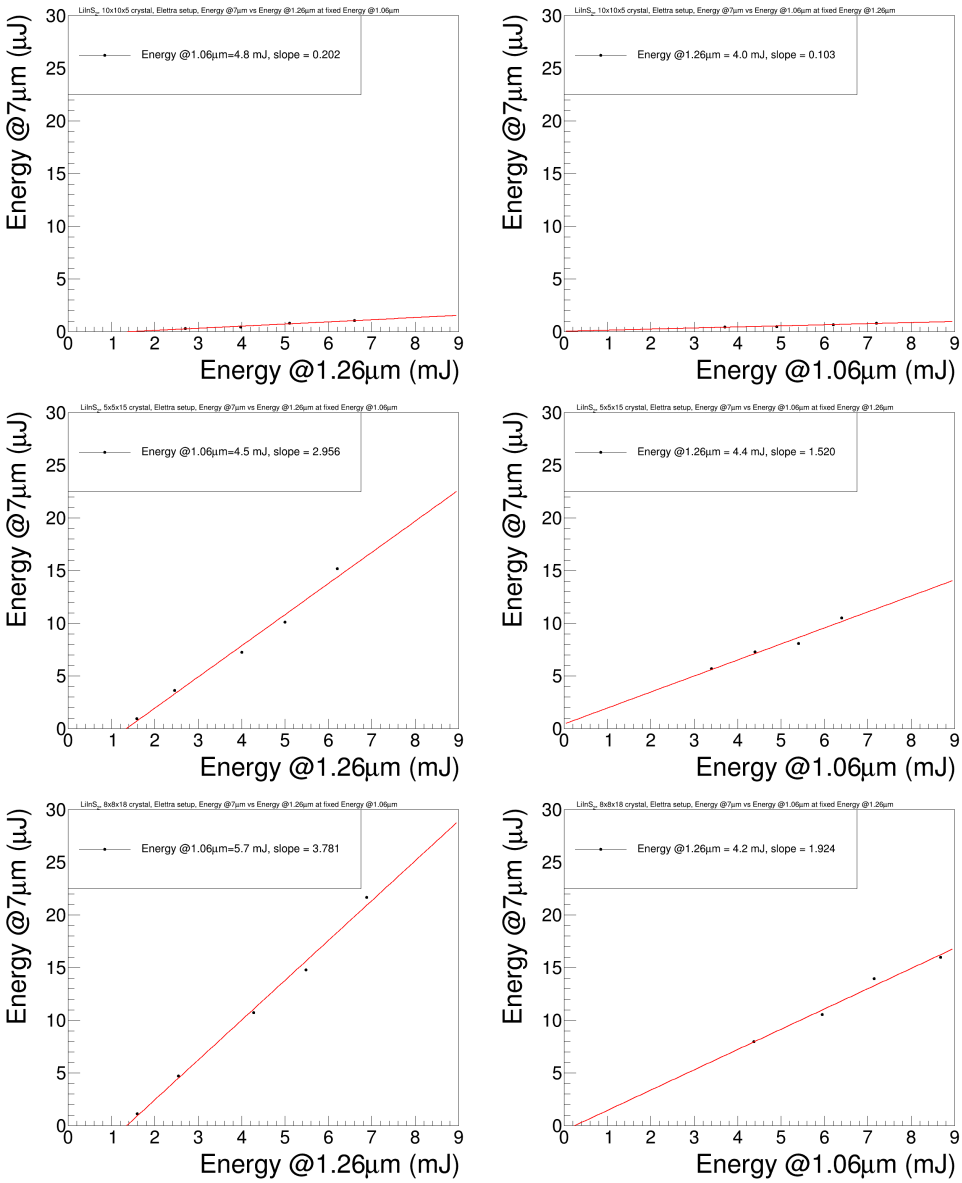

Figure 4.23: These plots show the energy production at 6.8 μm varying the energy of the 1.26 μm beam keeping the 1.06 μm energy constant (left column) and vice versa, varying the 1.06 μm and keeping constant the 1.26 μm (right column), with Elettra setup. The same measurements were performed with all three $LiInS_2$ crystals; First row 10×10×5 mm^3, second row 5×5×15 mm^3, and third row 8×8×18 mm^3.

$BaGa_4Se_7$ The second crystal material tested is the $BaGa_4Se_7$. One of these crystals has a darker color due to the higher barium concentration and will be called $BaGa_4Se_7$ red, while the lighter will be called $BaGa_4Se_7$ yellow. Of this material we had three crystals:

- a 7×7×6 mm^3, yellow, uncoated;
- a 7×7×6 mm^3, red, uncoated;
- a 10×10×27 mm^3, yellow, AR coated for 1.06, 1.26 and 6.8 μm.

The same measurement performed with the $LiInS_2$ varying the 1.06 and 1.26 μm light were repeated with these $BaGa_4Se_7$ crystals and the results are showed in figure 4.24. As can be seen, these crystals were more efficient than the $LiInS_2$, obtaining values comparable to the $LiInS_2$ 5×5×15 mm^3 with 1/3 of the length. For this reason, these crystals are the most promising for the final setup of the laser to obtain the required energy for the experiment.

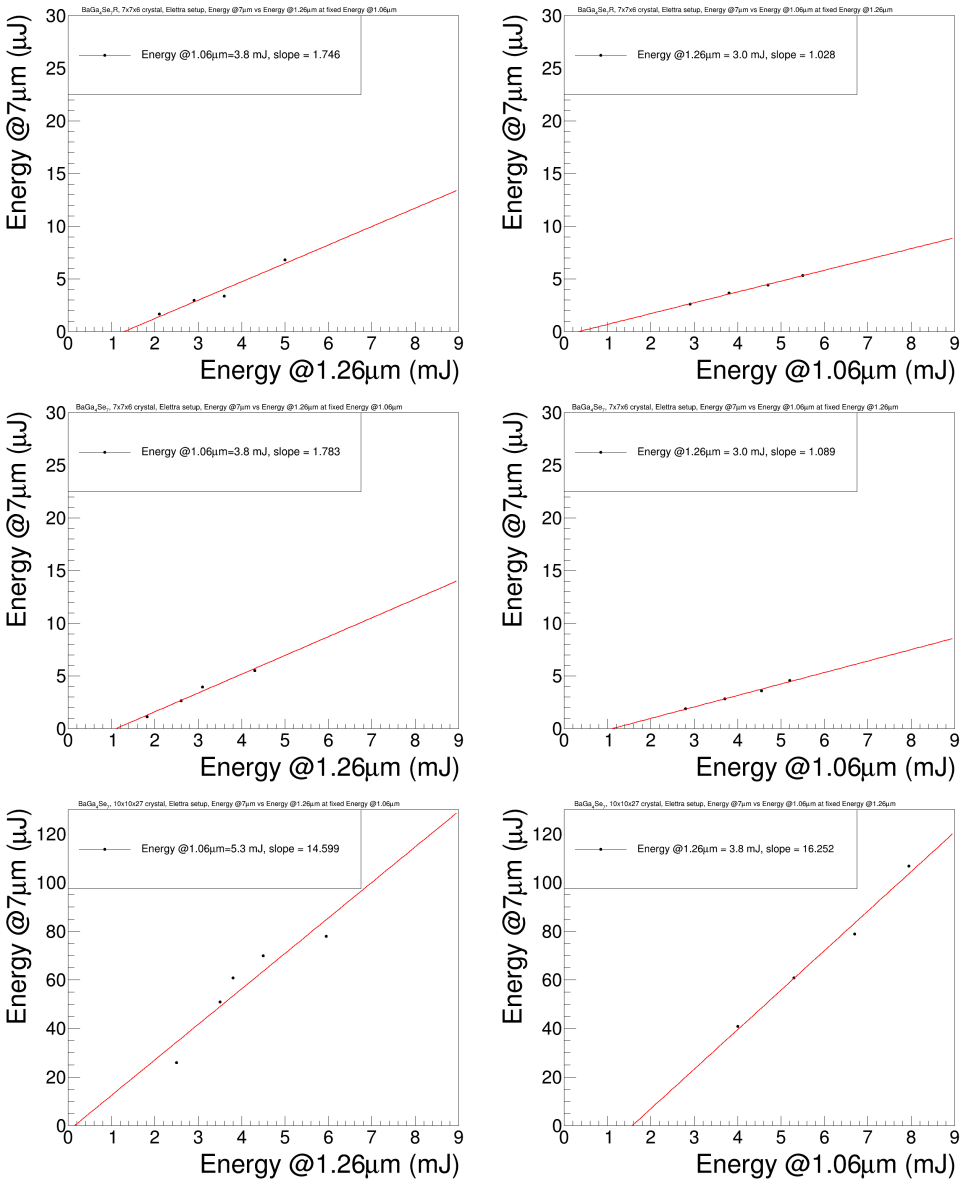

Figure 4.24: These plots show the energy production at 6.8 μm varying the energy of the 1.26 μm beam keeping the 1.06 μm energy constant (left column) and vice versa, varying the 1.06 μm and keeping constant the 1.26 μm (right column), with Elettra setup. The same measurements were performed with all three $BaGa_4Se_7$ crystals; first row yellow 7×7×6 mm^3, second row red 7×7×6 mm^3, and third row yellow 10×10×27 mm^3.

$LiInSe_2$ and $GaSe$ Other materials tested were the $LiInSe_2$ and $GaSe$. The first one showed a similar behavior to the $LiInS_2$, while the most interesting was the $GaSe$. This crystal showed the best results in term of efficiency, as can be seen in figure 4.25 where it shows a higher slope compared to the other materials. However the material characteristics are unsuitable for the application. In fact, the crystal cannot be cut along the Z axis, but only along the crystal lattice surfaces, and this gives as a result a 50° θ angle which forces to use large crystals to have beams completely passing through the crystal itself. Another issue is that it cannot be coated with AR coating because it is very fragile and for this reason 10% of the pump and 50% of the signal energies was lost due to surface reflection.

This last result can be seen also in figure 4.26, where the transparency of the crystal at 6.8 μm is shown. As can be seen there are two different groups of values in this plot: the higher values are in coincidence of crystals coated with AR coating for 1.06, 1.26 and 6.8 μm, while the other are not coated. This shows the importance of the coatings to increase the efficiency of the complete system.

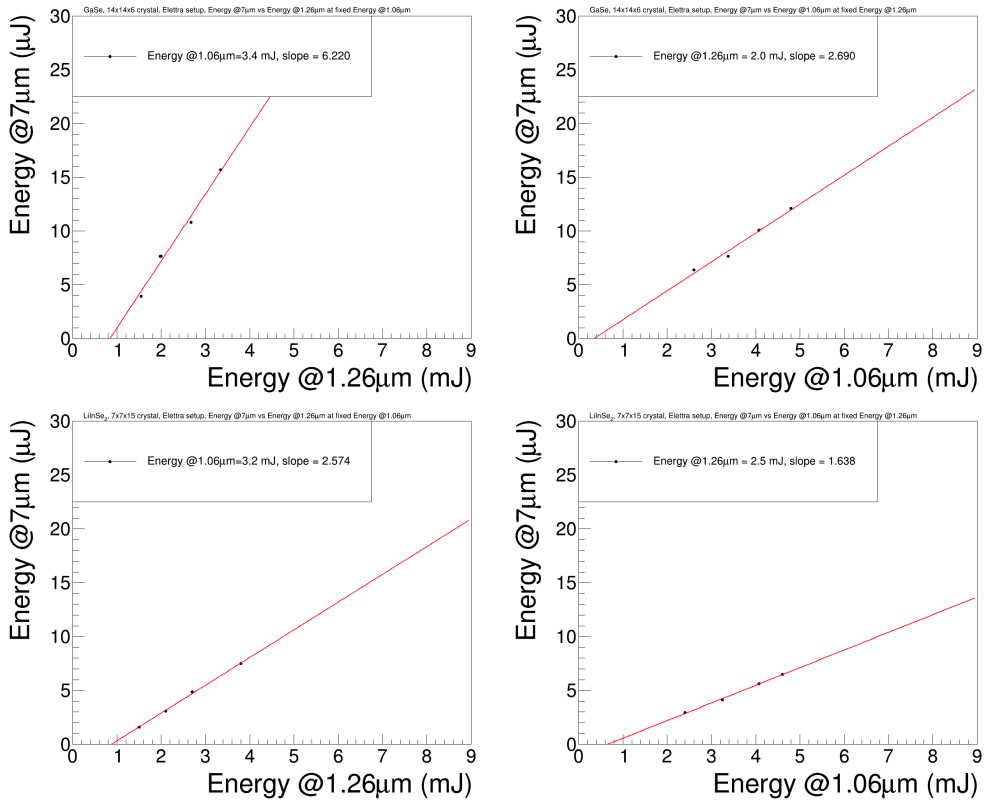

Figure 4.25: These plots show the energy production at 6.8 μm varying the energy of the 1.26 μm beam keeping the 1.06 μm energy constant (left column) and vice versa, varying the 1.06 μm and keeping constant the 1.26 μm (right column), with Elettra setup. The same measurements were performed with the $GaSe$ (first row) and with the $LiInSe_2$ crystals (second row).

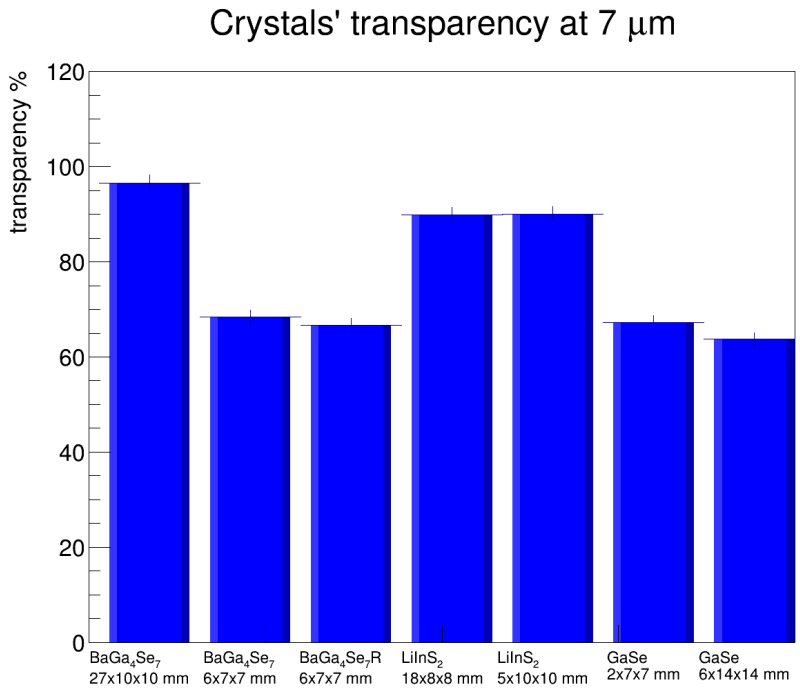

Figure 4.26: This plot shows the transparency percentage at 6.8 μm of the various crystals. The three crystals with the higher values have the AR coating, the others not.

Crystal test with RAL setup

As anticipated, the second part of the crystal tests were performed with the final setup of the laser that will be used in the data acquisition at RAL. This setup, described in chapter 3, is more powerful than the one used to test the non-linear crystal described in the previous 4.3.3 and during these tests it was able to produce more energy at 6.8 μm. The beam diameters were set with telescopes to 6 mm, to not exceed the damage threshold of the crystals and coatings using the higher energies of these lasers. More measurements were performed on the 6.78 μm beam to check the:

- energy;
- wavelength tunability and tunability step;
- wavelength stability;
- linewidth.

Most of the measurements were performed by varying the energy of the two pump and signal beams, the timing between them and with different non-linear crystals. All the 6.8 μm energies and their stability were measured using a Coherent LabMax TOP with a J-10MB-HE Energy Sensor, with an energy range between 10 μJ to 20 mJ. The wavelength and linewidth related measurements were taken with the HighFinesse Wavelength Meter WS6-200 IR III. The timing data about the 1.06 and 1.26 μm beams were collected with the same pin photodiode used for the other tests, while the timing data of the 6.78 μm were collected using a particular HgCdTe photodetector from VIGO System. Most of the stability tests were performed using a $LiInSe_2$ crystal 7×7×20 mm^3, which was burnt during the last measurement of the double pass measurement.

6.8 μm energy varying the 1.06 and 1.26 μm energies Measurements varying the 1.06 and 1.26 μm beams energies were performed with the RAL setup. The 1.06 and 1.26 μm energies were higher, giving as a result higher 6.8 μm energies for every crystals, as can be seen in figure 4.27 and 4.28. Unfortunately, we didn't have the 10×10×27 mm^3 yellow $BaGa_4Se_7$ crystal yet, but starting from the measurements made on the same material, we can aspire to obtain, using the current setup, up to 800 μJ.

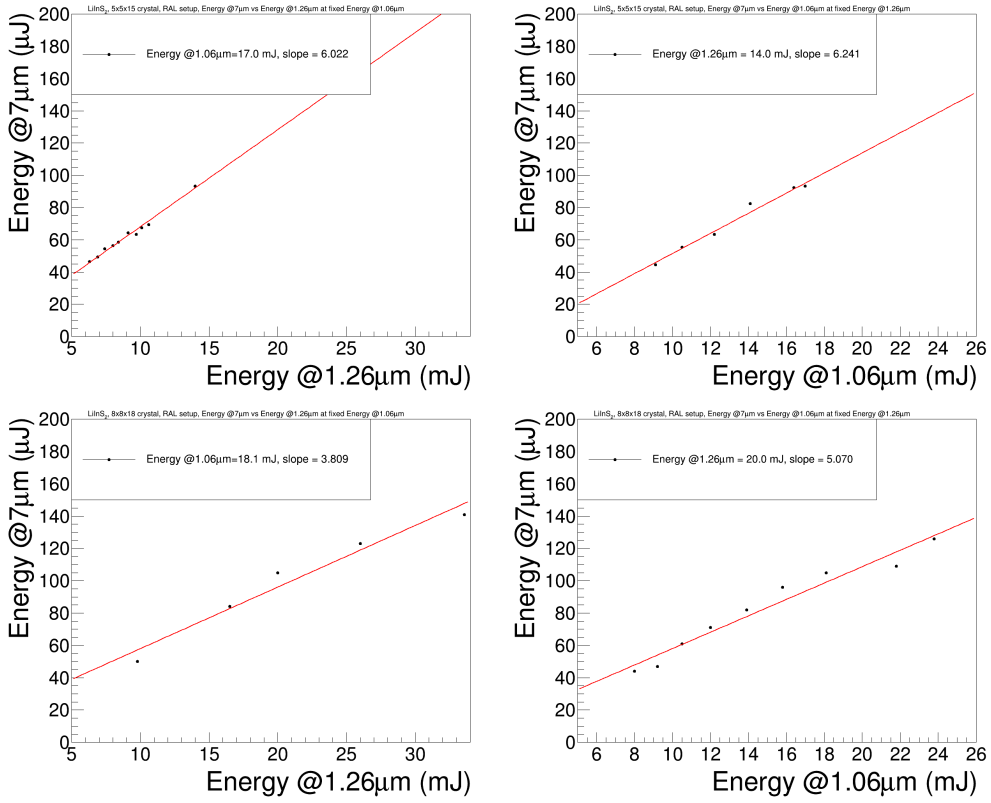

Figure 4.27: These plots show the energy production at 6.8 μm varying the energy of the 1.26 μm beam keeping the 1.06 μm energy constant (left column) and vice versa, varying the 1.06 μm and keeping constant the 1.26 μm (right column), with RAL setup. The same measurements were performed with the 5×5×15 mm^3 $LiInS_2$ crystal (first row) and with the 8×8×18 mm^3 $LiInS_2$ crystal (second row).

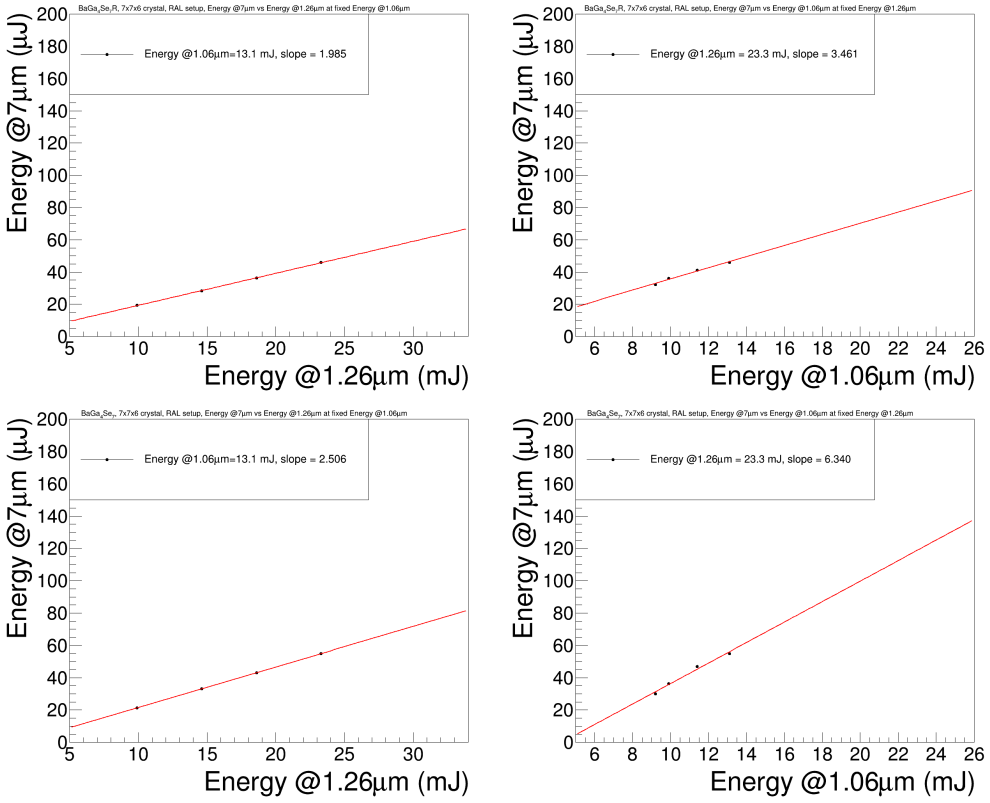

Figure 4.28: These plots show the energy production at 6.8 μm varying the energy of the 1.26 μm beam keeping the 1.06 μm energy constant (left column) and vice versa, varying the 1.06 μm and keeping constant the 1.26 μm (right column), with RAL setup. The same measurements were performed with the 7×7×6 mm^3 red $BaGa_4Se_7$ crystal (first row) and with the 7×7×6 mm^3 yellow $BaGa_4Se_7$ crystal (second row).

Two passes tests In order to obtain the maximum possible energy from a single crystal we added one more passage through the crystal. This configuration will be called double pass, and it was described in the previous figure 3.18. The results of these tests are shown in figure 4.29, where the energy produced by the DFG process was more than doubled adding one more passage through the crystal, doubling in this way the final energy. In figure 4.30 it can be seen the maximum energy reached at 6.8 μm from our laser using the crystals available when we performed this test. The maximum energy reached until now is 548 mJ using a 7×7×20 mm^3 $LiInS_2$ crystal.

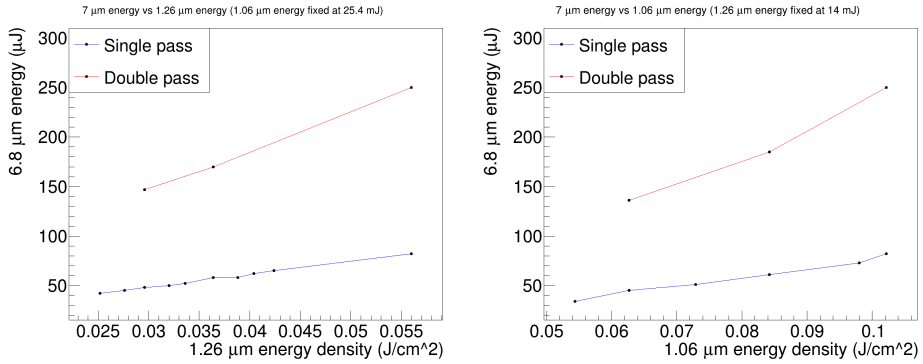

Figure 4.29: The increase of energy output at 6.78 μm as a function of the two injected laser energies in single and double pass configuration. These data were obtained with the 5×5×15 mm^3 $LiInS_2$ crystal.

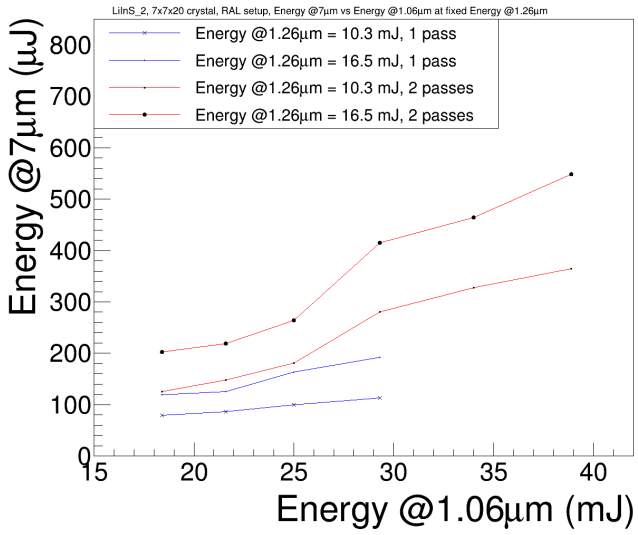

Figure 4.30: The increase of the output at 6.78 μm as a function of the two injected laser energies in single and double pass configuration. The plots are obtained keeping the 1.26 μm energy fixed at 10.3 and 16.5 mJ. These data are obtained with the 7×7×20 mm^3 $LiInS_2$ crystal

Tunability and stability measurements Other measurements were performed to study the tunability and the stability of the laser system. The first characteristic was tested changing the wavelength of the 6.8 μm beam by rotating the back mirror of the oscillator as described in the previous section 3.5. The result of this test can be seen in figure 4.31, where the plot represents the wavelength range between 6750 and 7150 nm versus the angle of the back mirror. The dependence is linear and can be used to set the needed wavelength.

A wavelength stability measurement was performed to check the stability of the wavelength in time. The measurement lasted around 25 minutes, but showed a good stability around the chosen value of 6812.25 nm, as can be seen in figure 4.32.

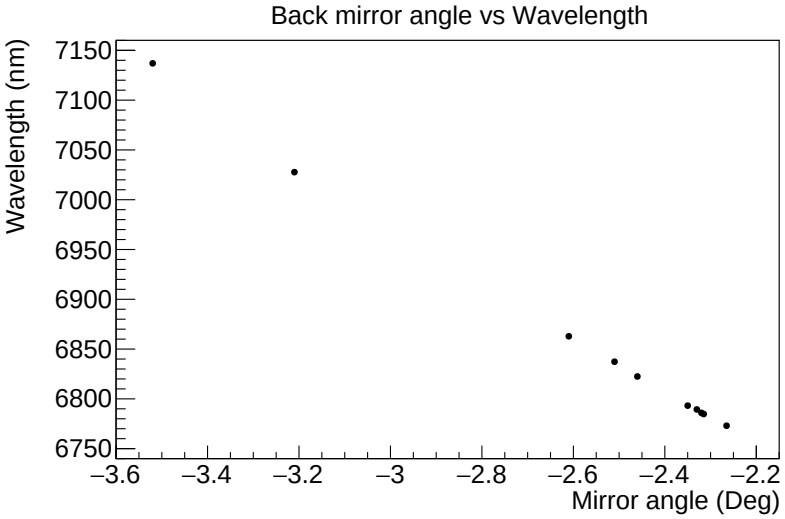

Figure 4.31: The laser wavelength interval between 6750-7150 nm reachable by moving the rotational piezomotor of the oscillator back mirror. These data were obtained with the 7×7×20 mm^3 $LiInS_2$ crystal.

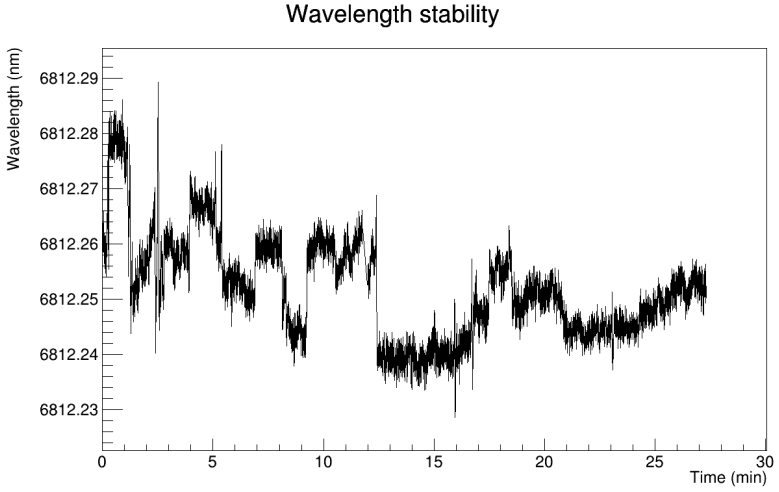

Figure 4.32: The stability of the wavelength at 6.8 μm vs time. These data were obtained with the 7×7×20 mm^3 $LiInS_2$ crystal.

Chapter 5

Conclusions

The topics of this thesis cover a broad spectrum of activities related to a high precision spectroscopy measurement, headed to a measurement of the proton radius characteristic.
In section 2.1, after an introduction to the FAMU methods, I recall beside the steps required to produce the muonic hydrogen, the measurement of the transfer rate and the calculations of the Zemach radius. In the following section the proof of the consistency of this method is presented through a series of results obtained from measurements coming from different gas mixtures, section 2.2. The analysis of the transfer rate on the hydrogen-argon gas mixture, which I performed, shows a weak dependence of the transfer rate on the temperature, and the non-suitability of this gas mixture for the experiment, making room for the use of oxygen.
Based on the requirements imposed by the FAMU method, the experimental setup and all the devices, that are part of it, were selected and are reported in the chapter 3. As part of my PhD work I took part in the development of the FAMU layout, of the data acquisition system and of the laser system.
Concerning the FAMU layout, I took care of all parts of the experimental apparatus: from the experimental room hosting the experiment, to the control of the environmental conditions, and to the mechanical stability of all elements. The choices which brought to the final setup, as described in chapter 3 are reported in section 4.1.
I also developed from scratch the software for the control of the laser, able to monitor all the parameters of the laser and remotely control the system. This program is also interfaced with the principal data acquisition system of the experiment, which also collects the data from the X-rays detectors.

These two systems are described respectively in 3.5 and 3.6.
The main work of my thesis was on the laser. Here I participated in the development in the 1.26 μm oscillator, the tests of the new amplification system, the characterization of the various DFG crystals with different setups, section 4.3. Different results have been attained with this laser system:

- measurement of the linear variation of the energy as a function of the pump and signal energies, to check energy production efficiency predictions;
- verification of the wavelength stability on times of the order of tenth of minutes showing a variability of 9.2 pm, in window of 2–4 minutes the stability was higher than 2.2 pm;
- check of the tunability range, covering a wide spectral range between 6750–7150 nm;
- measurement of the very narrow linewidth as required by the experiment, 30 pm, the measurement is limited by the instrument resolution for the entire spectral range;
- synchronization of the pump and signal pulses for optimal phase-matching, as this is one of the key point to maximize the energy at 6.78 μm;
- the maximum obtained energy was 540 mJ.

With the 7$\times$7$\times$20 mm^3 $LiInS_2$ nonlinear crystal the laser promises to fulfill almost all of the characteristics required by the experiment except the energy, as in table 5.1. Higher energies can be obtained by using crystals with bigger dimensions and higher efficiency like the 10$\times$10$\times$27 mm^3 yellow $BaGa_4Se_7$, that we have lately tested successfully on our test bench with the Elettra setup.

Among the many challenges of this experiment, which at present is in a harsh competition with other two similar initiatives, the main one is represented by the energy made available by the laser system. In this direction, my work continues also these days, optimizing the introduction of an improved optical path to double the energy production.

Parameters	FAMU requirements	FAMU laser present results
Wavelength	6785$\pm$3 nm	6730–6840 nm
Energy output	$>$ 1 mJ	0.5 mJ
Linewidth	$<$0.07 nm	$<$ 0.03 nm
Tunability step	0.03 nm	0.034 nm
Pulses duration	10 ns	7 ns
Repetition rate	25 Hz	25 Hz

Table 5.1: FAMU laser requirements and experimental results.

The data acquisition at RAL, which was supposed to take place in March 2020, was forced to be postponed firstly due to the COVID-19 pandemic and subsequently because of a one-year-long maintenance shutdown of the accelerator. The new schedule gives the opportunity to perform the data acquisition in September 2022.

Bibliography

[1] R. Pohl, R. Gilman, G. A. Miller, and K. Pachucki. Muonic hydrogen and the proton radius puzzle. *Annual Review of Nuclear and Particle Science*, 63(1):175–204, 2013.

[2] C. E. Carlson and B. C. Rislow. New physics and the proton radius problem. *Phys. Rev. D*, 86:035013, Aug 2012.

[3] J. C. Bernauer, P. Achenbach, C. Ayerbe Gayoso, R. Böhm, D. Bosnar, L. Debenjak, M. O. Distler, L. Doria, A. Esser, H. Fonvieille, J. M. Friedrich, J. Friedrich, M. Gómez Rodríguez de la Paz, M. Makek, H. Merkel, D. G. Middleton, U. Müller, L. Nungesser, J. Pochodzalla, M. Potokar, S. Sánchez Majos, B. S. Schlimme, S. Širca, Th. Walcher, and M. Weinriefer. High-precision determination of the electric and magnetic form factors of the proton. *Phys. Rev. Lett.*, 105:242001, Dec 2010.

[4] P. J. Mohr, D. B. Newell, and B. N. Taylor. Codata recommended values of the fundamental physical constants: 2014. *Journal of Physical and Chemical Reference Data*, 45(4):043102, 2016.

[5] Wikipedia. Standard_model — wikipedia, the free encyclopedia, 2021. [Online; controlled 06/10/2021].

[6] T. Yamazaki, K. Nagamine, S. Nagamiya, O. Hashimoto, K. Sugimoto, K. Nakai, and S. Kobayashi. Negative moun spin rotation. *Physica Scripta*, 11(3-4):133–139, mar 1975.

[7] W. Ruckstuhl et al. Measurement of the hyperfine splitting of the 1S state in muonic Li-7 as a search for axial vector muon nucleon interactions. *Nucl. Phys. A*, 433:634–648, 1985.

[8] R. Pohl, A. Antognini, F Nez, and et All. The size of proton. *Nature*, 466:213–216, 2010.

[9] E. Cline, J. Bernauer, E.J. Downie, and R. Gilman. MUSE: The MUon Scattering Experiment. *SciPost Phys. Proc.*, page 23, 2021.

[10] D. Bakalov, A. Adamczak, M. Stoilov, and A. Vacchi. Theoretical and computational study of the energy dependence of the muon transfer rate from hydrogen to higher-z gases. *Physics Letters A*, 379(3):151–156, 2015.

[11] C. Pizzolotto, A. Adamczak, D. Bakalov, G. Baldazzi, **M. Baruzzo**, R. Benocci, R. Bertoni, M. Bonesini, V. Bonvicini, H. Cabrera, D. Cirrincione, M. Citossi, F. Chignoli, M. Clemenza, L. Colace, M. Danailov, P. Danev, A. de Bari, C. De Vecchi, M. de Vincenzi, E. Fasci, E. Furlanetto, F. Fuschino, K. S. Gadedjisso-Tossou, L. Gianfrani, D. Guffanti, A. D. Hillier, K. Ishida, P. J. C. King, C. Labanti, V. Maggi, R. Mazza, A. Menegolli, E. Mocchiutti, L. Moretti, G. Morgante, J. Niemela, B. Patrizi, A. Pirri, A. Pullia, R. Ramponi, L. P. Rignanese, H. E. Roman, M. Rossella, R. Sarkar, A. Sbrizzi, M. Stoilov, L. Stoychev, J. J. Suárez-Vargas, G. Toci, L. Tortora, E. Vallazza, M. Vannini, C. Xiao, G. Zampa, and A. Vacchi. The FAMU experiment: muonic hydrogen high precision spectroscopy studies. *Eur. Phys. J. A*, 56:185, 2020.

[12] A. Adamczak, D. Bakalov, L. Stoychev, and A. Vacchi. Hyperfine spectroscopy of muonic hydrogen and the psi lamb shift experiment. *Nuclear Instruments and Methods in Physics Research Section B: Beam Interactions with Materials and Atoms*, 281:72–76, 2012.

[13] E. Mocchiutti, A. Adamczak, D. Bakalov, G. Baldazzi, R. Benocci, R. Bertoni, M. Bonesini, V. Bonvicini, H. Cabrera Morales, F. Chignoli, M. Clemenza, L. Colace, M. Danailov, P. Danev, A. de Bari, C. De Vecchi, M. De Vincenzi, E. Furlanetto, F. Fuschino, K.S. Gadedjisso-Tossou, D. Guffanti, K. Ishida, C. Labanti, V. Maggi, R. Mazza, A. Menegolli, G. Morgante, M. Nastasi, J. Niemela, C. Pizzolotto, A. Pullia, R. Ramponi, L.P. Rignanese, M. Rossella, N. Rossi, M. Stoilov, L. Stoychev, L. Tortora, E. Vallazza, G. Zampa, and A. Vacchi. First measurement of the temperature dependence of muon transfer rate from muonic hydrogen atoms to oxygen. *Physics Letters A*, 384(26):126667, 2020.

[14] R. Jacot-Guillarmod, F. Mulhauser, C. Piller, L. A. Schaller, L. Schellenberg, H. Schneuwly, Y.-A. Thalmann, S. Tresch, A. Werthmüller, and A. Adamczak. Muon transfer from thermalized muonic hydrogen isotopes to argon. *Phys. Rev. A*, 55:3447–3452, May 1997.

[15] C. Pizzolotto, A. Sbrizzi, A. Adamczak, D. Bakalov, G. Baldazzi, **M. Baruzzo**, R. Benocci, R. Bertoni, M. Bonesini, H. Cabrera, D. Cirrincione, M. Clemenza, L. Colace, M. Danailov, P. Danev, A. de Bari, C. De Vecchi, M. De Vincenzi, E. Fasci, F. Fuschino, K.S. Gadedjisso-Tossou, L. Gianfrani, K. Ishida, C. Labanti, V. Maggi, R. Mazza, A. Menegolli, E. Mocchiutti, S. Monzani, L. Moretti, G. Morgante, J. Niemela, A. Pullia, R. Ramponi, L.P. Rignanese, M. Rossella, M. Stoilov, L. Stoychev, J.J. Suárez-Vargas, L. Tortora, E. Vallazza, and A. Vacchi. Measurement of the muon transfer rate from muonic hydrogen to oxygen in the range 70-336 k. *Physics Letters A*, 403:127401, 2021.

[16] Rutherford Appleton Laboratory (RAL).

[17] RIKEN-RAL.

[18] M. Bonesini, R. Benocci, R. Bertoni, M. Clemenza, D. Ghittori, R. Mazza, E. Vallazza, A. de Bari, A. Menegolli, M. Prata, M. Rossella, **M. Baruzzo**, and E. Mocchiutti. Ce:LaBr3 crystals with SiPM array readout and temperature control for the FAMU experiment at RAL. *Journal of Instrumentation*, 15(05):C05065–C05065, may 2020.

[19] M. Bonesini, R. Bertoni, F. Chignoli, R. Mazza, T. Cervi, A. de Bari, A. Menegolli, M.C. Prata, M. Rossella, L. Tortora, R. Carbone, E. Mocchiutti, A. Vacchi, E. Vallazza, and G. Zampa. The construction of the fiber-SiPM beam monitor system of the r484 and r582 experiments at the RIKEN-RAL muon facility. *Journal of Instrumentation*, 12(03):C03035–C03035, mar 2017.

[20] M. Bonesini, R. Benocci, R. Bertoni, R. Mazza, A. deBari, A. Menegolli, M.C. Prata, M. Rossella, L. Tortora, E. Mocchiutti, A. Vacchi, and E. Vallazza. The upgraded beam monitor system of the famu experiment at riken–ral. *Nuclear Instruments and Methods in Physics Research Section A: Accelerators, Spectrometers, Detectors and Associated Equipment*, 936:592–594, 2019. Frontier Detectors for Frontier Physics: 14th Pisa Meeting on Advanced Detectors.

[21] V. Petrov. Frequency down-conversion of solid-state laser sources to the mid-infrared spectral range using non-oxide nonlinear crystals. *Prog. in Quantum Electronics*, 42:1–106, 2015.

[22] M. Gerhards. High energy and narrow bandwidth mid IR nanosecond laser system. *Opt. Commun.*, 241:493–497, 2004.

[23] G. Stoeppler, N. Thilmann, V. Pasiskevicius, A. Zukauskas, C. Canalias, and M. Eichhorn. Tunable Mid-infrared ZnGeP2 RISTRA OPO pumped by periodically-poled Rb:KTP optical parametric master-oscillator power amplifier. *Opt. Express*, 20(4):4509–4517, Feb 2012.

[24] L. I. Stoychev, H. Cabrera, K. S. Gadedjisso-Tossou, N. Vasiliev, Y. Zaporozhchenko, I. P. Nikolov, P. Sigalotti, A. A. Demidovich, J. J. Suárez-Vargas, E. Mocchiutti, C. Pizzolotto, J. Niemela, **M. Baruzzo**, M. B. Danailov, and A. Vacchi. 24 mJ Cr+4:forsterite four-stage master-oscillator power-amplifier laser system for high resolution mid-infrared spectroscopy. *Rev. Sci. Instrum.*, 90(9):093002, 2019.

[25] L. I. Stoychev, M. B. Danailov, A. A. Demidovich, I. P. Nikolov, P. Cinquegrana, P. Sigalotti, D. Bakalov, and A. Vacchi. DFG-based mid-IR laser system for muounic-hydrogen spectroscopy. In Jacob I. Mackenzie, Helena JelÍnková, Takunori Taira, and Marwan Abdou Ahmed, editors, *Laser Sources and Applications II*, volume 9135, pages 52 – 57. International Society for Optics and Photonics, SPIE, 2014.

[26] Hitran. `https://hitran.org/`.

[27] R. Benocci, M. Bonesini, K.S. Gadedjisso-Tossou, H. Cabrera, L. Stoychev, M. Rossella, **M. Baruzzo**, M. Consonni, and J.J. Suarez-Vargas. Laboratory tests for MIR light detection and transport with specialty optical fibres. *JINST*, 15(04):C04030–C04030, apr 2020.

[28] H.G. Heard. Laser parameter measurements handbook. page 386. Wiley, New York, 1968.

[29] L. I. Stoychev, H. Cabrera, K. S. Gadedjisso-Tossou, I. P. Nikolov, P. Sigalotti, A. A. Demidovich, J. J. Suárez-Vargas, E. Mocchiutti, J. Niemela, **M. Baruzzo**, N. Vasiliev, Y. Zaporozhchenko, M. B. Danailov, and A. Vacchi. Pulse amplification in a cr4+:forsterite

single longitudinal mode (SLM) multi-pass amplifier. *Laser Physics*, 29(6):065801, apr 2019.

[30] L. M. Frantz and J. S. Nodvik. Theory of pulse propagation in a laser amplifier. *Journal of Applied Physics*, 34(8):2346–2349, 1963.

[31] A. J. Tiffany, I. T. McKinnie, and D. M. Warrington. Pulse amplification of a single-frequency cr:forsterite laser. *Appl. Opt.*, 37(21):4907–4913, Jul 1998.

[32] R. W. Boyd. Chapter 2 - wave-equation description of nonlinear optical interactions. In *Nonlinear Optics (Third Edition)*, pages 69–133. Academic Press, Burlington, third edition edition, 2008.